This is to certify that the

dissertation entitled

Physical and Mechanical Properties of Hipped Ag Fibers Reinforced $YBa_2Cu_3O_{7-x}$ Superconductor Composite

presented by

Gun-Eik Jang

has been accepted towards fulfillment
of the requirements for

Ph.D. degree in Materials Science

Kalinath Mukherjee
Major professor

Date 5/3/92

PHYSICAL AND MECHANICAL PROPERTIES OF HIPPED Ag FIBERS REINFORCED $YBa_2Cu_3O_{7-x}$ SUPERCONDUCTOR COMPOSITE

BY

GUN-EIK JANG

A DISSERTATION

Submitted to
Michigan State University
in partial fulfillment of the requirements
for the degree of

DOCTOR OF PHILOSOPHY

Department of Metallurgy, Mechanics and Material Science

1992

ABSTRACT

PHYSICAL AND MECHANICAL PROPERTIES OF HIPPED Ag FIBER REINFORCED $YBa_2Cu_3O_{7-x}$ SUPERCONDUCTOR COMPOSITE

BY

GUN-EIK JANG

Ceramics exhibit a strong relationship between mechanical and physical properties and the processing and fabrication sequence. The final microstructure also depends on processing. This interrelation between processing, microstructure and properties is particularly true for the new high T_c superconducting ceramic oxides of the type, $YBa_2Cu_3O_{7-x}$. An attempt to improve the mechanical stability of such superconducting ceramics, through composite technology, requires a detailed understanding of the relationship between microstructure and processing. To characterize some of these relations, Several properties have been measured for sintered oxide superconductor.

Polycrystalline $YBa_2Cu_3O_{7-x}$ has proven to be difficult to densify by conventional sintering to the full theoretical density while maintaining the superconducting orthorhomic phase. This precludes conventional sintering from being an effective process for achieving full density.

In this research, the $YBa_2Cu_3O_{7-x}$ samples were prepared by two different processing techniques: one by conventional sintering and the other by hot isostatic pressing (HIP). It was determined that reinforcement with silver fibers and hot isostatic pressing produced the best results without degrading the su-

perconducting properties. In this thesis, physical and mechanical properties of HIP processed and silver fiber reinforced 1-2-3 based superconductors are discussed and compared with the properties of unreinforced and conventionally sintered samples. Finally, significantly improved mechanical properties such as fracture toughness and fracture energy, obtained by a multi-stage processing, are reported.

ACKNOWLEDGEMENTS

First of all, I would like to express my gratitude to Professor Mukherjee for his continual encouragement and guidance, which he provided throughout my Ph. D. program and research project. I would also like to thank my committee members for their timely review of this dissertation. A special thanks to my korean friends and colleagues in laser laboratory for their assistance and friendship.

Finally, a special thank you is to be extended to my wife Hwa-Young and my beautiful daughter Jee-Hee for their patience and continual encouragement during the many months of this research effort.

LIS

LIS

1.

2.

3

TABLE OF CONTENTS

LIST OF FIGURES

Figure

29.

30.

31.

32.

33.

34.

35.

36.

37.

38.

39.

40.

41.

42.

43(

Fi

63

LIST OF TABLES

I. INTRODUCTION

While the new class of high T_c (~ 93 K) ceramic superconductors represent a technological breakthrough [1], there are still a number of difficulties to overcome for use in practical applications. The brittle nature inherent in ceramics poses one of the most serious problems. It is important to recognize that the mechanical responses of these materials are similar to other advanced ceramics. A critical temperature of 93 K is acceptable for numerous design applications provided that the devices are mechanically stable. Moreover, many applications of superconducting oxides will require these materials to be fabricated in the form of wires or cables. The shaping of wires or cables typically require significant flexibility or ductility of the material from which the wires or cables are made. However, the oxide superconductor itself does not have enough flexibility and toughness to satisfy these shaping operations. The flexibility and toughness can, however, be increased by making a metal-oxide superconductor composite.

New investigations should be focused on second phase materials such as filaments, whiskers or fibers which can offer a continuous path for current flow, improved mechanical strength and retained superconducting properties. Processing conditions that will yield continuous, interwoven oxide and fiber-phase must be well developed.

The most important criterion to be considered for successful applications is the understanding of processing variables which influence the microstructure and electrical properties such as critical temperature and critical current density. It is well known that critical temperature is usually influenced by the crystal structure and long range order, while critical current density depends predominantly on the microstructural features such as grain boundaries, microcracks,

grain orientation and microchemistry. The low critical current density in the bulk polycrystalline materials is thought to arise from weak-link junctions of the superconductive phase across the grain and twin boundaries, microcracks, pores and voids, inclusions of non-superconducting phase, and the lack of appropriate texture formation. The chemistry of impurity phases in the grain boundaries, in particular, may be the other dominant factor in determining the current carrying capability as well as the resistance to grain boundary fracture. Although the presence of fine dispersion of impurities can increase critical current density by the flux pinning mechanism, proper control of processing conditions and microstructure was found to be crucial in attaining a high transition temperature and improved critical current density.

So far, a number of research projects have been successfully conducted in the area of superconducting composites, especially focused on particulate composites. However, none of the previous work has been undertaken in the area of fiber reinforced composites to study the modification of mechanical properties through the addition of fibers into ceramic oxide superconductors.

In the present study, Ag fiber reinforced $YBa_2Cu_3O_{7-x}$ (1-2-3 system) superconductor composite has been systematically studied as a function of the volume % Ag fibers. The reason for selecting Ag fiber as the reinforcing material in the 1-2-3 matrix can be explained as follows:

1. Ag has been found to be one of the few materials that does not degrade the superconducting properties of 1-2-3 system [2-5].
2. Ag remains as a pure metal, that is chemically stabilized, in the 1-2-3 system [2-5].
3. The melting temperature of Ag, 960.5°C, is higher than the normal sintering or processing temperature of the 1-2-3 system.

4. Ag lowers the normal state resistivity and contact resistance of the composites [3].
5. It has been shown that Ag particulates improve mechanical properties like Young's modulus and fracture strength [4,5] of the 1-2-3 matrix.

The overall objective of this research is to evaluate the feasibility in order to obtain dense superconducting composites which are mechanically reliable and have a greater fracture toughness. This practical objective is coupled with the fundamental objective, which is to understand the relationship between processing conditions, microstructure, and superconducting properties.

2. LITERATURE SURVEY

2. 1 High T_c Superconductor: History, Structure and Properties

2. 1. 1 History of high temperature superconductors

The discovery of the La-Ba-Cu-O system, with a superconducting transition at 30 K, by Bednorz and Müller [6] and subsequent evolution of 90 K Y-Ba-Cu-O system [1,7] have stimulated extensive investigation in the preparation and characterization of various types of ceramic superconductors.

To date, research has been conducted by a very large number of investigators to further increase the critical temperature. The history of the high temperature oxide superconductors has shown that elemental substitution is the most effective approach for raising the transition temperature. Substitution of Sr for Ba in La-Ba-Cu-O system led to discovery of 40 K La-Sr-Cu-O superconductor [8, 9]. Substitution of Y for La produced the 90 K Y-Ba-Cu-O system [1], which is the first system to have its critical temperature above liquid nitrogen boiling temperature (77 K). Also the effect of various other substitutions in Y-Ba-Cu-O system, on the superconducting transition temperature, has been studied extensively [10-12]. Substitution of Tl for the rare earth metal (R) in the R-Ba-Cu-O system, produced the 90 K Tl-Ba-Cu-O system [13,14], and addition of Ca in the Tl-Ba-Cu-O system led to the 120 K Tl-Ca-Ba-Cu-O system [15]. The Tl-Ba-Cu-O system is the first non-rare earth system which reaches zero resistance above liquid nitrogen temperature, whereas the Tl-Ca-Ba-Cu-O system is the first system which reaches zero resistance above 100 K, and has the highest transition temperature for zero resistance.

On the other hand, substitution of Bi for La in La-Sr-Cu-O system led to 20 K Bi-Sr-Cu-O system superconductor [16]. But partial substitution of Ca for Sr in this system produced 110 K Bi-Ca-Sr-Cu-O superconductor [17]. A number of researchers have reported that substitution of a 3-d transition metal such as Ni, Zn, or Co for Cu can sharply decrease the critical temperature [18,19,20]. The ionic size and orbital structure of the 3-d transition metals are very similar to those of Cu. The 3-d transition metals will occupy the Cu sites if transition metals are substituted into the Y-Ba-Cu-O system. However, according to Xiao et al. [19], T_c is strongly correlated with the size of paramagnetic moments of doped elements. Addition of Zn provides an extra electron which fills up anti-bonding d-band and thereby reduces the density of state at the Fermi level. Tarascon et al. [18] have suggested and tried to explain the reduction of T_c by 4 different inter-related mechanisms; structural disorder, oxygen vacancies, the dopants inducing a different oxidation state in the copper and magnetic depairing. However, there is no explanation as yet regarding the reduction of T_c when substitution was made for Cu.

There was a report of critical temperature above 150 K in Y-Ba-Cu-O system [21]. Ovshinsky et al [21] claimed superconducting zero-state at 155 K by adding fluorine to 1-2-3 system. They synthesized five different compositions of $YBa_2Cu_3F_xO_z$ by substituting part of oxygen with fluorine. However, these results were contradicted by other researchers [22, 23]. Yan et al. [22] and Narottom et al. [23] reported they could not observe such a high transition temperature reported by Ovshinsky et al. [21]. Their results only indicate that superconducting temperature is slightly increased (up to 93.4 K) and sharpened with low levels of fluorine concentration. Yan et al. also [22] studied F and Cl effects on the 1-2-3 system. Most samples of $YBa_2Cu_3F_xCl_YO_z$, showed

diamagnetic susceptibility at a temperature between 89 and 94 K without any significant improvement of T_c.

Among high T_c oxide superconductors, Y-Ba-Cu-O is perhaps one of the most widely studied compounds because it exhibits superconducting behavior above 90 K and is relatively easy to synthesize. Fig. 1 shows the typical effect of various doping elements on the critical temperature of Y-Ba-Cu-O system as measured by a.c. susceptibility [24]. It can be seen that the superconducting temperature and transition range in samples doped with Au and Cd is still high and sharp. However, doping with other elements , for example Zn or Al, seems to destroy the superconducting transition and/or broadens the the transition range.

2. 1. 2 Crystal structure of $YBa_2Cu_3O_{7-x}$

$YBa_2Cu_3O_{7-x}$ was identified as the phase exhibiting superconducting transition at 90 K. This compound has a distorted orthorhombic oxygen deficient perovskitelike structure [25]. All observed x-ray powder diffraction peaks can be accounted for by choosing an orthorhombic unit cell with lattice parameters given by: a = 38.20 nm , b = 38.93 nm, and c = 116.88 nm [26]. Compounds with the perovskite structure (Fig. 2) have the formula of ABO_3, where A is the relatively large ion in the center of the unit cell, B is the small ion at the corners and O is the oxygen ion at the edge of the unit cell [27]. The cell volume is 3 times the standard perovskite cell and structure can be visualized as a stack of alternating layers in a c-axis: ($BaCuO_3$) : ($YCuO_3$) : ($BaCuO_3$) [27,28]. The crystal structure of Y-Ba-Cu-O [29] in Fig. 3 resembles three stacked cubic perovskite unit cells, however there are major differences between the two structures. While in a perovskite structure, copper ions are

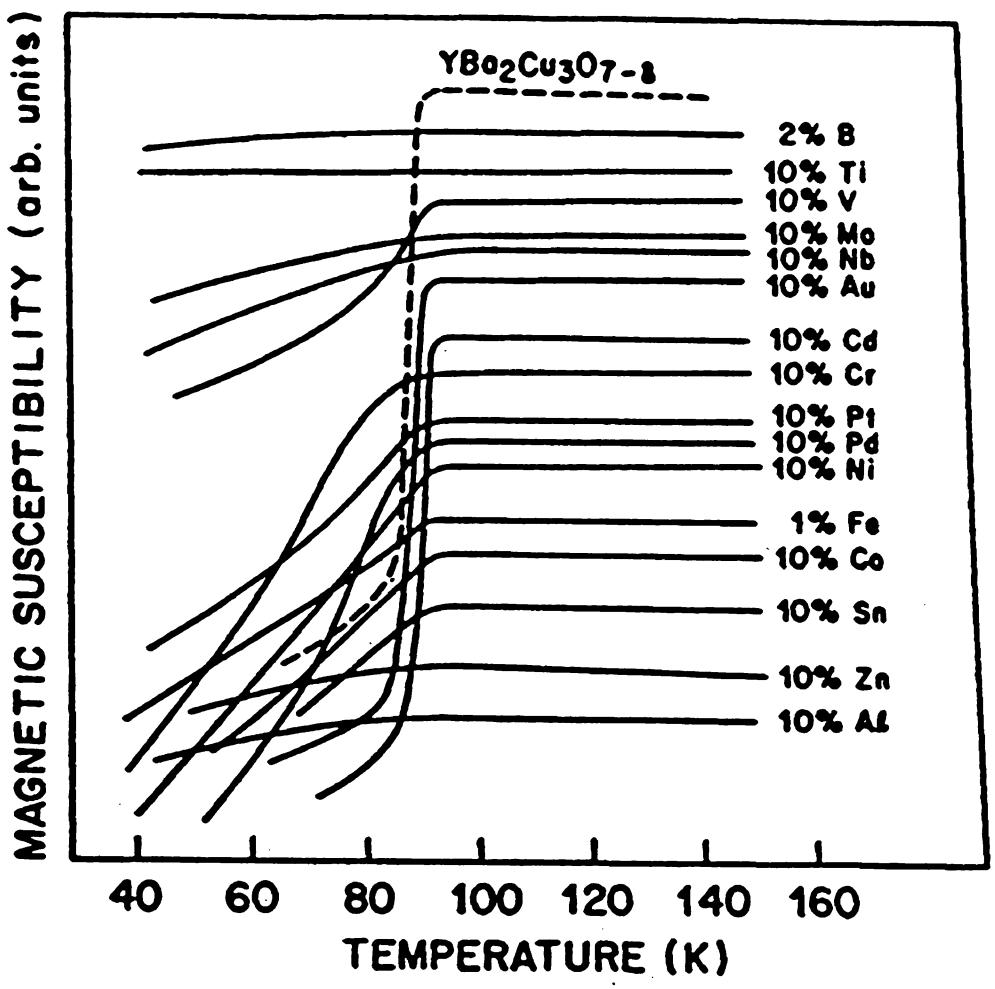

Fig. 1. The effect of various doping elements (in weight percent) on the critical temperature of $YBa_2Cu_3O_{7-x}$ as measured by a.c. susceptibility (Ref. 24).

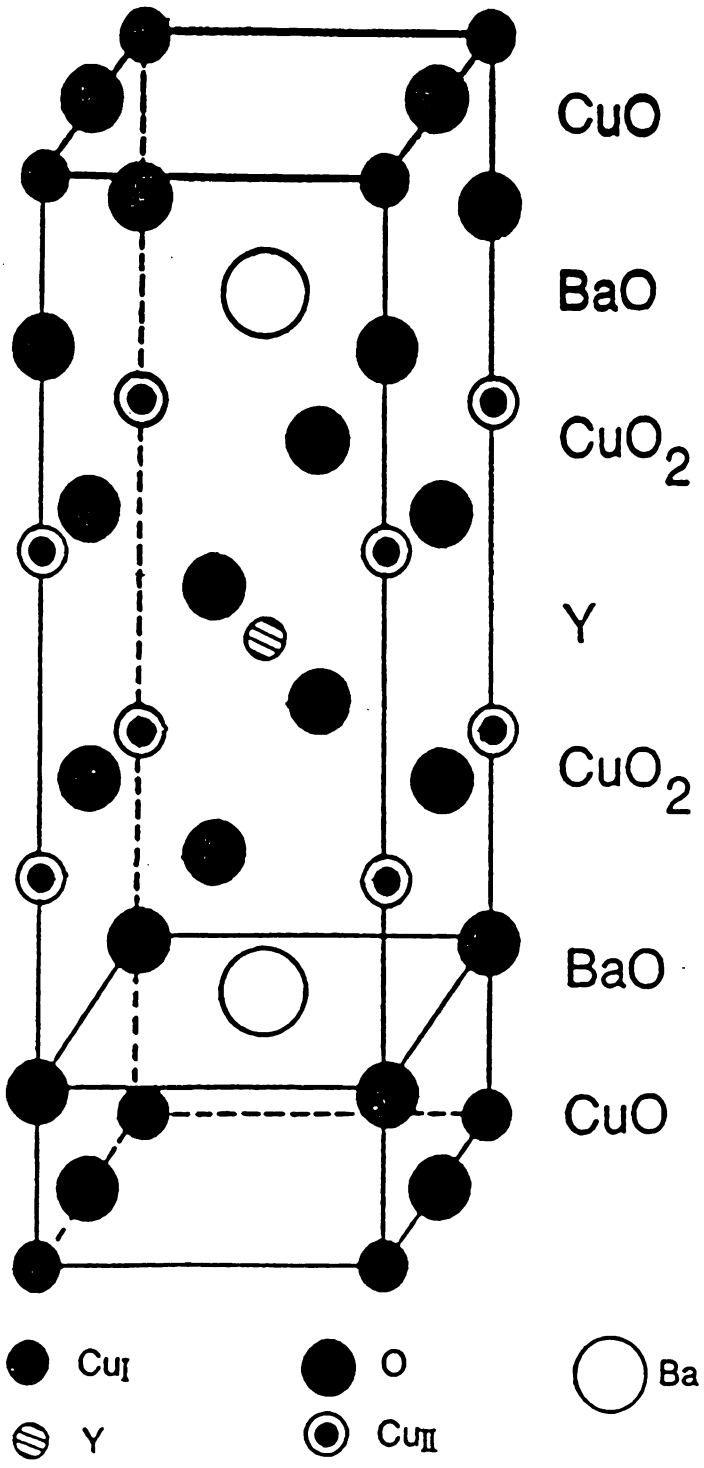

Fig. 3. The crystal structure of $YBa_2Cu_3O_{7-x}$ (Ref. 29).

located in the center of an oxygen octahedron, copper ions occupy two symmetry sites [30,31]. In the structure of Y-Ba-Cu-O, all oxygen atoms are missing in the (002) yttrium atom plane and oxygen vacancies occur in a strongly preferred way. In the basal plane, half of the oxygen atoms are missing; thus vacancies occur along the a-axis, leading to an orthorhombic distortion.

Jorgensen et al. [32] studied T_c as a function of the fractional occupancy of the oxygen sites. They found that $YBa_2Cu_3O_{7-x}$ compound can contain, on the average, from six to seven oxygen atoms per unit cell and in the orthorhombic phase, T_c decreases smoothly as x changes from 0.3 to 0.7 and reaches zero at the orthorhombic-tetragonal transition. Tetragonal $YBa_2Cu_3O_{7-x}$ is not superconductor. Also they pointed out the structure transformation from the tetragonal to the orthorhombic lattice for 1-2-3 phase, strongly depends on the oxygen content and the ordered state of the oxygen vacancies in the lattice. This systematic depression of T_c is correlated with the decrease in the oxygen content which alters the electronic structure of the Cu-O network.

There is a reversible phase transition from non-superconducting tetragonal to superconducting orthorhombic at about 750°C [29]. This means at high temperatures, oxygen and oxygen vacancy ordering are supposed to be distributed at random and the structure becomes tetragonal with parameters a = b. Since the phase transition is associated with changes in oxygen content, the mechanism of high T_c superconductivity is associated with oxygen vacancies. It has been known that oxygen loss and disorder only occur on CuO basal planes and that the rest of the layers do not participate in the order-disorder transition of the oxygen and vacancies.

2. 1. 3 Mechanical and electrical properties in Y-Ba-Cu-O superconductor

Ever since the discovery of high transition temperature superconductors [1], considerable efforts have been expended toward the investigation of this and other high temperature superconductors (HTS). A number of difficulties, however, have to be overcome before practical applications of bulk HTS can be realized. There are two main problems before these materials are successfully utilized in actual devices. One of these is the inherent brittleness of HTS. The brittleness in mechanical properties, is related not only to the intrinsic nature of ceramics with a layered structure, but also to the presence of porosity unavoidably present in the sintered samples.

The mechanical properties of single or poly-crystalline $YBa_2Cu_3O_{7-x}$ are comparable to those of typical brittle ceramics, with fracture toughness values (K_{Ic}) of about 1 MPa $m^{1/2}$ [33-35]. The fracture toughness of melt processed samples, which was measured by indentation method, was estimated to be 1.2 MPa $m^{1/2}$ [36].

Estimated fracture strength of pure 1-2-3, according to Nishio et. al. [37], was about 25 to 40 MPa depending on processing conditions. Also fracture strength and Young's modulus of pure 1-2-3 produced by liquid phase processing technique was 40 MPa and 81 GPa respectively [38].

A number of research projects have been conducted to improve the mechanical and fracture properties of HTS and different superconducting composites, especially in particulate composites[39-41]. Among these attempts, the 1-2-3 system containing Ag [42-49] has been most extensively studied. Nishio et al. [37] prepared composite superconductors by sintering a mixture of YBCO

and Ag powder at various proportions, ranging up to 92 volume %, and were able to enhance the mechanical strength against fracture to about 4 - 5 times as large as that in the sintered YBCO sample. This was achieved without seriously lowering the superconducting transition temperature. A liquid phase processing method has been developed to manufacture bulk Ag/YBCO composites by Lee et al. [38]. In nominal 15 wt % Ag composites, the measured Young's modulus was 100 GPa and fracture strength was 70 MPa. Ag/YBCO composite, reinforced by adding Zr, has been synthesized by Oka et al. [50]. The flexural strength in $Ag/Zr_YYBa_2Cu_3O_{7-X}$ reached its maximum value of 280 MPa at the composition Y = 0.8 and 33 vol. % Ag. This value is more than 5 times as large as in the sintered YBCO. They pointed out the enhanced mechanical strength was attributed to the unique microstructure, in which dispersed Ag particles remain intact with Zr-bearing YBCO matrix, whereas CuO and $BaZrO_3$ precipitates in the 1-2-3 phase matrix act to reinforce the ceramic without disrupting the superconducting channel.

1-2-3/Ag composites manufactured by solid-state sintering are characterized by randomly oriented grains of 10 - 40 μm size. Typically, silver is found to reside in the voids and along the grain boundaries, with small amounts of Ag entering the 1-2-3 lattice [2]. Sintering of 1-2-3 superconductor is enhanced by Ag addition, and the percentage of theoretical density of these composites increases with Ag content. Consequently, mechanical properties like Young's modulus and fracture strength increase with Ag addition [4-5].

Unfortunately, even though the mechanical properties of the HTS are improved, the transport critical current density (J_c) of these composites remains between 50 and 600 A/cm^2 [51], which is insufficient for practical applications. For practical applications, J_c must be on the order of 10^5 A/cm^2 at magnetic fields on the order of 1 to 10 Tesla at 77 K [52]. However, only for epitaxially

grown thin films [53] and single crystals [54] of 1-2-3 the critical current density has reached the range of 10^5 - 10^6 A/cm^2. Unfortunately J_c of bulk 1-2-3 superconductors is typically three orders of magnitude lower [51].

Highly anisotropic crystal structures of all of the presently known high T_c oxides lead to strongly anisotropic electron transport properties in both the normal and superconducting states, especially, in single crystals. The anisotropic behavior of single crystal $YBa_2Cu_3O_{7-x}$ has been studied by several investigators [55, 56] by magnetization of the crystal with the field applied both parallel and perpendicular to the Cu-O planes. Fig. 4 shows magnetic hysterisis loops at 4.5 K for the Cu-O plane perpendicular to the field lines and parallel to the field line. In Fig. 4(a), actually the induced screening currents flow parallel to the Cu-O plane. Fig. 5 shows the field and temperature dependance of the critical current density determined from the hysterisis curves in Fig. 4. As can be seen in Fig. 5, single crystal of $YBa_2Cu_3O_{7-x}$ demonstrates a strong anisotropy with the good conducting directions being along the Cu-O planes.

The progress toward the much expected major application of bulk high T_c superconductors has been hindered by their low critical currents, especially in strong magnetic fields. In sintered superconductors, J_c decreases very rapidly with applied magnetic field. For sintered samples of $YBa_2Cu_3O_{7-x}$, a flux density of only 0.01 T depresses J_c from its zero field value by a factor of ten. For higher fields, the J_c vs. B curve flattens and decreases slowly with a slope which depends on temperature. Thus, in bulk polycrystalline materials, it would be advantageous to have a strong crystallographic texture with the basal plane of the grains parallel to the conductor axis.

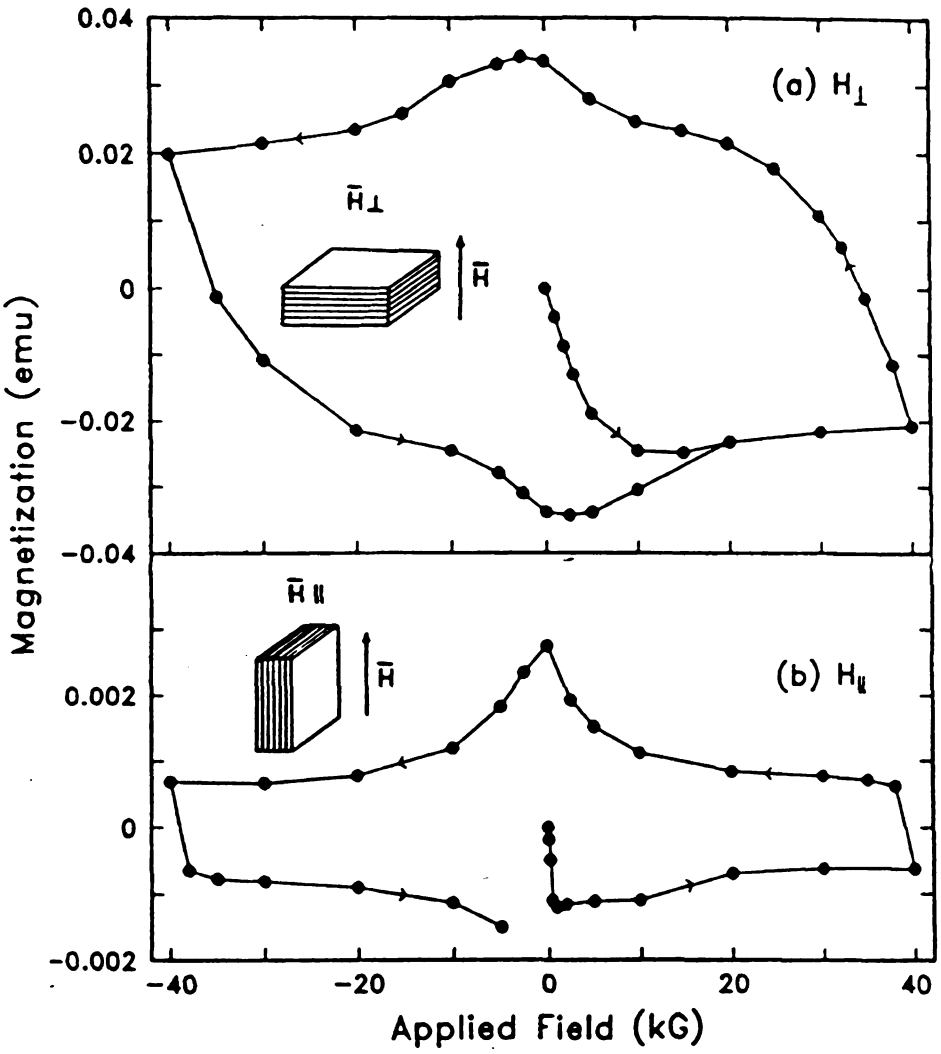

Fig. 4. Magnetization hysteresis loops at 4.5 K for a single crystal of 1-2-3 with the Cu-O planes oriented (a) perpendicular to the magnetic field and (b) parallel to the applied field (Ref. 55).

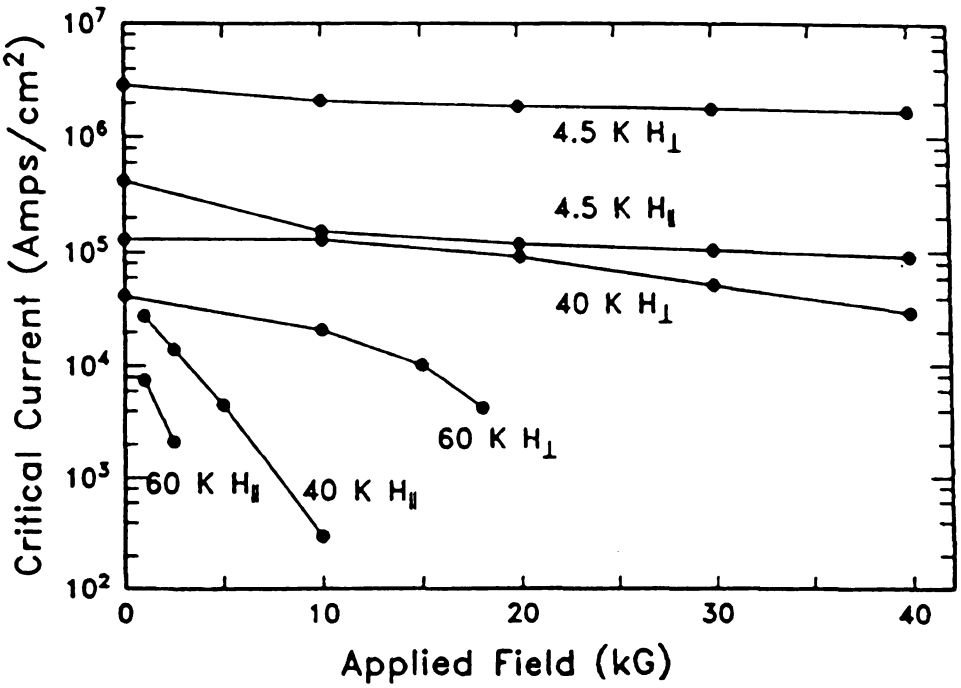

Fig. 5. Critical current densities deduced from magnetization hysteresis as a function of magnetic field applied either parallel or perpendicular to the Cu-O planes (Ref. 55).

2. 1. 4 Weak-link behavior at the grain boundaries

It is necessary to focus on the major limiting factors of current transport in terms of weak-link behavior at the grain boundaries [51]. As mentioned before, it is logical that microstructure modifications, which lead to lowering of grain boundaries angles along the current paths, should enhance J_c. Two major causes for the low critical currents at 77 K in bulk, polycrystalline high T_c superconductors are: weak links at the grain boundaries and flux line movement within the grains. The latter is due to insufficient flux pinning in Y-Ba-Cu-O and severe flux creep in Bi-Sr-Ca-Cu-O and Tl-Ba-Ca-Cu-O. Various processing techniques are aimed at overcoming these problems. Fig. 6 shows transport J_c vs. H in Y-Ba-Cu-O. The shaded area represents the improved intergrain J_c value in bulk Y-Ba-Cu-O with added flux pinning defects [24].

It is now well known that Josephson type weak links are present at the grain boundaries of polycrystalline high T_c superconductors [57,58]. The misorientation between adjacent grains adversely influences the current-carrying capability at the grain boundary [58], although there are indications that some specially oriented boundaries may not behave as weak links [59]. Across most of the high angle grain boundaries, the flow of transport electrical current is severely limited, especially in the presence of a magnetic field.

The exact nature of the grain boundary weak links is still not clearly understood, although it is most likely related to the disturbed crystal structure. Chemical inhomogeneity, the presence of many dislocations at the grain boundaries [60] and incoherent boundaries are other potential barriers to supercurrent flow. In many previous studies of grain boundary composition, regions of excess copper and oxygen depletion of grain boundaries were

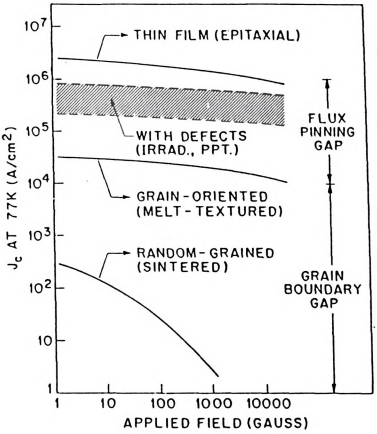

Fig. 6. Transport J_c vs. H in $YBa_2Cu_3O_{7-x}$.
The shaded area represents the improved intergrain J_c values in bulk $YBa_2Cu_3O_{7-x}$ with added flux pinning defects (Ref. 24).

observed with respect to the grain interior [61,62]. The large anisotropy in thermal expansion and the strain associated with the phase transition, result in microcracks between grains. These microcracks also hindered supercurrent flow. However, the weak link problem in high T_c superconductors can be greatly reduced by the elimination or minimization of high angle grain boundaries in the paths of the transport current. This can be achieved by a preferential crystallographic alignment of grains parallel to the a-b conduction planes (CuO_2 planes).

Grain alignment, through melt-processing, have been successfully used in this regard [63, 64]. Salama et al. [65] developed a liquid-phase processing technique that results in oriented-grains of 1-2-3 superconductors. They claim that J_c is as high as 75,000 A/cm^2 at 77 K and zero applied field. Directional solidification techniques are now widely used to produce bulk 1-2-3 samples with transport critical current densities exceeding 10^4 A/cm^2 in applied fields of several tesla. Jin et al. used the term "melt texturing" to describe their pioneering work in this area [64]. In the case of 1-2-3, melt texturing describes directional solidification from the melt or partially melt state. While there are a number of variations of the texturing techniques, they all involve heating 1-2-3 above its peritectic decomposition temperature (1,010°C in air) and slow cooling to form aligned, generally large, grains of the superconductor. Fig. 7 shows a schematic illustration of melt-texture processing. The optical microstructure of the melt textured material, reveals near perfect alignment of the 1-2-3 superconductor phase in the a-b direction along the length of the sample. Fig. 8 shows the effect of temperature gradient on the melt-textured microstructure. The melt-textured Y-Ba-Cu-O exhibits significantly improved J_c and greatly reduced field dependency as shown in Fig. 8. Although a desirable microstructure has been identified for producing high J_c values, the difficulty, in practice, of

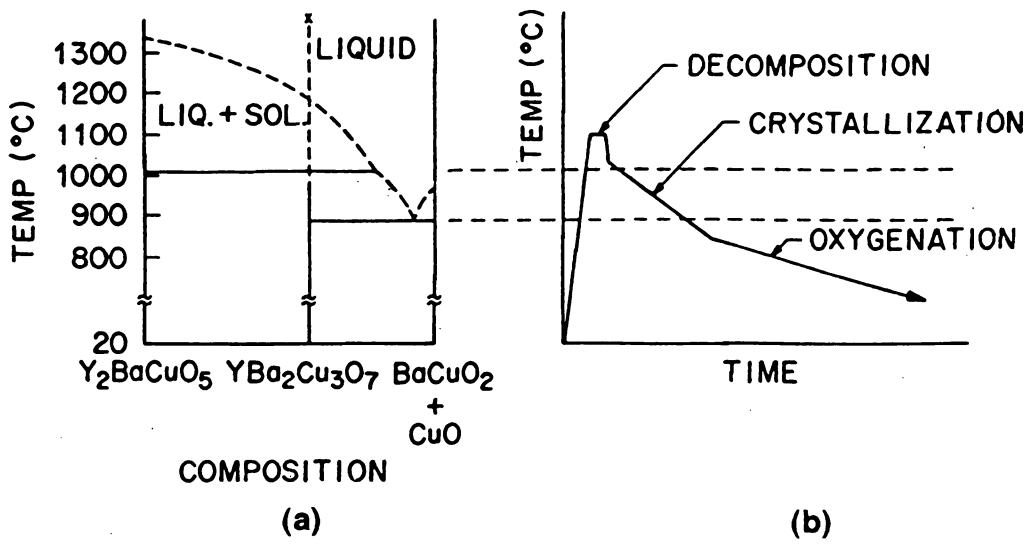

Fig. 7. A schematic illustration of time, temperature and phase equilibria, associated with melt-texture processing
(a) A qualitative sectional phase diagram
(b) Three basic processing steps, shown as the temperature-time curve (Ref. 24).

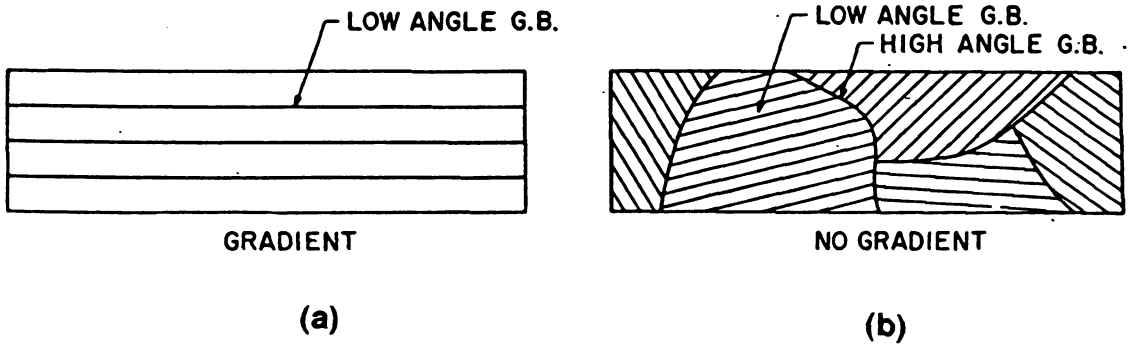

Fig. 8. The effects of temperature gradient on the melt-textured microstructure.
(a) Long-range grain alignment, obtained with a temperature gradient.
(b) Locally melt-textured structure, obtained without a temperature gradient (Ref. 24).

achieving highly aligned microstructures over extended distances is formidable. The longest reported distances, over which "single domain" types of structures have been generated, are on the order of 5 cm or less. Also another difficulty to produce grain alignment is extremely slow travel speed (Bridgement type processes) necessary for processing.

As stated above, even though progress has been made in this area, especially to increase J_c by melt-texturing techniques, there are still a number of difficulties to be overcome. The major challenge is to develop a commercially acceptable processing technique which yields high value of J_c, maintains a critical temperature of ~90 K and provides sufficient fracture toughness for design purposes.

2. 2 Superconductor Processing: Techniques and Mechanisms

2. 2. 1 Sintering and Hot Isostatic Pressing

Generally, in conventional sintering process, densification occurs by capillary-driven, long range diffusion processes. The driving force for sintering is a reduction in the system free energy via the decreased surface curvatures and an elimination of surface area. A characteristic feature of sintering is that the rate is very sensitive to temperature. Consequently, full densification can be achieved only at temperatures approaching the melting temperature where diffusion becomes rapid. However, the achievement of high homologous sintering temperatures (~ 0.8 of melting temperature) become technically difficult and also is limited by the phase stability (see phase diagram in 8 (b)). This precludes ordinary sintering from being an effective process for achieving full density.

Hot Isostatic Pressing (HIP) is a process in which sintering is enhanced by the application of high isostatic pressures. The HIP brings about the consolidation of powder materials by gas pressure at elevated temperature through hot deformation processes. This means that relatively rapid densification can be carried out at a lower temperature in a relatively short time.

The use of the hot isostatic press has proven to give fully dense metals and ceramics in other applications [66-69]. For polycrystalline $YBa_2Cu_3O_{7-x}$, it has been difficult to densify to full theoretical density by HIPing, while maintaining the superconducting orthorhomic phase [70-73].

Basically, there are three different types of HIP techniques: (1) post-HIP, (2) sinter-HIP and (3) encapsulation HIP. In post-HIP the material is presintered to a density at which there is little or no interconnected or open porosity and then HIPed. With sinter-HIP, the material is sintered in-situ in the HIP equipment, preferably under vacuum, until a closed pore structure is formed and then HIPed without removing from the apparatus. The third method, encapsulation HIP, requires the material to be contained within a gas-tight envelope whilst still in the green state and then HIPed. The envelope must be formed from a material which is deformable at the processing temperature so that the pressure can be transmitted to the specimen to aid the sintering process. The envelope must also remain intact in order to protect the material from the gas.

Among three different HIP techniques, the main attraction of encapsulation HIP is that the material does not need pre-sintering to give a completely closed pore system and therefore high levels of sintering aids are not required. Another advantage is that a greater degree of microstructural control is obtained. By encapsulation HIPing from the green state, the increased densification rate at lower sintering temperatures, due to the application of the pressure,

enables fine grained microstructures to be produced by limiting the extent of grain growth.

There are many methods of encapsulation using glass materials [74]: glass capsule method, glass bath method, glass powder coating method and glass powder pressing method. Also high melting point metals such as tantalum can be used to form deformable cans which are packed under vacuum and sealed by welding.

2. 2. 2 HIP mechanisms as applied to $YBa_2Cu_3O_{7-x}$ consolidation

Several mechanisms are considered to contribute to densification during HIPing: yielding, power law creep (PLC), Nabarro-Herring/Coble creep (NHCC) and diffusion. When pressure is applied to packed particles, it is transmitted through the powder bed as a set of forces acting across the particle contacts. If an external pressure P is applied to the compact with a density D and coordination number Z, the average contact force, f can be calculated according to the following equation [75].

$$f = 4\pi PR^2/ZD, \qquad (1)$$

where R is the average powder particle radius. The contact force produces a contact pressure, P_{eff}, on each particle contact area of a:

$$P_{eff} = f/a = 4\pi R^2 P/aZD \qquad (2)$$

The deformation at these contacts is, at first elastic but as the pressure rises, the contact forces increase, causing plastic yielding and expanding the

points of contact into contact areas. Yielding occurs when the contact pressure exceeds yield strength of the material, and hot deformation occurs almost instantaneously. Once these contact areas can support the forces without further yielding, time-dependent deformation processes determine the rate of further densification. These time dependent processes are power-law creep (in the contact zones) and diffusion (from a grain boundary source to the void surface).

Power law creep, a slower process, is governed by the usual equation;

$$\dot{\varepsilon}_P = A\,\sigma^n \exp(-Q_{creep}/RT) \qquad (3)$$

where, $\dot{\varepsilon}$ is the creep rate, A and n are material constants, Q_{creep} is the creep activation energy, R is gas constant and T is temperature.

Nabarro-Herring/Coble creep (diffusional creep) occurs by grain boundary diffusion and sliding. Nabarro-Herring creep results from vacancy redistribution from a higher vacancy concentration in the region of a material experiencing a tensile stress to the lower vacancy concentration regions subject to compressive stresses. This results in a vacancy flux from the former to the latter areas, and a mass flux in the opposite direction. Therefore, the grain elongates in one direction and contracts in the other, that is, creep deformation occurs. Nabarro-Herring creep is expressed by following equation:

$$\dot{\varepsilon}_{NH} = A_{NH}\,(D_L/d^2)\,(\sigma\Omega/kT) \qquad (4)$$

where, A_{NH} represent geometric factors, D_L is self-diffusion coefficient, d is grain size, σ is applied stress, Ω is the atomic volume, k is Boltzmanns constant and T is temperature. Nabarro-Herring creep is accomplished solely by diffusional

mass transport and dominates creep processes at much lower stress levels and higher temperatures than those at which creep is controlled by dislocation glide.

Coble creep is closely related to Nabarro-Herring creep and is driven by the same vacancy concentration gradient that causes Nabarro-Herring creep. However, in Coble creep mass transport occurs by diffusion along grain boundaries in a polycrystal or along the surface of a single crystal. Coble creep mechanism is expressed by following equation:

$$\dot{\varepsilon}_c = A_c (D_{GB}\delta'/d^3) (\sigma\Omega/kT) \qquad (5)$$

where, A_c represent geometric factors, D_{GB} is grain boundary-diffusion coefficient, δ' is an appropriate grain boundary thickness, d is grain size, σ is applied stress, Ω is the atomic volume, k is Boltzmanns constant and T is temperature.

From the above equations (4 and 5), it can be seen that Coble creep is more sensitive to grain size than is Nabarro-Herring creep. Even though both forms of creep are favored by high temperatures and low stresses, it is expected that Coble creep will dominate the creep rate in very fine grained materials. Also both deformation modes are effective only when the powder is polycrystalline and the grain size is small compared to the powder particle size.

During diffusional creep of a polycrystal, additional mass-transfer processes must occur at the grain boundaries to prevent the formation of internal voids or cracks. These result in grain-boundary sliding and the diffusional creep rate must be balanced exactly by the grain-boundary sliding creep rate if internal voids are not to be formed. The mass transfer can be produced by volume diffusion near the grain boundary, by grain-boundary diffusion, or by both mechanisms. The mass transfer is driven by vacancy concentration gradients in the same manner that diffusional creep is driven. Diffusional flow and

grain-boundary sliding, therefore, can be considered sequential processes in which mass is first transported by Nabarro-Herring and/or Coble creep and a grain shape change and separation is effected.

Among several mechanisms, densification by long range diffusion, or sintering, plays only a minor role in HIPing, dominating only at very low pressures. The overall behavior of densifying mechanism is quite complicated because each has a different dependence on particle size, on the external variables P, T, and on powder properties and current geometry. One way of analyzing it is to construct HIP maps which identify the dominant mechanisms and predict densification rates and times, as a function of pressure and temperature. The HIP process of $YBa_2Cu_3O_{7-x}$ was modeled by Tien et al. [70] in terms of pressure, temperature, powder particle size, grain size and entrapped gas. They tried to assess the feasibility of hot isostatic pressing to obtain fully dense bulk superconductors using HIP modeling and experimental verification. For the calculation, the powder was assumed to be spherical and monosized.

2. 3 Mechanical Properties of Ceamic Matrix Composites

2. 3. 1 The general theory of strength of fiber reinforced composites

The use of high modulus fibers in a lower modulus matrix is well known and is a routinely practiced technique for increasing the strength. The general theory of fiber reinforcement suggests that significant strengthening will occur if the elastic modulus of the fibers is greater than that of the matrix, if tensile stress can be transmitted to fibers, but less toughening will occur. Conversely, if fibers of lower modulus are employed, the ultimate failure strength will be reduced while toughening will be increased because the matrix rather than fibers will

carry a greater proportion of the applied load. Stress may be transmitted to the fibers by plastic or elastic deformation of the matrix. Some crack-tip energy may be absorbed by the plastic deformation of a ductile fiber.

In the absence of internal stresses, the strength, σ_c of continuous fiber reinforced composites may be estimated by the simple rule of mixtures criterion, assuming the strains in each component are equal:

$$\sigma_c = \sigma_f V_f + \sigma_m' V_m \quad \text{for} \quad V_f > V_{min} \tag{6}$$

$$\text{or} \quad \sigma_c = \sigma_f V_f + \sigma_{mu} V_m \quad \text{for} \quad V_f > V_{min} \tag{7}$$

where the subscripts c, f, m refer to composite, fiber, and matrix. And σ_f is the fracture strength of the fiber, V_f, the volume fraction of fiber, σ_m', the matrix stress at the fiber failure strain, V_m, the volume fraction of the matrix phase, V_{min}, the minimum volume fraction of fiber and σ_{mu} is the stress carried by the matrix when the composite is strained to ultimate failure strength. The validity of both of these equations is dependent on V_f exceeding a value V_{min}. Also both equations depend on which component fails first, and assuming that composite failure occurs immediately following failure of one of the components. If the fibers fracture first then the composite strength is followed by equation (6). Conversely, if the matrix fractures first then the composite strength is given by equation (7). A second important volume fraction is V_{crit} which is that fraction of fibers that must be exceeded for fiber strengthening to occur. These two values are illustrated in Fig. 9. In Fig. 9, plot A represents equation (6) and B represents:

$$\sigma_c = \sigma_{mu}(1 - V_f) \tag{8}$$

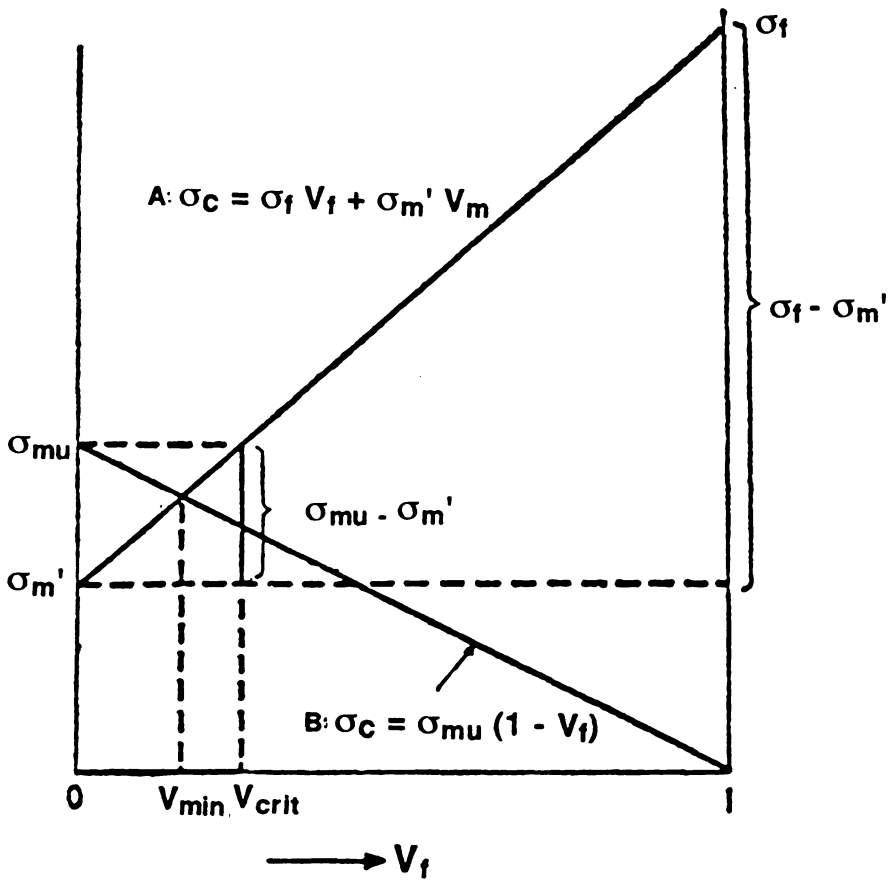

Fig. 9. Diagram illustrating V_{min} and V_{crit} and their relationship to σ_f, σ_m and σ_{mu}.

The intersection of the two curves is at V_{min}, i.e. where fiber and matrix break simultaneously and V_{crit} is always greater than V_{min}. When $\sigma_{mu} - \sigma_m'$ is small then little strengthening is required to exceed the matrix strength, and this can be achieved by a small volume of fiber, i.e. V_{crit} is small. Conversely when $\sigma_{mu} - \sigma_m'$ is large and the matrix work hardens effectively then much more strengthening is required to exceed σ_{mu}, and V_{crit} is large. Therefore, V_{crit} is of most importance where composite tensile strength is the criterion.

The fibers in the composite are discontinuous, the rule of mixtures cannot be applied. The ultimate strength of a given fiber can be utilized if it lies parallel to the tensile axis, and if its length exceeds a critical fiber length. Critical fiber length is defined as the minimum fiber length in the composite which can just be loaded to its failure stress. The stress-strain state at the fiber end does not correspond to the condition of equal tensile strain. When the tensile load is applied, the strained matrix region cannot instantaneously transfer tensile load, in an amount equivalent to that borne by continuous fibers, to the fiber at the fiber termination-matrix interface. Instead, tensile force is transmitted from the matrix to the fiber by means of shear stresses which develop at the fiber-matrix interface due to very different elastic modulii. The tensile force borne by the matrix deforms it and the matrix is displaced relative to the fiber along this interface. The relative displacement is zero at the fiber midpoint and a maximum at the fiber ends. The displacement results in an interfacial shear stress, greatest at the fiber ends, that is capable of transmitting tensile load to the fiber. The manner in which this occurs is shown schematically in Figs. 10 [76] and 11. Two consequences of this dominate the performance of discontinuous fiber composites: (1), a portion of each fiber, near its ends, will not be fully loaded and will thus be ineffective in strengthening the composite, and (2) the nature of fiber/matrix bond is of critical significance in determining the strength.

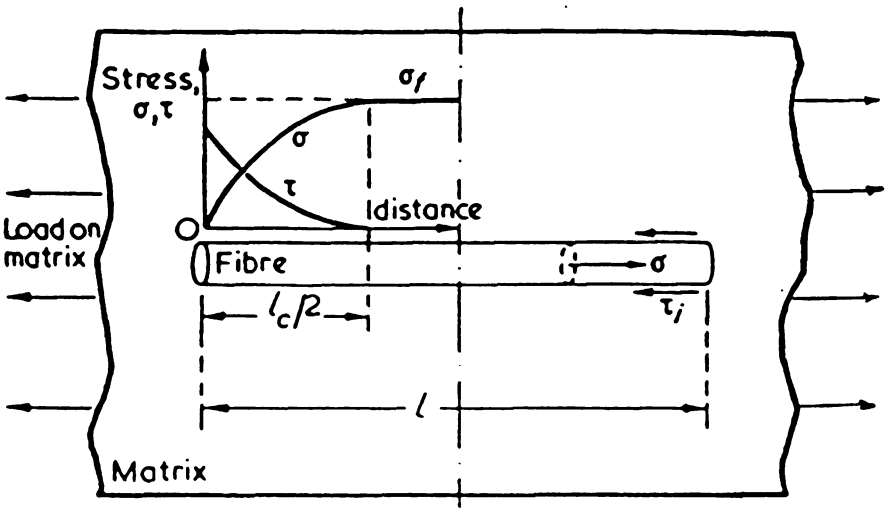

Fig. 10. Schematic illustration of the distribution of fibre tensile stress (σ) and interface shear stress (τ) along a short fibre embedded in a matrix (Ref. 76).

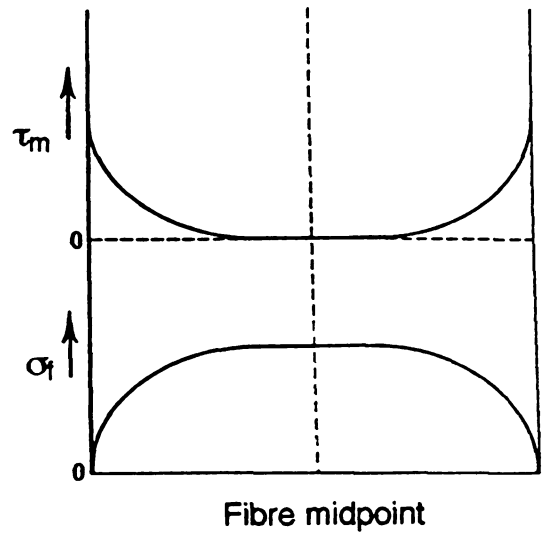

Fig. 11. The variation of τ_m and σ_m with position along the fiber when the matrix (and fiber) deforms elastically.

Various theories have been proposed to account for the detailed variation of the fiber and interface stresses, but for most purposes these can be represented by a simple linear function. If ß is defined as the build-up of tensile stress in the fiber, the strength of a discontinuous fiber composite can be written as:

$$\sigma_c = \bar{\sigma}_f V_f [1-(1- ß) l_c/l] + \sigma_{mu} V_m, \quad V_f > V_{min} \qquad (9)$$

In this expression, l_c is the critical fiber length (a fiber shorter than this cannot be loaded to its breaking stress) and $\bar{\sigma}_f$ is the mean fiber stress. If the length exceeds a certain critical length, the fiber midpoint, and regions adjacent, experience a tensile stress corresponding to the equal-strain condition. The value of σ_f is determined by the fiber and matrix properties through the relationship:

$$l_c/d_f = \sigma_f/2\tau \qquad (10)$$

where d_f is the fiber diameter and τ is the interfacial stress. Clearly if $l >> l_c$, equation (9) becomes equal to equation (6) or (7). Determination of how effective discontinuous fibers are, requires knowledge of l_c/d_f, where l_c/d_f is called the critical aspect ratio. Fig. 12 schematically illustrates the effects of several variables which control the strength of the composite including: the fiber volume fraction, fiber strength and fiber length [76]. As this figure indicates, the maximum V_f obtainable decreases as the fibers become shorter.

If randomly oriented fibers are employed, the proportion of fibers, capable of being loaded to their fracture stress will be reduced, and hence the ultimate strength of the composite will be lower than that of an equivalent aligned

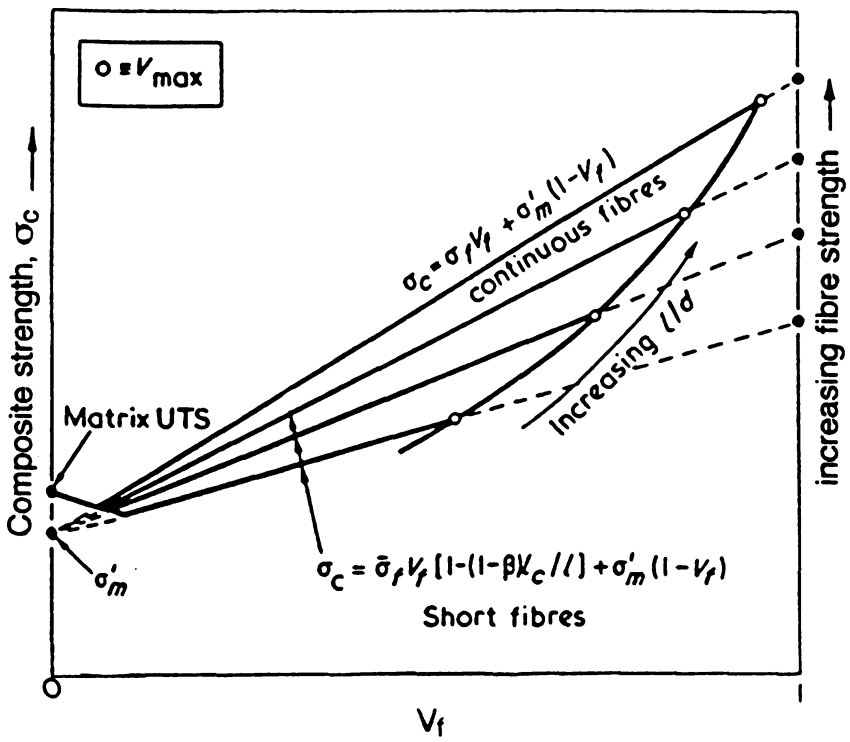

Fig. 12. The effect, (shown schematically), of fiber volume fraction, V_f, fiber length, l, and fiber strength, σ_f, on the strength, σ_c, of the composite (Ref. 76).

system. Suitable efficiency factors have been derived to take into account the effect of fiber orientation and fiber length.

2. 3. 2 Theory of energy absorption mechanisms

The incorporation of low modulus fibers into relatively high modulus ceramic materials was originally carried out in order to increase the fracture toughness, rather than the strength of these brittle materials. Fibers are effective in providing barriers to crack propagation and thereby improve the fracture toughness of a material. Their precise role, however, is complex and difficult to describe or quantify fully.

There are a number of mechanisms by which the total work of fracture may be raised. In a poorly bonded composite, the stresses near the crack tip could cause the fibers and matrix to debond from each other before the fibers break. When total debonding occurs, the elastic strain energy in debonded lengths of the fiber cannot redistribute stored energy in the rest of the composite. When the fiber snaps in the debonded region, the energy is dissipated as heat.

Fiber stress relaxation, a variation of the debonding model, estimates the stored elastic energy lost from a snapped fiber when the interfacial bond is not destroyed and elastic energy is lost by the fiber over its critical fiber length. It is also possible for a matrix crack to propagate past a fiber leaving it unbroken and bridging the crack. Crack bridging can result in toughness by a combination of a process described above.

Another mechanism which can enhance the toughness is to increase the effective crack propagation area. This can occur by having planes of weakness within the material, in a direction parallel to the tensile axis along which a

propagating crack may be deflected, thereby effectively blunting crack tips. Aveston has shown [77] that very high values for the work of fracture are possible by this mechanism.

If the fiber-matrix bond is sufficiently strong, a crack may propagate relatively unimpeded through the composite, and the work of fracture or toughness will be low. An increased bond strength would be expected to increase the interfacial shear strength and decrease the debonded length in the debonding model. In that case, the critical fiber length, l_c would be decreased.

If discontinuous fibers of length l, where the length is less than the critical length, l_c, the fibers will not be loaded to their fracture stress and they must be withdrawn from the matrix as the fracture planes separate. It has been shown by Cottrell [78], that the contribution due to pull-out can be very significant, and the maximum value γP_{max}, is obtained for $l = l_c$, when

$$\gamma P_{max} = V_f \tau l_c/12r \qquad (11)$$

where τ is the interfacial shear stress resisting pull-out, and r is the fiber radius. If the fiber length $l > l_c$, some pull-out is still observed, since many of the fibers will intersect the crack plane within a distance $l_c/2$, and hence a fraction l_c/l of the fibers will not be loaded to their fracture stress, and must pull-out as the planes separate. The fact that pull-out effects have also been observed for many continuous brittle-fiber systems, has been attributed to the statistical distribution of strength along these fibers, allowing fracture of many fibers to occur at positions away from the fracture plane.

In the case of ductile reinforcing fibers, a large contribution to the fracture toughness of the composite may be provided by plastic flow and rupture of the fibers. For fibers of length, $l > l_c$, the contribution, γ_f, due to fiber rupture will be

$$\gamma_r = V_f \gamma_f (l - l_c/l) \qquad (12)$$

where γ_f is the rupture energy.

In composites with random fiber orientation, many fibers will cross the fracture plane obliquely and will be subjected to a bending moment. For the case of brittle fibers this will have the effect of lowering the applied tensile stress required to fracture the fibers. For ductile fibers, plastic bending may accommodate the extra strain at the convex portion of the fibers during withdrawal from the matrix, and may contribute significantly to the total work of fracture. If fibers make a small enough angle to the fracture plane, they will either fail in shear, or will break through the matrix. It has been shown that the maximum work of fracture due to pull-out of aligned ductile fibers of critical length is significantly greater than that which can be obtained by plastic bending alone of misaligned fibers. However, the deformation of misaligned fibers can make a substantial contribution to the work of fracture when fibers of less than the critical length are employed, and would not yield very high values when aligned.

Unfortunately, with randomly-oriented reinforcement, some fibers will lie approximately perpendicular to the tensile axis and may act as stress-concentration sites, particularly if bonding is weak, consequently reducing the strength of the composite. In general, reinforcement of ceramics by metal or ceramic fibers, although providing a substantial improvement in fracture toughness, particularly when using metal reinforcement, often leads to little improvement, or even a reduction, in the mechanical strength [79]. This is because the relatively large diameter fibers employed, normally greater than 50 μm and often as large as 200 μm, acted as stress concentration sites which weakened the matrix and toughness was therefore increased at the expense of strength. Significant

strengthening was possible due to a combination of factors, including the influence of small size and the large difference in elastic modulus between high modulus of reinforcing fibers and the relatively low modulus of the matrix.

Of the above energy absorption models, debonding and pull-out mechanisms have been most widely accepted. Table 1 summarizes various theoretical models for energy absorption mechanisms which was studied by a number of researchers.

2. 3. 3 Stress-strain curves of fiber reinforced composites

For a suitable combination of the toughening mechanisms described above, a non-catastrophic mode can be obtained, as characterized by the tensile stress-strain curve of Fig. 13 [80]. Qualitatively, this failure mechanism is favored in composites with weak interfaces, high strength fibers and tensile residual stresses normal to the fiber/matrix interface. Changes in any of these parameters can lead to a transition in failure mechanism to one which is catastrophic, with a linear stress-strain curve to failure.

There are generally three regions of failure in fiber reinforced composites: (1) linear stress strain behavior before matrix cracking (BMC), (2) nonlinear region with increasing stress and strain after multiple matrix cracking (AMC) occurs with possible crack deflections at the fiber-matrix interface, and (3) a region of decreasing stress with increasing strain where fiber pullout (FP) is occuring. For each fiber (or a bundle of fibers) pullout in region 3, a slight decrease is seen in stress locally as the general load is also decreasing.

The initial departure from non-linearity in both types of stress-strain curves results from cracking of the matrix. For the non-catastrophic mode of failure, the first crack in the matrix extends indefinitely, breaking only a small

Table 1

Theoretical models of energy absorption associated with mechanical deformation of fiber reinforced composites

Model	Fracture surface energy γ
Pull-out (short fibers of length l)	$\frac{V_f \sigma_f l_c^2}{12 l}$ $(l > l_c)$ $\frac{V_f \sigma_f l^2}{12 l_c}$ $(l < l_c)$
Debonding	$\frac{V_f \sigma_f {}^2 y}{4E_f}$
Stress-relaxation	$\lesssim \frac{V_f \sigma_f {}^2 l_c}{6E_f}$
Crack-bridging	$\frac{2V_f r \sigma_f {}^3}{\tau_i E_f} \times \frac{(1+\gamma_f)(1-2\gamma_f)}{12(1-\gamma_f)}$
Matrix plastic deformation	$\frac{(1-V_f)^2}{V_f} \times \frac{\sigma_m r}{\tau} \times U$

V_f : Volume fraction of fiber
E_f : Young's Modulus of fiber
r : radius of fiber
τ : Shear strength of metal matrix
y : Debonded length of fiber
U : Work of fracture unit volume of metal matrix
τ_i : Fiber-matrix interfacial shear strength
σ_f : UTS of fiber
γ_f : Poisson's ratio of fiber
σ_m: UTS of metal matrix
l_c : Critical transfer length

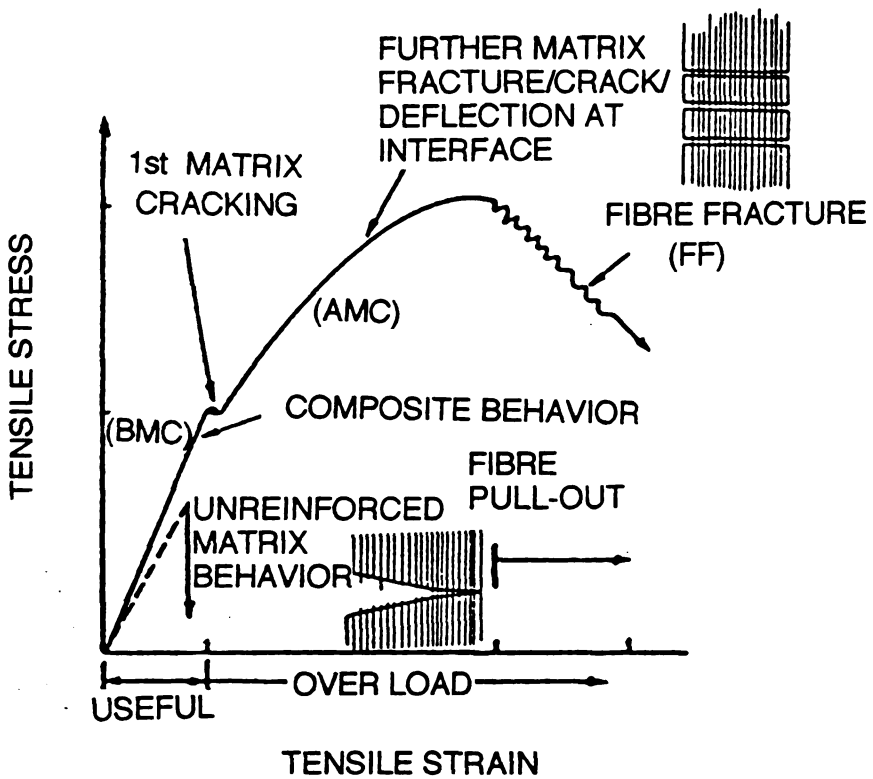

Fig. 13. Idealized stress-strain behavior of a ceramic matrix composites (Ref. 80).

fraction of fibers [81,82]. The increasing non-linear portion of the stress-strain curve is dictated by the properties of the fibers, as qualified by frictional interactions with the matrix block. The ultimate strength is determined by the fiber bundle failure. The tail of the curve corresponds to pullout of broken fibers. If, on the other hand, a substantial proportion of the fibers break in the wake of the first matrix crack as it extends, then the failure of the composite is catastrophic.

2. 3. 4 Testing methods

2. 3. 4. 1 Tensile strength

To characterize the tensile properties of ceramic composites, test fixtures and a specific specimen configuration will be required. The modification that have to be considered are the size limitations of material available for testing, the difficulty of machining holes in a test specimen, and the difficulties with machining fiber composites for dimensional requirements of the test specimen. Almost all the difficulties associated with tensile testing may be attributed to premature failures near the grip areas due to stress concentration and deviations from the uniaxial stress conditions caused by misalignments. Some efforts were made to develop a suitable tensile grip to prevent cracking of the specimen, at the grip. Sashedri et al. [83] developed a simple, self-aligning, uniaxial test fixture that produced nearly zero bending moments during tensile tests.

2. 3. 4. 2 Flexural strength

The bending test is commonly used for brittle ceramics materials because it does not require gripping the specimen, and hence it is less complicated to perform. It should be pointed out that bending tests are subjected to the following assumptions [84]:

1). The material is homogeneous and isotropic.

2). Plane sections remain plane after deformation.

3). The material exhibits a linear stress strain relationship, so that the linear elastic fracture mechanics can be applied.

In most composites, (particulate, chopped fibers and whisker reinforced), if the fibers or whiskers are distributed randomly in three dimensions, then the composite could be approximated as isotropic. In that case determination of two elastic constant are sufficient for a complete stress-strain description [85]. However, continuous fiber reinforced composites are highly anisotropic and generally orthotropic, i. e., having three mutually perpendicular planes of symmetry [86]. Therefore, it is necessary to determine 9 independent elastic constants.

While the bending test methods possess a number of features which make them very attractive and therefore commonly used for testing composite materials, the flexural strength is not generally recommended for producing design data. However, this method is useful in simulating actual behavior during service conditions. Because of the nature of ceramic composites, tensile and flexural tests generally will not give results which will lead to the same conclusions concerning the performance of these materials [87]. The ultimate flexural strengths are generally higher than the ultimate strength value. However, as the span to depth ratio increases, flexural strength approaches the tensile strength asymptotically.

Marshall and Evans [87] investigated failure mechanisms in a unidirectional SiC-fiber/glass-ceramic composite. These experiments showed that failure in tension occurs in several stages: multiple matrix cracking, followed by fiber fracture and pullout. In flexural loading, the failure process was more complex. Main factors affecting these results were related to the supporting span to depth ratio. Beam specimens, which satisfy the above assumptions, are used to develop both flexural and shear properties, with the span to depth ratio governing the mode of failure. A short beam test is usually designated for measuring the ultimate interlaminar shear stress, while a high span to depth ratio is selected for testing ultimate tensile or compressive stresses. The effects of the absolute thickness and width of the beam are disregarded here, because their contributions, are negligible compared with that of the span to depth ratio. The maximum tensile stress, σ_m, derived from the beam theory, is given by:

$$\sigma_m = 3PL/2bd^2, \quad \text{for 3-point loading,} \tag{13}$$

$$\sigma_m = 3PL/4bd^2, \quad \text{for 4-point loading at quarterpoints,} \tag{14}$$

where P is the fracture load, L is the span width, and b and d are the specimen width and depth respectively. The flexure standards recommended by Naval Research Lab. [88] are:

(1) 1/3 span, 4-point flexure, with span to depth of 21 - 23, for tensile strength measurement,

(2) 3-point flexure with span-to depth of 3.9 ± 1.8 for tensile strength determination, and

(3) 4-point flexure with span-to-depth of 12 - 14 for K_{Ic} determination using a single notch beam technique with 0.15 mm wide and, 0.4 - 1.0 mm deep notch.

A schematic diagram of a 3-point and a 4-point bending tests are shown in Fig. 14. According to experiments conducted at the Naval Research Lab. [88], the strengths obtained by short span, 3-point flexure falls sharply below those obtained by long span, 4-point flexure. This is because errors due to beam deflection, mixed-stress fields (especially shear components), rate of stress and changing directions of load application became more pronounced in a 3-point flexure. The 3-point flexure configuration is more complicated by the the presence of shear stresses as shown in the shear and moment diagrams (Fig. 14). This is unlike the pure bending in a 4-point set-up, where the inner span of the specimen experiences pure bending. Because of this the 4-point flexure experiment is more commonly used than the 3-point flexure test.

2. 3. 5 Fracture toughness

Fracture toughness is an important material property which characterizes the resistance of the material to crack propagation. It is convenient to define a parameter K, given by:

$$K = Y\sigma\,(\pi c)^{1/2} \qquad (15)$$

where the parameter K is called the stress intensity factor, σ is the critical stress, Y is a dimensionless parameter that depends on both the specimen and crack geometry and c is the crack length. For simplicity Y is assumed to be 1. Equation (15) describes the degree of stress intensification that occurs near the border of the crack when a tensile stress is applied at the ends of the specimen. Unstable fracture occurs when K reaches a critical value K_c. This critical value K_c is termed the fracture toughness.

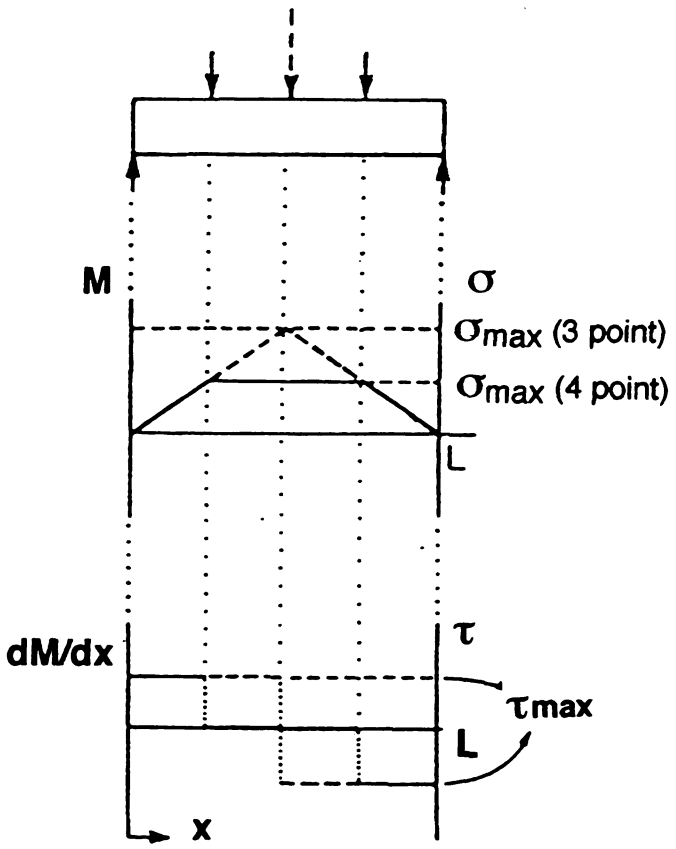

Fig. 14. The schematic diagram of the 3-point and the 4-point bending mode.

For relatively thin specimens, the value of K_c will depend on the thickness, B. However, K_c becomes independent of B above a certain critical value of specimen thickness. The constant K_c value for thicker specimens is known as the plane strain fracture toughness, K_{Ic}, which is also defined by

$$K_{Ic} = Y\sigma (\pi c)^{1/2} \tag{16}$$

The I subscript in K_{Ic} denotes that this critical value of K is for mode I (opening mode) crack displacement. Also plane strain fracture toughness, K_{Ic}, may be expressed in the form:

$$K_{Ic} = (EG_c)^{1/2} \tag{17}$$

where E is Young's modulus and G_c is the critical amount of work which needs to be done at the crack tip for fracture, or the critical rate of release of strain energy. G_c is equivalent to the fracture surface energy, γ, as follows:

$$G_C = 2\gamma \tag{18}$$

The fracture stress is then given by:

$$\sigma_F = (EG_c/\pi c)^{1/2} \tag{19}$$

As pointed out before, the above equations are based on the linear elastic fracture mechanics (LEFM). For an isotropic material, the stress intensity factor is related to the fracture surface energy and the Young's modulus under plane strain condition as given in eq. (16) or Young's modulus and Poisson's

ratio under plane stress condition. For an elastically anisotropic material, in plane stress, it has been shown [89] that the relation between K and G_c is more complicated.

The stress intensity factor, K, is a more useful concept for the design engineer than the fracture surface energy, γ, (or G_c). But the fracture surface energy can be more directly related to the microscopic fracture processes. Usually the stress intensity factor, K, is expressed as K_{Ic} in terms of unstable opening mode crack extension under plane strain conditions.

It is necessary to develop specifications for valid K_{Ic} testing because real materials do not deform in elastic-brittle manner assumed in linear elastic fracture mechanics. Nevertheless, when a sufficiently large crack-notched specimen is tested, the behavior is sufficiently close to elastic-brittle because the crack tip plastic zone remains small relative to the significant specimen dimensions. However, it is inappropriate to apply the ideas of toughness testing to continuous fiber ceramic matrix composites. This is because failure in composites is a complex, unlocalized process. For short fiber composites, the techniques used for measuring the toughness of homogeneous ceramics are valid and do not present any problem because most of the damage during failure occurs close to the macroscopic fracture surface and macroscopic cracks tend to deviate from their intended paths into the weak directions.

Several tests are available for determining the fracture toughness. The choice of technique is dictated by several factors among which one of the most important considerations is the type of information needed. Specimen geometry used in fracture toughness testing of ceramics, varies according to the type of information desired. Double cantilever beam specimen yields information relating applied stress intensity, K_a, to crack length or crack velocity, while fracture toughness value, K_{Ic}, is obtained by using single edge notched and chevron

notch techniques. A double torsion specimen yields both K_{Ic} and crack velocity, V, data.

An important aspect of specimen preparation is precracking. All tests are based on the assumption that the stress to cause a sharp crack to propagate through the material is measured. Fig. 15 [90] shows the different types of specimen geometry for fracture toughness measurements. Table 2 summarizes various commonly used test methods for fracture toughness.

2. 3. 5. 1 The double cantilever beam (DCB) test

This test is run by applying a tensile opening load to one end of the specimen, causing a crack to propagate down its midplane. The load can be applied either through holes drilled through the specimen or tabs glued to its ends. A side groove is usually placed in the specimen to ensure that the crack will propagate along the mid-plane. The applied stress intensity, K_a, at the crack tip can then be calculated.

2. 3. 5. 2 The single edge notched beam (SENB) test

The procedure is similar to a 3 or a 4-point bend test except that an artificial crack is placed in the specimen before testing. The initial cut (crack) is usually made by sawing with a diamond impregnated blade or a wire. In the simplest variation of the test, the specimen is fractured and the depth of the cut is used as the initial crack length. This approach, however, often leads to invalid results because the K_{Ic} value determined in this fashion depends on notch width. The experimentally determined K_{Ic} value decreases with the notch radius until a critical notch radius is reached, below which K_{Ic} is independent of the notch radius. This problem can be eliminated by initiating a sharp crack at the base of the notch. This may happen naturally as a result of

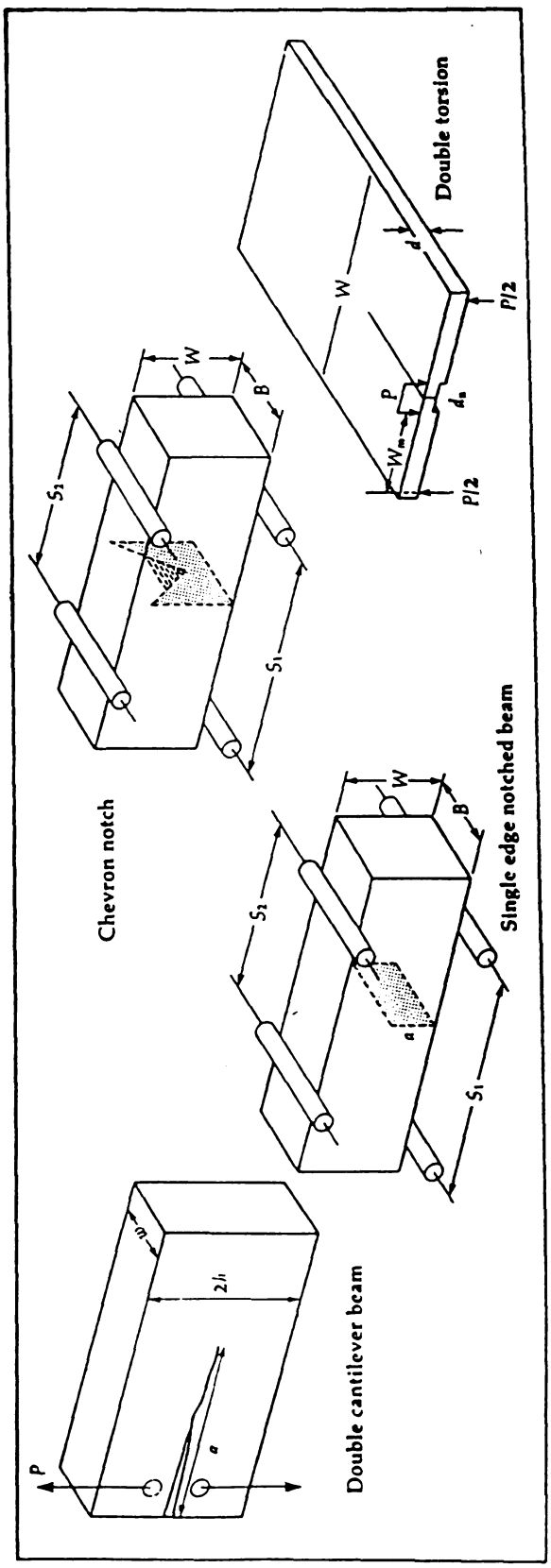

Fig. 15. The different types of specimen geometry for fracture toughness measurement (Ref. 90).

Table 2.

Test methods for fracture toughness measurements [Ref. 90]

Test method	Parameter/ property determined	Equation	Variables
Double cantilever beam	Applied stress intensity (K_a)	$K_a = \left(\frac{\sqrt{12\,Pa}}{\sqrt{w\,w'\,h^3}}\right)\sqrt{1 + 1.32\,(h/a) + 0.542\,(h/a)^2}$	P is applied load, a is crack length, w is specimen width, w' is the width of the grooved section, and $2h$ is specimen height
Single edge notched beam	Fracture toughness (K_{Ic})	$K_{Ic} = \frac{3P\,(S_1 - S_2)}{2BW^2}\,a^{1/2} \cdot Y$	B is specimen thickness, W is specimen height, S_1 and S_2 are the outer and inner roller spans, and Y is a calibration factor
Chevron notch	K_{Ic}	$K_{Ic} = \frac{P\,(S_1 - S_2)}{BW^{3/2}}\,Y_m^*$	Y_m^* is a geometric factor determined by specimen compliance
Double torsion	K_I	$K_{Ic} = PW_m\left(\frac{3(1+\nu)}{Wd^3d_n}\right)^{1/2}$	ν is Poisson's ratio, W_m is the moment arm, d is specimen thickness, and d_n is the thickness of the groove
	Crack velocity (V)	$V = \frac{-a_i P_i}{P^2}\left(\frac{dP}{dt}\right)$	a_i is initial crack length, P_i is initial load, and dP/dt is the load relaxation rate
Indentation (crack length)	K_{Ic}	$K_{Ic} = \chi\left(\frac{E}{H}\right)^{1/2}\left(\frac{P}{c^{3/2}}\right)$	χ is a constant, c is crack length, E is Young's modulus, H is hardness, and P is indentation load
Indentation (strength)	Resistance to crack growth (K_c); K_{Ic}	$K_{Ic} = \eta\left(\frac{E}{H}\right)^{1/8}\,(\sigma P^{1/3})^{3/4}$	η is a constant, and σ is fracture stress

sawing, or an additional procedure such as wedge loading or thermal stress may be needed. The length of the precrack must be about half the notch radius to give a valid result.

A second factor that influences notched beam tests is loading rate. If the load is applied too slowly, there is a possibility of slow crack growth during testing. This results in an underestimation of K_{Ic} because the actual critical crack length will be no longer than that measured before applying the load.

2. 3. 5. 3 Chevron notch beam (CNB) test

Like the SENB test, this test is performed with a bar in which a chevron notch (rather than a straight-through notch), is machined into the specimen which is shown in Fig. 16. The unique feature of chevron notch specimens is the extremely high stress concentration at the tip of the notch. As a result, the stress intensity factor passes through a minimum as the crack grows. Because of the high stress concentration at the tip of the chevron notch, the crack starts at a very low load and thus precracking of the specimen is not necessary. As long as the notch is large enough to cover many fibers at the critical crack length, this should be a useful test. However, the major disadvantage of chevron notch beam test is notch machining difficulty in specimen.

2. 3. 5. 4 Double torsion test

In this method, the test specimen is a rectangular plate, typically with a length three to four times the width. A center groove is often used to guide the crack, but can be eliminated if thin specimens are used and the specimen is aligned carefully in the fixture. As with other fracture toughness tests, the specimen must be precracked before determining K_{Ic}. The main difficulty with

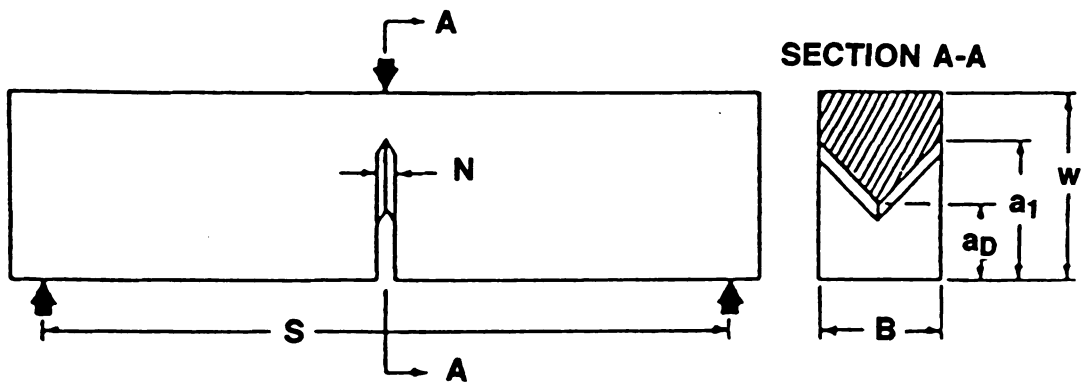

Fig. 16. Schematic of chevron notch flexural beam for the determination of fracture toughness.

double torsion testing is that the crack propagates with a curved front, extending further along the tensile surface than along the compressive surface.

2. 3. 5. 5 Indentation test

In this method, there are two main variations. These are: (1) the indent crack length method, and (2) the indentation strength method. Both methods rely on the formation of a well-defined crack pattern around the impression made by a diamond indenter, most often by a Vickers square pyramid. The crack length method requires the measurement of the radial crack traces that appear to emanate from the corners of the indenter. The residual stresses accompanying the indentation provides the driving force for crack growth. The attractive features of this approach are that there are no practical specimen size limitations, and that both the position and size of the cracks are easily controlled.

One of the drawbacks in this method, is that it requires crack length measurement, which can be difficult and tedious. A second point is that residual stresses from the indent can cause subcritical crack growth. If this occurs, the measured crack lengths will be longer than the equilibrium crack lengths, and K_{Ic} will be underestimated.

The indentation strength method eliminates both the need to measure crack length and the problem of subcritical crack growth. This technique uses the indentation-produced crack system as a controlled flaw in a strength test. Of particular importance in this test is the role of the residual stress associated with the indent, which provides a stress intensity at the crack tip in addition to that provided by the externally applied stress. The residual stress intensity, however, decreases as the crack extends. This decrease causes the crack to grow stably to a critical length before unstable fracture, thus eliminating initial crack

length as a critical factor and obviating the need for crack length measurements. Fracture toughness is calculated after the strength of the indented specimen is determined.

3. EXPERIMENTAL PROCEDURE

3. 1 Sample Preparation

The superconducting composite samples were prepared by using two different processing techniques: one by conventional sintering and the other by using hot isostatic pressing (HIP).

3. 1. 1 Sample Preparation (conventional sintering)

The starting powders of $YBa_2Cu_3O_{7-x}$ were prepared by mixing 99. 99 % purity Y_2O_3, $BaCO_3$ and CuO powders (Aldrich Chemical Co.) in appropriate amounts. A mortar and pestle was used for grinding and mixing. Well-mixed powders were calcined at 930°C in air atmosphere for 24 hours, reground and recalcined at 930°C for 24 hours. Calcined powder particles (after second calcination) were then passed through sieves to get a particle size of less than 30 μm. Four different compositions, 5, 8, 12 and 15 volume %, of 50 μm diameter chopped silver fibers (around 10 mm length) were randomly distributed into the calcined 1-2-3 powder. The fibers were then thoroughly mixed with 1-2-3 powders in acetone solution by a magnetic stirrer. The acetone was quickly evaporated resulting in powder-fiber mixture. The mixture was then further dried in a furnace at a temperature of 200°C to remove the remaining acetone. The dried mixture was then compacted in a closed stainless steel die at a pressure of 130 MPa to form a rectangular bar (6 mm x 9 mm x 38 mm). Following that, a solid state reaction/sintering was performed by heating the bar at 925°C for 10 hours in air and subsequent slow cooling to room temperature inside the furnace.

Several different volume % Ag fibers were mixed into the 1-2-3 compound. However, it was found that when the volume % of Ag was more than 15 %, a good compaction of Ag and 1-2-3 mixture could not be achieved. The tangling of short size Ag fibres was the most serious difficulty in producing a random distribution when the volume % of Ag fibers was > 15 %.

3. 1. 2 Sample Preparation (hot isostatic pressing)

For hot isostatic pressing and specimen preparation, an IPS Eagle-6 Hot Isostatic Press system (International Pressure Service, Inc.) was used. The Eagle-6 uses a 6 inch internal diameter stamped monolithic pressure vessel with threaded closures, rated around 200 MPa. This equipment is capable of reaching a temperature 2,000°C, using a graphite furnace, which is a modular plug-in unit with a hot zone measuring 3 inches in diameter and 4 inches in length.

Argon gas was used as the pressure medium. A microprocessor-based controller was utilized to control and monitor the process temperature, pressure, time, valve position, compressors, volts, amps and electrical contacts. Pressure and temperature was controlled by a programmed set point controller. A digital/analog strip chart recorder was used to record system pressure and temperatures as a function of time. Temperatures was monitored by using 5 different tungsten/rhenium thermocouples located at different levels within the furnace and the pressure vessel. Assigning a true temperature to the run was difficult because neither of the thermocouples is directly attached to the specimen. Therefore temperature, in our experiments, represents a bracketed temperature within which the upper and lower bounds. The uncertainty in temperature measurement was estimated approximately within ± 5 C of reported values.

Before HIP processing, given samples were conventionally sintered at 925°C for 2 hours only. The reason for this short presintering was to give some strength to the green compact so as to enable easier handling during further fabrication stages. The bar was coated with 99.99 % purity boron nitride using BN spray (Union Carbide Co.) and then it was wrapped with a 0.025 mm thick Cu foil (Aldrich Chemical Co.).

There are two main reasons for using the BN spray and Cu foil. One is to reduce the oxygen partial pressure, especially at high temperatures, by inducing the chemical reaction between Cu foil and residual oxygen to form CuO layer. The other is to easily remove the CuO layer from the surface of the specimen separated by the BN spray. The BN sprayed and Cu foil wrapped sample was placed into a 12 mm (I.D) diameter and 2 mm thickness pyrex tube. For easy decapsulation, high thermal conductivity BN powder (HCP, Union Carbide Co.) was placed between the Cu foil wrapped sample and the glass wall. The pyrex tube, with the sample, was evacuated for 20 minutes under a vacuum of 10^{-2} Pa and finally sealed by torch. The sealed capsule was placed into a specially designed rectangular type graphite crucible and carefully inserted into the heating zone of the graphite furnace. In the HIP, in the first stage, the system was evacuated for 30 minutes and then purged 3 times by argon gas. The pressure was kept low to avoid glass cracking as the temperature was raised to 820°C, which is the pyrex softening temperature. The applied heating rate was 8°C/min. Temperature and pressure were then raised up to 890°C and 170 MPa respectively and kept for 2 hours. At last, the temperature was slowly cooled to 500°C at a rate of 2.5°C/min and cooled down to room temperature. Pressure was vented. Figs. 17 and 18 show the detailed HIP processing cycle in terms of pressure, temperature and time. Specimens were removed from the glass wall of the capsule by using the grit blast method. After decapsulation, the

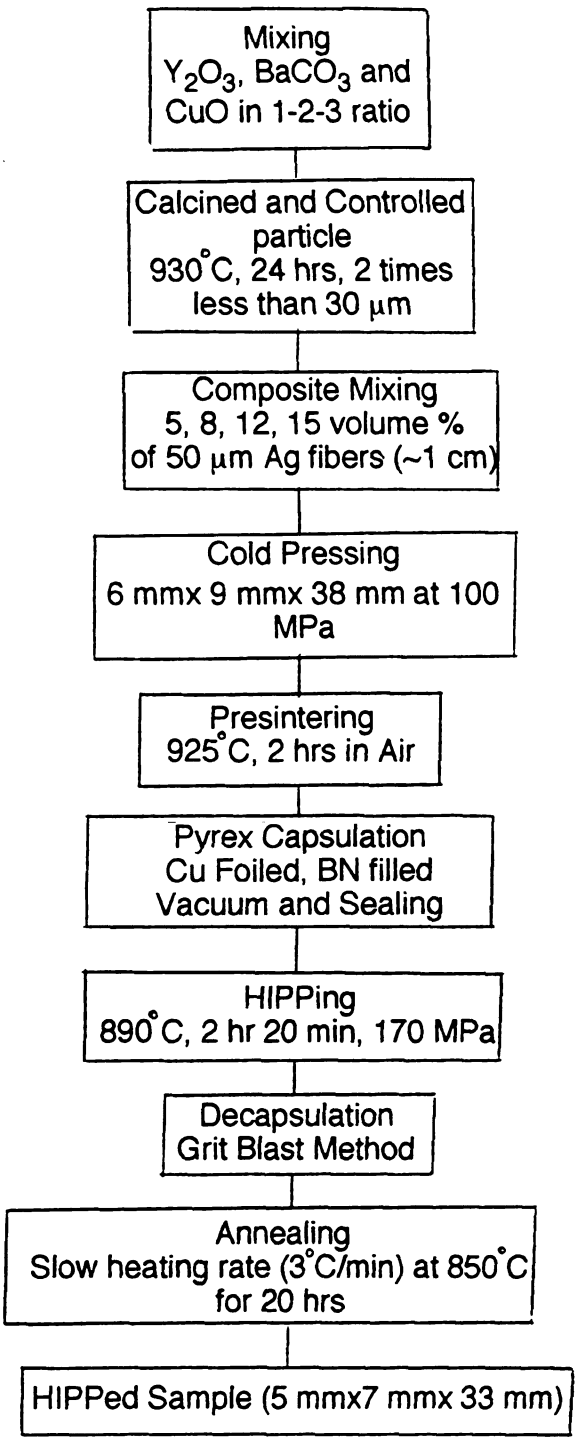

Fig. 17. Schematic diagram for the HIP processing cycle.

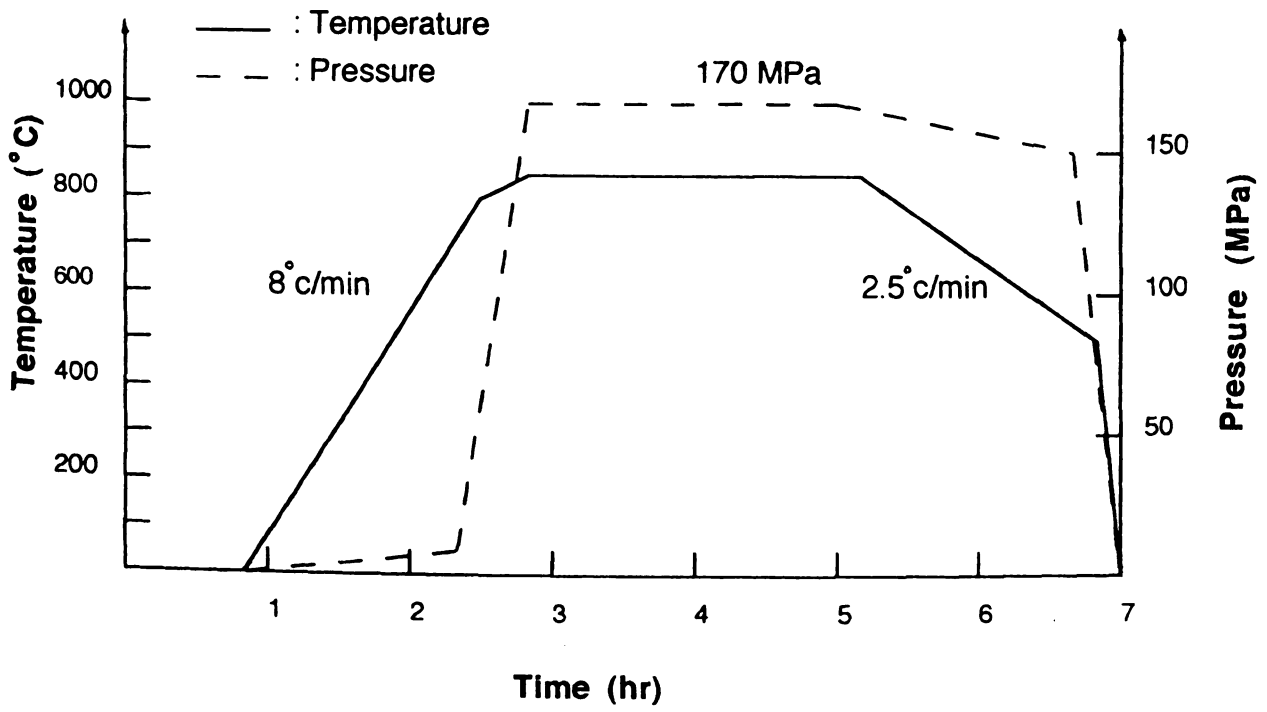

Fig. 18. Time-temperature-pressure profile during HIPing of Ag fiber reinforced $YBa_2Cu_3O_{7-x}$.

sample surface was found to be somewhat contaminated due to reaction with the glass wall and boron nitride. Typically, the color of the sample surface was green. This green phase was later identified as a mixture of Y_2BaCuO_5 (2:1:1) phase and CuO from x-ray experiments. However, this layer was usually less than 0.4 mm from the surface and disappeared during surface polishing and subsequent post-annealing processing. Annealing was conducted, at 850°C in air for 20 hours with a heating rate of 3°C/min. Typical dimensions of the HIPed specimens after annealing and polishing was 5 mm x 7 mm x 33 mm.

3. 2 Sample Characterization Methods

3. 2. 1 X-ray diffraction studies

For the structural analysis and phase identification, x-ray diffraction experiments were carried out by using a SCINTAG diffractometer (Scintac XDS 2000 diffractormeter, Scintac Co.) with a Ni filter CuKα radiation. A tube voltage of 35 kV and a tube current of 25 mA was used for all structural analysis. For diffraction studies of as-prepared samples, flat sample surfaces, which were mechanically polished, were used.

3. 2. 2 Electrical resistance measurements

The electrical resistance measurement was performed by using a standard four-probe technique (LR-400 four wire AC resistance bridge) on the regular geometry (5 mm x 7 mm x 15 mm) specimens.

Figure 19 shows the schematic diagram describing the experimental set-up for resistance measurement. Also, a schematic of the four-point probe is shown in Fig. 20. In this diagram (Fig. 20), four gold-plated pins were attached to the test specimen. The two outer pins were for current source and the inner two were for potential measurements. Four gold-plated pins and a calibrated T-type (copper-constantan) thermocouple were placed on the regular geometry of the specimen (5 mm x 7 mm x 15 mm). The specimen, thermocouple and pins were wrapped between two poly-vinyl chloride blocks (Fig. 21). All were then clamped by two plastic clamps and were immersed into the liquid nitrogen dewar for cooling.

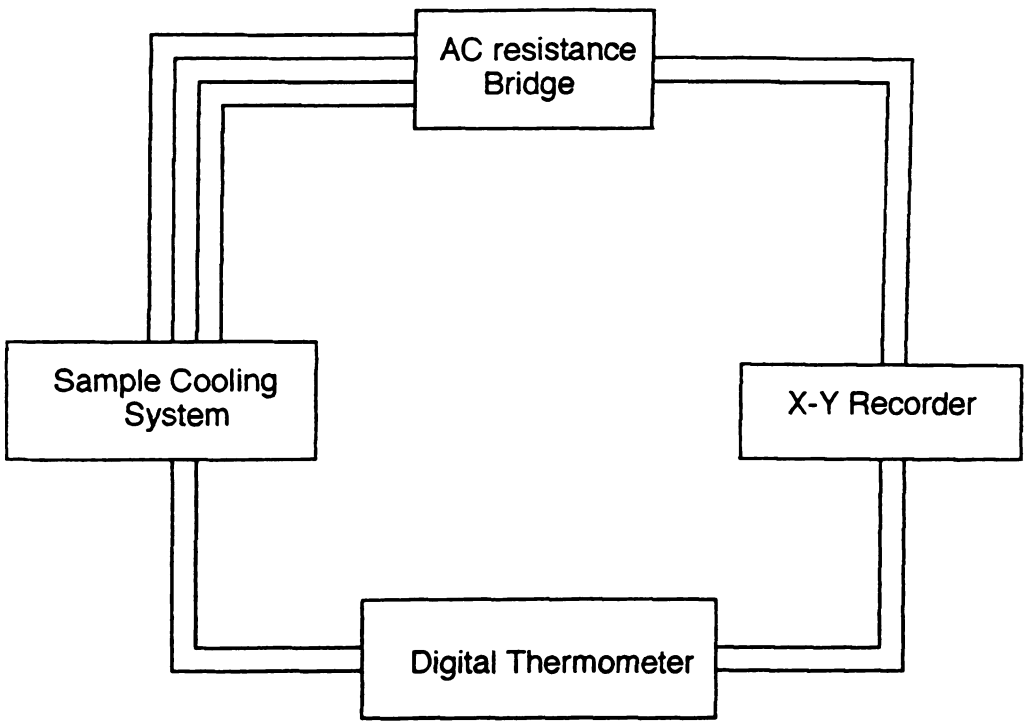

Fig. 19. Schematic diagram describing the experimental set-ups for resistance measurement.

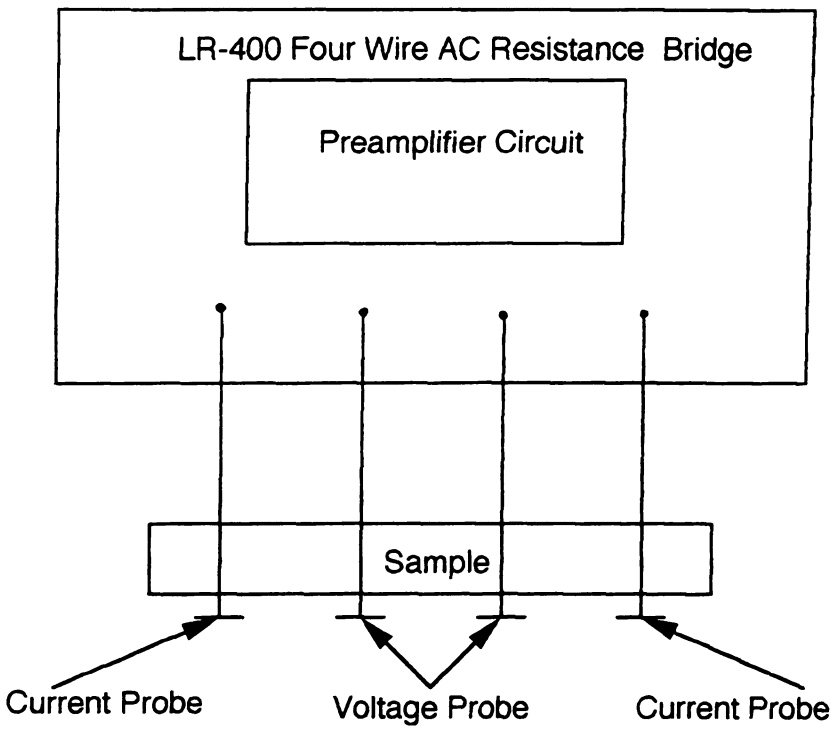

Fig. 20. Schematic of the four-probe technique.

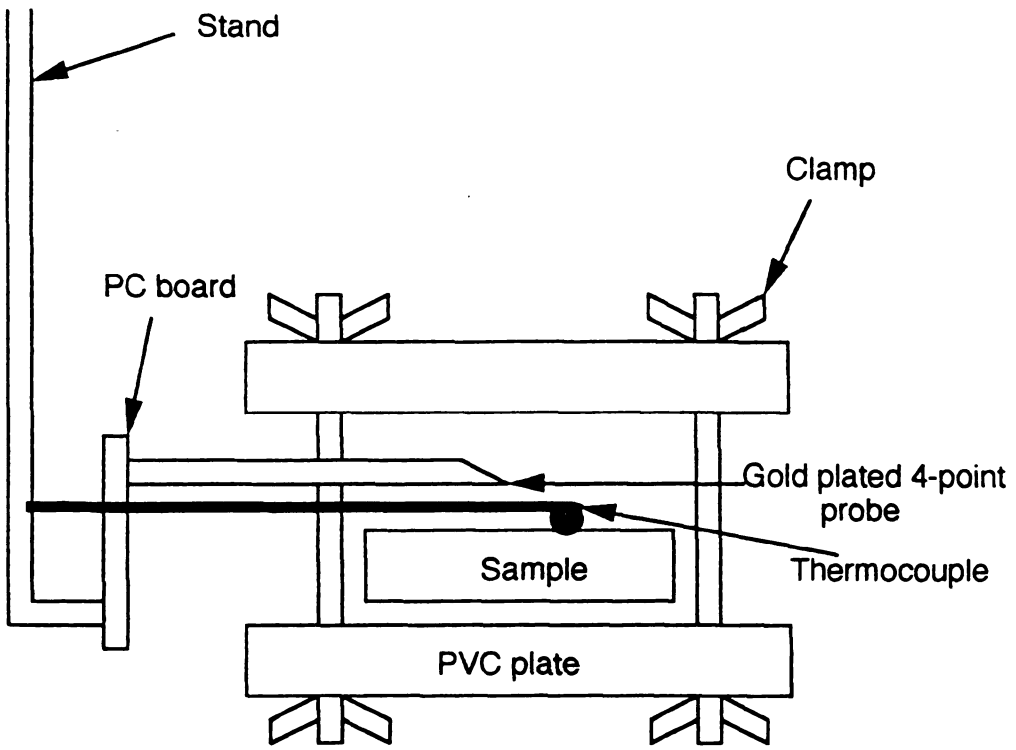

Fig. 21. Schematic diagram of sample holder assembly for AC resistance measurement.

The electrical resistance was monitored by using the LR-400 AC resistance bridge (Linear Research Inc.). The monitored resistance was calculated by the voltage drop caused by passing a given constant current, while the temperature was changed from the liquid nitrogens boiling temperature, 77 K, to room temperature. The applied current used for this experiment was 3 mA. Temperature was monitored by using a digital thermometer and the uncertainty in this measurement was estimated approximately within $\pm 1^{\circ}C$. Temperature vs. resistance (voltage) was continuously recorded by using a Houston Instrument 200, X-Y recorder.

3. 2. 3 Critical current density measurements

Critical current density was measured by using a standard four-probe technique at 77 K with zero magnetic field. The temperature was held constant at 77 K while the current through the sample was varied. Fig. 22 shows a schematic diagram of the critical current density measurement set-up.

A typical specimen size was 1 mm x 1.5 mm x 15 mm. The applied current range was from 0.2 to 9 Amp and the resistance was calculated from the voltage drop. The value of J_c was then deduced by dividing the critical current, at which the generated voltage was extrapolated to zero, over the effective cross section of specimen. In order to minimize the surface contact resistance, only the sample surfaces under contact were painted with Ag. The coated sample with Ag were then annealed at $450^{\circ}C$ for about 2 hours and slowly cooled down to room temperature in air atmosphere. Cu wire was then embedded into the Ag dispersed surface by Indium soldering. Ag dispersion by annealing was believed to have created the continuous network to give a stable bonding between the superconductor and the embedded wire.

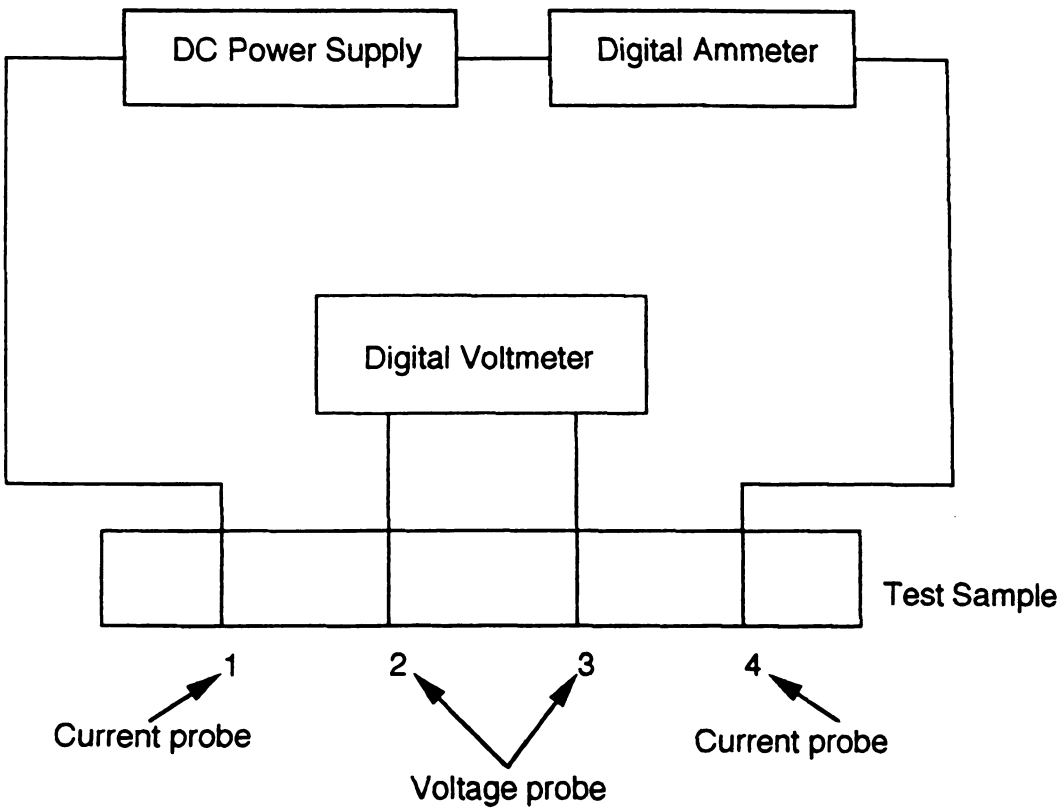

Fig. 22. Schematic diagram describing the experimental set-ups for critical current density measurement.

3. 2. 4 Magnetic moment measurements

The Meissner effect is a manifestation of the superconducting state. The Meissner effect is a phenomena in which the specimen expels all external magnetic fields when cooled through the superconducting transition point. Flux exclusion by a superconductor is the underlying principle associated with the Meissner effect, and is akin to a perfect diamagnetic state.

For the magnetic moment measurement, a Quantum Design Magnetic Property Measurement System (MPMS, Model 2000 VHF SQUID, Quantum Design) was employed. The MPMS is a sophiscated analytical instrument specifically designed for the study of the magnetic properties of small experimental samples over a broad range of temperature and magnetic fields. The system hardware has two major components: (1) the MPMS dewar and probe assembly, and (2) the associated control system in the MPMS control console (Fig. 23). Automatic control and data collection are provided by an HP computer and two independent subsystem controllers. Most of the gas control and other ancillary functions in the system are also automated. The cryogenic probe integrates a 5.5 Tesla superconducting magnet with a SQUID detection system and a high-performance temperature control system to provide rapid precision measurements over a temperature range of 1.9 to 400 K. Liquid helium provides refrigeration for the SQUID detection system and magnet, as well as providing for operation down to 1.9 K. The sample handling system allows automatic sample measurements and position calibrations using a microstepping controller having a positioning resolution of 0.003 mm. The equipment is capable of resolving variations in magnetic moments as small as 10^{-8} emu.

The measurement is made by inserting a pair of secondary coils into the sample area. Also, external to the secondary coil, is a long primary coil. The

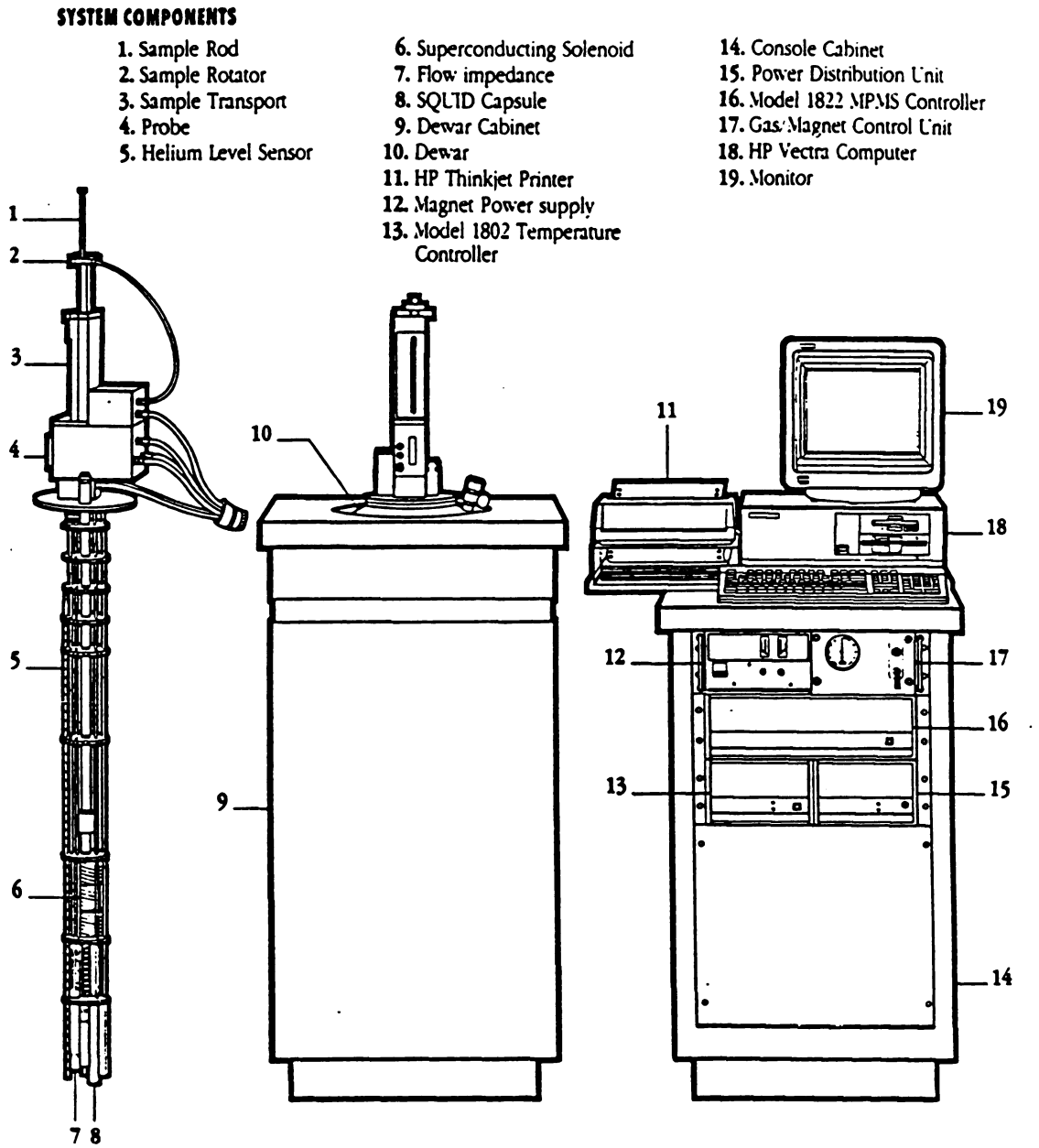

Fig. 23. Magnetic Property Measurement System (MPMS) components (Ref. 91).

sample is inserted into the center of one of the two secondary coils. A low-frequency current is passed through the primary coils. Any change in the flux linking or Meissner effect in the sample will yield a voltage (mutual inductance) in the secondary coils. A lock-in amplifier allows the magnetic susceptibility change to be detected.

For the magnetic moment measurement, about 1 gram of each different volume % Ag reinforced specimens were used. The samples were cooled down to liquid He temperature in a zero field and magnetization was measured from 40 K upon warming. The applied magnetic field used for this experiment was 20 G. The measurements were taken at 5 K intervals, from 40 to 50 K, 2.5 K intervals between 50 and 80 K, and 1 K intervals from 80 to 97 K. Standard deviation in this magnetic moment measurement was around 10^{-8} *emu*.

3. 2. 5 Density and porosity measurements

The density of each specimen, with different volume % Ag fibers, was measured according to ASTM B328-73 (buoyance method). About 2.5 grams of specimen was cleaned with acetone for 20 minutes and then completely dried. After cleaning, samples were weighed in air atmosphere (W_A) and immersed in SAE 10 W-40 motor oil (viscosity of approximately 200 SUS at 100 F) for 4.5 hour and held at 185°C. Then, the temperature was lowered to room temperature by immersion in oil at room temperature. The oil immersion introduces impregnation of the sample through interconnected pores (open pores). Following this, the excess oil was wiped off with a damp cloth and the samples were weighed again (W_B). The samples impregnated with oil, were then tied with a 0.09 mm diameter copper wire and suspended from the beam hook of a semi-micro balance. Samples were completely immersed into a beaker filled with

distilled water at 20°C, which was placed underneath the beam hook. The wired sample was weighed (W_C) and then the wire without the sample was immersed again into the distilled water for measurement (W_E). The density of sample can now be calculated from:

$$D = A/(B - C + E) \qquad (20)$$

where

D = density, g/cm^3

A = weight in air of oil-free specimen, g,

B = weight of oil-impregnated specimen, g,

C = weight of oil-impregnated specimen and wire in water, g,

and E = Weight of wire in water, g.

The measured density was compared with the theoretical density of Ag-$YBa_2Cu_3O_{7-x}$ which was obtained from the rule of mixtures. The porosity was calculated by subtracting the ratio of the measured density to the theoretical density from 1. Theoretical density of $YBa_2Cu_3O_{7-x}$ and Ag are 6.375 g/cm^3 [92] and 10.491 g/cm^3 [93] respectively.

3. 2. 6 Flexural strength and fracture toughness measurements

For strength measurements, specimens were unnotched. For fracture toughness measurements, the specimens were machined into the single edge-notched (SENB) configuration. Typical sample dimensions were 5 mm x 7 mm x 33 mm. Seven specimens, with the same volume % of Ag, were prepared for measurements. The notch was made by 0.016 mm thickness diamond blade, and the nominal notch depth was around 0.8 mm. An instron machine, at a

cross head speed of 0.05 mm/min was used for all fracture tests. The testing was carried out in a 3-point bending apparatus with a span width of 28 mm. Fig. 24 shows the schematic diagram for the 3-point bending apparatus. Strength and fracture toughness values were determined from the specifications stated in ASTM D790M-82. Typical span to depth ratio was kept to 6 : 1 in order to minimize the shear contribution to the fracture mode.

From beam theory, which is based on the linear elastic fracture mechanics under plane strain conditions, the fracture stress (σ_F) of the unnotched specimen was determined as follows:

$$\sigma_F = 3PL/2bd^2 \tag{13}$$

where P is fracture load. L is the span width, and b and d are the specimen width and depth respectively. Also values for K_{Ic} were measured by the following equation:

$$K_{Ic} = 3PL/2bd^2\ C_o^{1/2}\ Y(C_o') \tag{21}$$

where Y is the geometry factor related to the specimen, C_o is the notch depth and $C_o' = C_o/d$: relative notch depth.

The $Y(C_o')$ relation given by Gross and Srawley [94] is

$$Y(C_o') = 1.99 - 2.47C_o' + 12.97(C_o')^2 - 23.17(C_o')^3 + 24.8(C_o')^4 \tag{22}$$

The fracture energy parameter,γ, was estimated by examining the area under the load deflection curves.

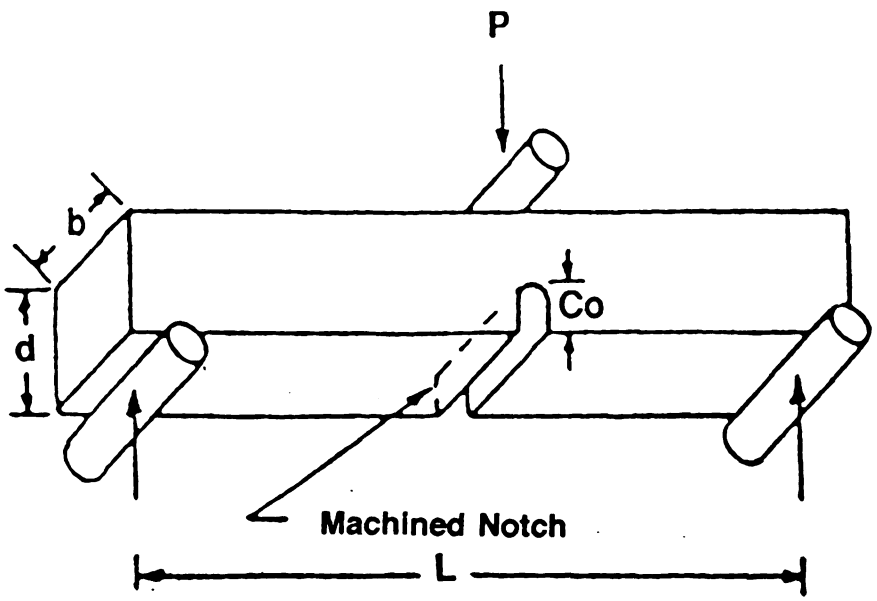

Fig. 24. Schematic diagram for notch-beam test in 3-point bending.

3. 2. 7 Morphological examination and EDAX analysis

3. 2. 7. 1 Optical microscopy

The microstructure was observed on the polished surface of the Ag reinforced specimens by using a Neophot-21 optical microscope (Leco Co.). Samples were metallographically mounted on a lucite block. Lucite mounted specimens were then polished on a nylon cloth with 1 to 5 μm alumina powder and 0.3 - 0.5 μm diamond paste. Methanol was used to prevent any possible degradation of the microstructure due to moisture pick-up.

3. 2. 7. 2 Scanning Electron Microscopy and EDAX

A HITACHI S-2500 SEM with Link energy dispersive x-ray spectroscopy was used to examine the microstructure and for the presence of elements on the fracture surface of the Ag reinforced specimens. Fractured specimens were mounted on cylindrical aluminum stubs. Silver paint was used for electrical contact to ground and also to provide a better mechanical support.

3. 2. 8 Scanning Auger Electron Microprobe

Qualitative analysis was carried out to obtain information about the interface and elemental distributions by using a Scanning Auger Multiprobe (SAM) (PHI 660, Perkin-Elmer Corp.).

AES (Auger Electron Spectroscopy) is a very powerful technique often used together with XPS (X-ray Photoelectron Spectroscopy) for surface chemistry studies. The basic principle of the Auger effect is the de-excitation of an

ionized atom by a non-radiative process. When an electron is ejected from an inner shell of an atom by photon or electron bombardment, the resultant vacancy is simultaneously filled by an electron from one of the outer shells (Fig. 25). The energy released in this decay process is transferred to a third electron that is emitted outside of the sample (the Auger electron). A simplified model for calculation of Auger electron energy was developed by Burshop [95]. The basic equation in this model is:

$$E^Z(XYZ) = E^Z(X) - E^Z(Y) - E^Z(V') \qquad (23)$$

where $E^Z(XYZ)$ = energy of the ejected Auger electron from element with atomic number Z

$E^Z(X)$ = binding energy of the level on which initial core hole is created

$E^Z(Y)$ = energy of level from which an electron falls to fill the initial hole

$E^Z(V')$ = energy appropriate to an atom already singly ionized in an inner shell.

In this formula E(Y) and E(V') can be approximated as the binding energy of the Y and V' levels respectively.

In Auger Electron Spectroscopy, the intensity of the emitted electron signal is measured as a function of the kinetic energy of electrons. High resolution spectra are usually obtained by using a cylindrical mirror analyzer (CMA). Auger spectra are always reported in the first derivative mode, by using the lock-in amplification technique [96]. Differentiation of the recorded signal is done electronically by applying a modulation voltage on the incident electron beam and recording the "in-phase" component of the ejected electron beam. In the first derivative spectrum, the auger spectra appear much pronounced, and the background of inelastically scattered electrons is significantly reduced.

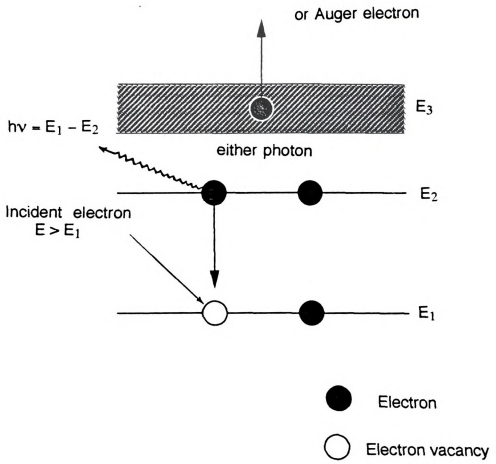

Fig. 25. A schematic diagram illustrating the basic processes associated with Auger electron transition.

The surface chemistry and interface between 1-2-3 matrix and Ag fibers in a HIPed specimen, containing 5 volume % Ag fibers, were studied. Samples were prepared by two different ways, one by fracturing and the other by polishing. One of HIPed specimens with 5 volume % Ag fibers was fractured at 77 K, liquid nitrogen boiling temperature. The other specimen with 5 volume % Ag fibers was metallographically polished by using 1 - 2 μm alumina powder and 0.2 - 0.5 μm diamond paste. Methanol was used to prevent possible degradation of the superconductor sample by moisture. Either fractured or polished specimens were introduced into the Auger chamber which was controlled at ultra-high vacuum conditions (1.5 x.10^{-9} torr). The SEM was used to examine the surfaces of both specimens. Fig. 26 shows a fracture surface taken by SEM. Auger surface scanning was performed on both specimens at 10 keV electron energy and 50 nA beam current. For these conditions the beam diameter was approximately 50,000 nm. For qualitative analysis, data was acquired in N(E) mode (number of counts per energy interval) vs. kinetic energy and then peaks were recorded in the derivative mode (N(E) * E). However, Auger characterization does not give the exact answer for the quantitative analysis, overall element concentration could be roughly estimated in terms of relative intensity.

In order to remove any residual surface contamination, ion sputtering was carried out on the fractured and polished specimens with a 4 keV Ar^+ ion beam and a 1 mm^2 raster size (the sputtering area). Sample preparation introduced a large amount of carbon, especially in the polished specimen due to methanol. The sputtered depth, calibrated by SiO_2, was 5,000 nm/min and the controlled system pressure was 15 x 10^{-3} Pa.

Electron line scanning was carried out to study the chemical distribution of elements, the diffusion of Ag into matrix and the diffusion of O_2 into Ag fibers

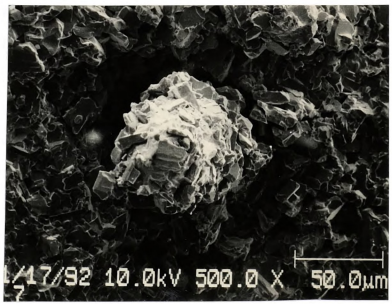

Fig. 26. A fracture surface examined by Auger spectroscopy apparatus (x 500).

at the interface. Line scanning was performed on the ion sputtered fractured sample (Fig. 26) after electronically drawing the horizontal scanning line across the fractured surface. This line was focused on the interface between the Ag fiber and the matrix. The applied electron excitation voltage was 10 keV and the beam current was 50 nA. Data points of line scanning on the SEM micrograph were taken at 2 μm intervals and different element concentrations were measured as a function of scanning distance (in μm). Estimated spatial resolution during line scanning is approximately 50,000 nm. Typical main Auger peaks of each element (kinetic energy) [97] are summarized at Table 3.

Compositional dot mapping for the distribution of chemical elements was performed on the ion sputtered fracture surface (Fig. 26). The applied electron excitation voltage was 10 keV and the beam current was 50 nA. Five different elements, Y, Ba, Cu, O and Ag are represented in terms of different contrasts in dot mapped pictures. In this experiment, Auger electrons of each element were detected around 200 to 500 nm from the surface.

Table 3

Typical main auger peaks in $YBa_2Cu_3O_{7-x}$ composite [97]

Elements	Kinetic energy (keV)
Y	127, 1746, 1821
Ba	500, 584, 600
Cu	840, 849, 920
O	468, 483, 503,
Ag	351, 356
C	272
B	179

4. RESULTS AND DISCUSSION

4. 1 Crystal Structure versus Processing Conditions

Figure 27 represents typical diffraction patterns of HIPed and unreinforced as well as reinforced specimens with different Ag volume %. The diffraction patterns shown in Fig. 27, are very similar to each other except for the extra peaks of Ag in the reinforced specimens and some variations in the relative intensity of prominent reflections. Relative intensity variations in prominent reflections might be associated with the localized texture formation during the HIPing process [98]. To confirm the peak positions, x-ray diffraction peaks from conventionally sintered 15 volume % Ag reinforced samples were compared with the major peaks of pure Ag and $YBa_2Cu_3O_{7-x}$ phases. The $YBa_2Cu_3O_{7-x}$ x-ray data was taken from Cava et al. [7] and pure Ag data was taken from powder diffraction index file (Fig. 28). From peak comparison, the diffraction pattern of the sintered 15 volume % Ag reinforced specimen, consisted of a superposition of diffraction patterns of pure Ag and orthorhombic $YBa_2Cu_3O_{7-x}$ phases.

Figure 29 shows the diffraction patterns of the 15 volume % Ag reinforced specimen, processed at different conditions: Fig. 29(a) sintered, Fig. 29(b) HIPed without post-annealing and Fig. 29(c) HIPed after annealing at 850°C for 20 hours. In this x-ray data, all of the diffraction peaks could be indexed. Comparing a conventionally processed sample in Fig. 29(a) with a HIPed sample Fig. 29(b) or HIPed sample after annealing Fig. 29(c) it is seen that the diffraction patterns for the HIPed samples have additional peaks at a 2θ value of 29, 30 (or 31) and 36.5 degrees. Composition and structure analysis [99] show that the phases responsible for these 2θ values are Y_2BaCuO_5 and Cu_2O which are the secondary phases, resulting from the phase decomposition of

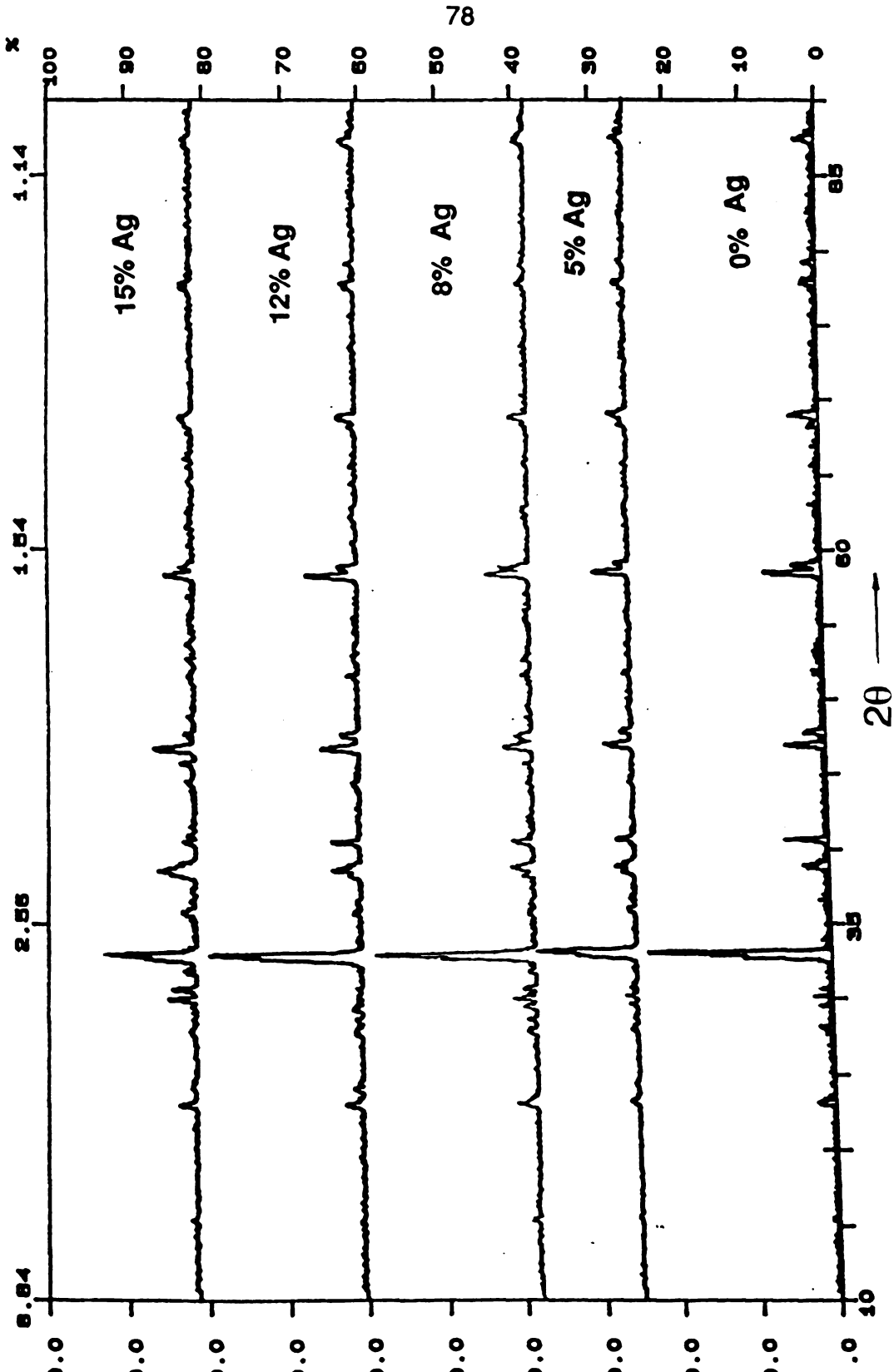

Fig. 27. Typical x-ray diffraction patterns from HIPed specimens.

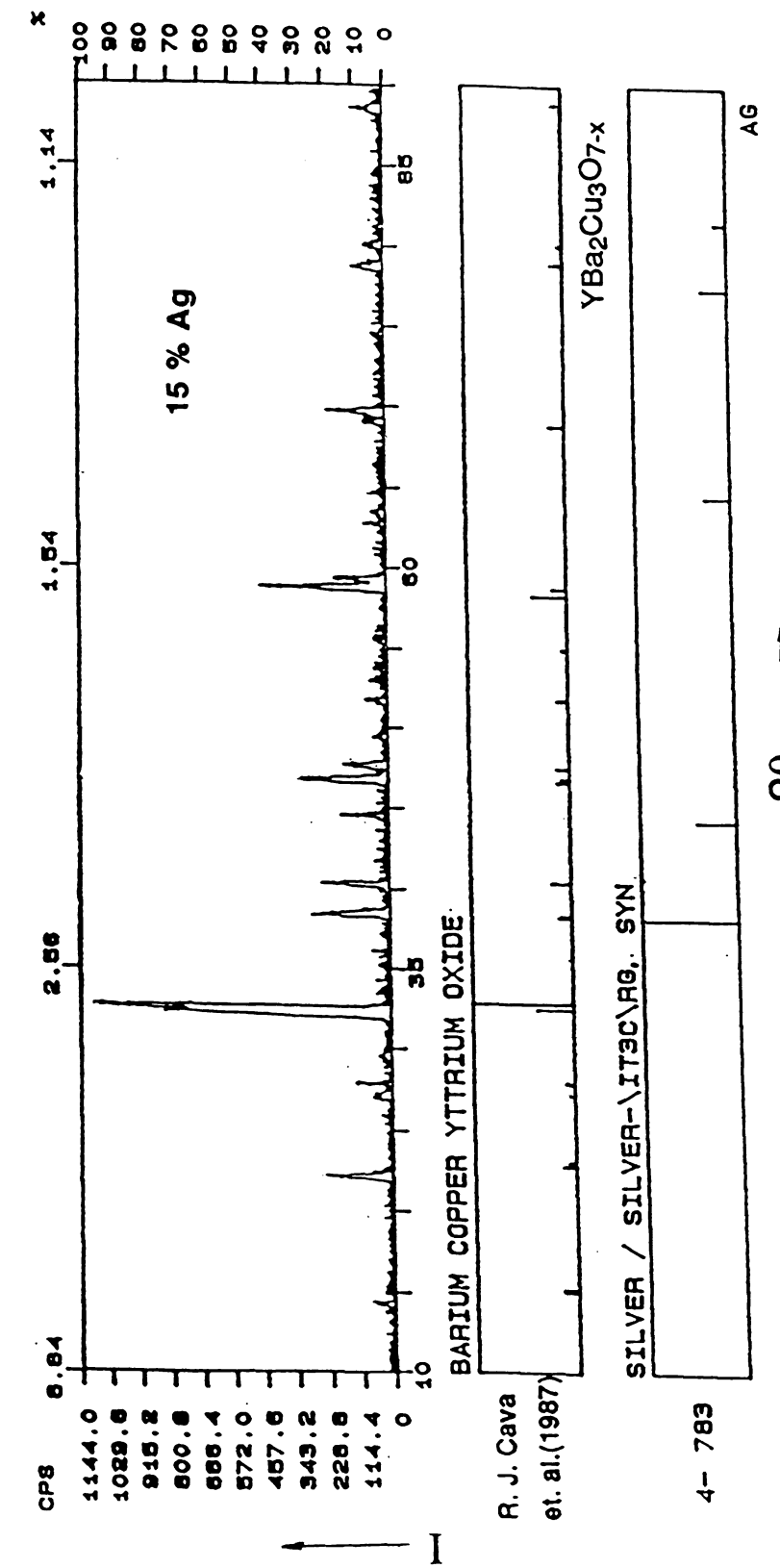

Fig. 28. X-ray diffraction pattern from a specimen reinforced with 15 volume % Ag. Reference diffraction pattern line positions of pure Ag and pure 1-2-3 compound are shown for comparison.

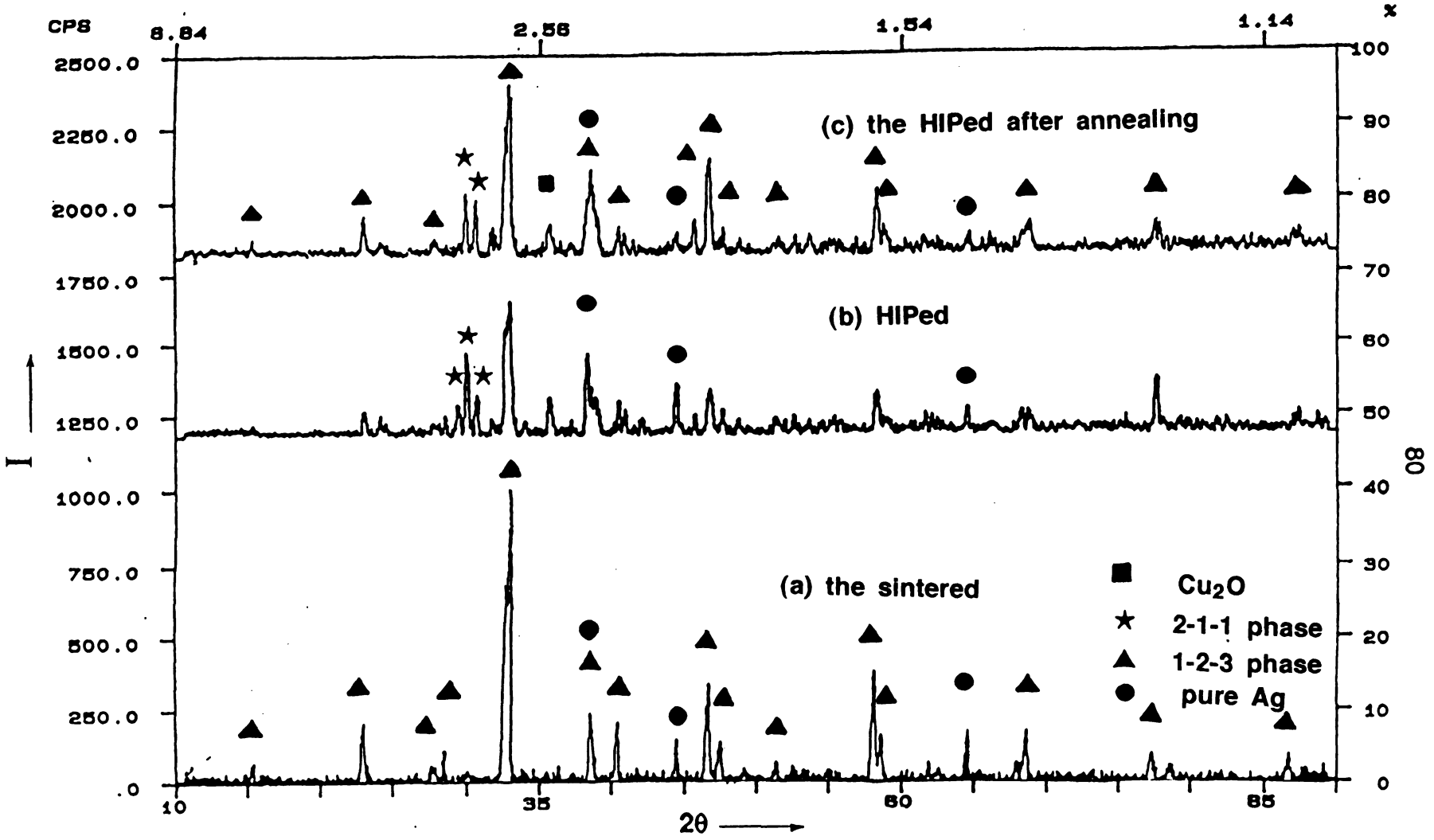

Fig. 29. X-ray diffraction patterns from specimens reinforced with 15 volume % Ag; for different processing conditions.

$YBa_2Cu_3O_{7-x}$. According to Wong et al. [99], Y_2BaCuO_5, called the "green phase", has orthorhombic perovskite type structure with lattice parameters of a = 71.31 nm, b = 56.59 nm and c = 116.80 nm. Therefore, the diffraction patterns observed after HIPing (Fig. 29) indicates the existence of a multiphase mixture: superconducting orthorhombic $YBa_2Cu_3O_{7-x}$ phase with some additional peaks of pure Ag and secondary peaks of Y_2BaCuO_5. However, relative intensities indicate the major phase is the superconducting orthorhombic $YBa_2Cu_3O_{7-x}$ phase. Fig. 29 also suggests that the silver remains intact with the 1-2-3 and other phases present. Another feature seen in Fig. 29 is the relative intensity decrease after HIPing. The decrease in relative peak intensities is related to the change of atom positions within the unit cell. Based on this observation, the relative intensity variations after HIPing are presumably related to oxygen stoichiometry changes in $YBa_2Cu_3O_{7-x}$ system.

Based on x-ray data (Fig. 29), conventionally prepared 1-2-3 after HIPing was found to be quite unstable and decomposed into other phases at the temperature of 890°C under 170 MPa. This phase decomposition is possibly associated with high pressure at the high temperature. The stress that causes this decomposition in the presintered sample is presumably the stress at the inter-particle contacts. The exact stress state at the inter-particle contacts varies throughout the sample. The load applied to the sample is distributed over the many inter-particle contacts, and the stress at each contact is a function of this contact load and the contact area. Since the total inter-particle contact area is less than the actual surface area of the sample, the average interparticle stress is always greater than the applied stress. For the case of isostatic pressure, the average inter-particle contact pressure, P_a, can be calculated as a function of density [75], as follows:

$$P_a = 4\pi P_{HIP} R^2/aND \qquad (24)$$

for monosized powders, where P_{HIP} is the isostatic pressure, R is the average powder particle radius, a is the average inter-particle contact area, N is the co-ordination number of the particle and D is density.

From equation 25, the contact stress decreases rapidly as density increases because the average inter-particle contact area increases as particles deform around each other. Possible decomposition reactions due to stress effect are:

$$YBa_2Cu_3O_{7-x} \rightarrow 1/2Y_2BaCuO_5 + ACuO + BCu_2O + CBaCuO_2 + DM_XO_Y \qquad (25)$$

$$\text{or } 2YBa_2Cu_3O_{7-x} \longrightarrow Y_2BaCuO_5 + 5CuO + 3BaO + yO_2 \qquad (26)$$

A recent x-ray study showed that the 211 phase (Y_2BaCuO_5) can be easily detected after HIPing. It is known that a small amount of 211 phase is always present even after careful preparation of 1-2-3 samples [100]. However, this 211 phase is quite commonly precipitated during a melt texturing process [63-65]. Based on equations 25 and 26, other second phase particles, such as CuO, or Cu_2O and $BaCuO_2$, should be detected in an x-ray measurement. However, the peaks related to those above mentioned phases were not strongly detected. This is possibly due to the small amounts of these phases present in the mixture.

The three diffraction patterns for 1-2-3 samples processed at different conditions, are shown in Fig. 30. The bottom scan, Fig. 30(a), shows the diffraction pattern for a sample presintered at 925°C for 2 hours and the center one, Fig. 30(b), shows a scan for a sample HIPed without any post-annealing. The

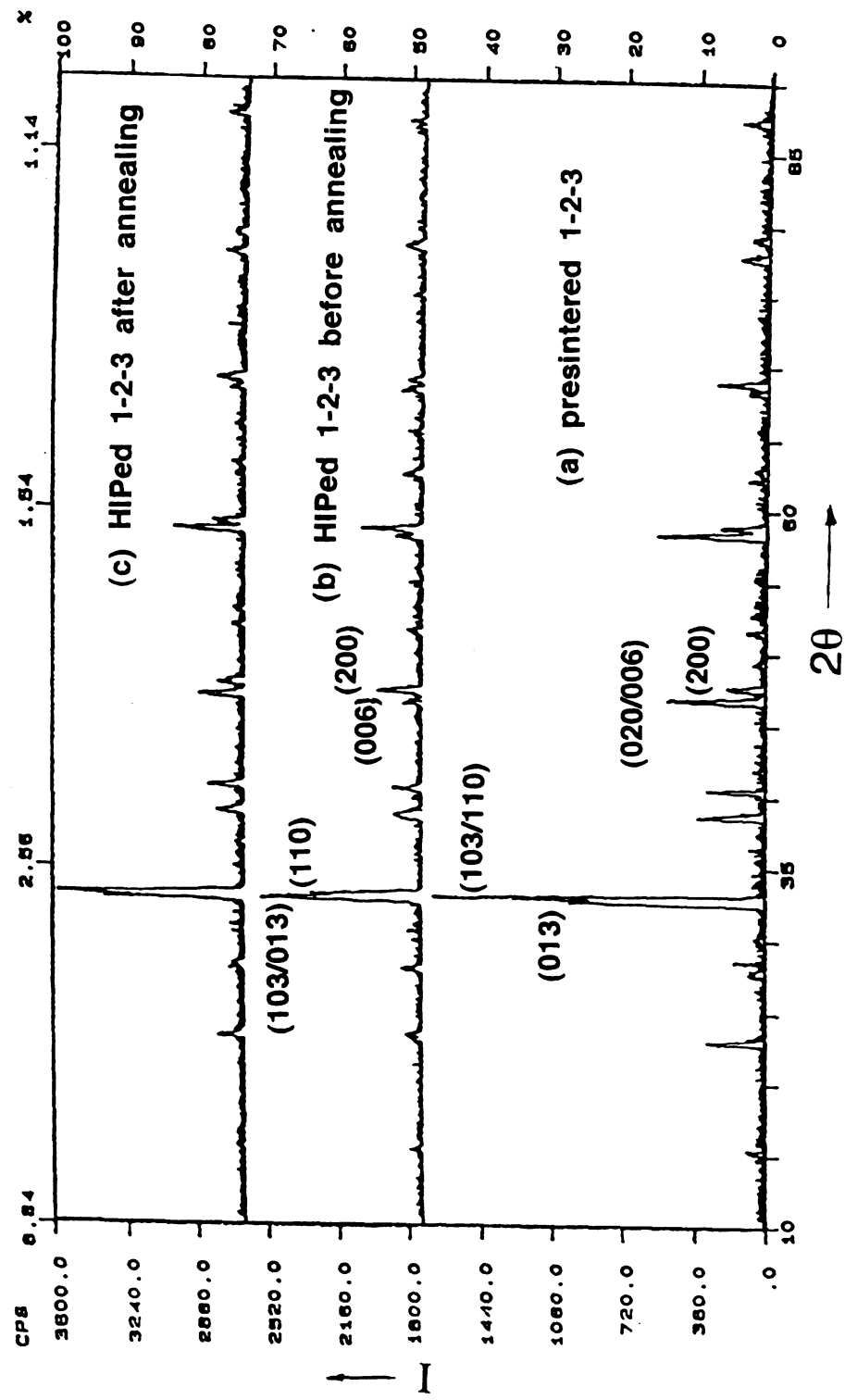

Fig. 30. X-ray diffraction patterns of 1-2-3 specimens for different processing conditions.

top scan, Fig. 30(c), shows a diffraction pattern for a HIPed sample after annealing at 850°C for 20 hours. Comparing Figs. 30(a) and 30(c) to Fig. 30(b), an important difference was found. The intensities of three pairs of diffraction peaks at around 32.5 and 32.8; 46.7 and 46.8; 58.2 and 58.3 degrees (2θ) are reversed in Fig. 30(b) compared with Figs. 30(a) and 30(c). Based on the structure analysis by Cava el al. [14], diffraction patterns shown in Figs. 30(a) and 30(c) were identified as those from an orthorhombic structure while that shown in Fig 30(b), is from a tetragonal structure.

In an orthorhombic phase, the peaks at 32.5 and 32.8 degrees, are indexed as 013 and 103/110 reflections respectively and these are indexed as 103/013 and 110 respectively in the tetragonal phase. In the orthorhombic phase, the intensity of the first peak (013) is lower than that of the 103/110 peak, but in the tetragonal phase, 013 and 103 reflections merge and give a higher intensity. Also the peaks at 46.7 and 46.8 degrees correspond to crystal planes 020/006 and 200 in the orthorhombic phase and the 006 and 200 in the tetragonal phase respectively. Based on these x-ray analysis, the x-ray results shown in Fig. 29 and Fig. 30, support the existence of a phase transformation under pressure, suggested by other researchers [73, 101]. Hendrix et al. [73] pointed out the $YBa_2Cu_3O_{7-x}$ compound was unstable with respect to pressure and it decomposes into other metal oxides (Y_2BaCuO_5, $BaCuO_2$, CuO and others) at stresses greater than 100 MPa, and at temperatures ranging from 700 to 950°C. According to Dijken et al. [102], during HIP densification at 900°C, sintered $YBa_2Cu_3O_{7-x}$ strongly degasses and the oxygen partial pressure increases up to 24.8 MPa. This means that the transformation and decomposition reaction processes of the $YBa_2Cu_3O_{7-x}$ compound prevent full densification and possibly cause the glass capsule material to blow out.

Therefore, it can be concluded from Fig. 29 and Fig. 30 that HIPing of the

$YBa_2Cu_3O_{7-x}$ compound produces unstable conditions and leads to the loss of oxygen and a transformation from the high T_c orthorhombic phase to the non-superconducting tetragonal phase. This result can be explained in terms of stoichiometry of $YBa_2Cu_3O_{7-x}$ compound which has the highest T_c orthorhombic phase for x close to 7.0. When it is heated, the high T_c orthorhombic phase decomposes first to a low T_c superconductor for x below about 6.7 to 6.8, and finally to a non-superconducting tetragonal phase for x below about 6.4.

4. 2 Superconducting Properties

4. 2. 1 Critical temperature (T_c) measurements

Figure 31 shows the temperature dependance of the electrical resistance of 1-2-3 system with Ag reinforcement, ranging from zero to 15 volume % Ag. The variation of the resistance with temperature of HIPed 1-2-3 composites was similar to those observed for the sintered samples. This means the resistance decreased approximately linearly with decreasing temperature to just above the superconducting onset temperature, and then sharply dropped at the transition temperature. The onset temperature, in resistance, is defined by the smallest curvature of the resistance-temperature curve [103]. HIPed samples with different volume % Ag have onset temperatures ranging from 90 to 92 K and have zero resistance at temperatures between 88 and 90 K. The transition width, which is defined as the temperature range for 10 - 90 % of transition, is 2 - 4 K.

Based on x-ray results shown in Fig. 29 and Fig. 30, HIPed samples, with Ag fiber, consisted of a multiphase mixture; superconducting orthorhombic $YBa_2Cu_3O_{7-x}$ phase, pure Ag and secondary phases of Y_2BaCuO_5. Therefore, it can be concluded that as long as the superconducting phase is fully

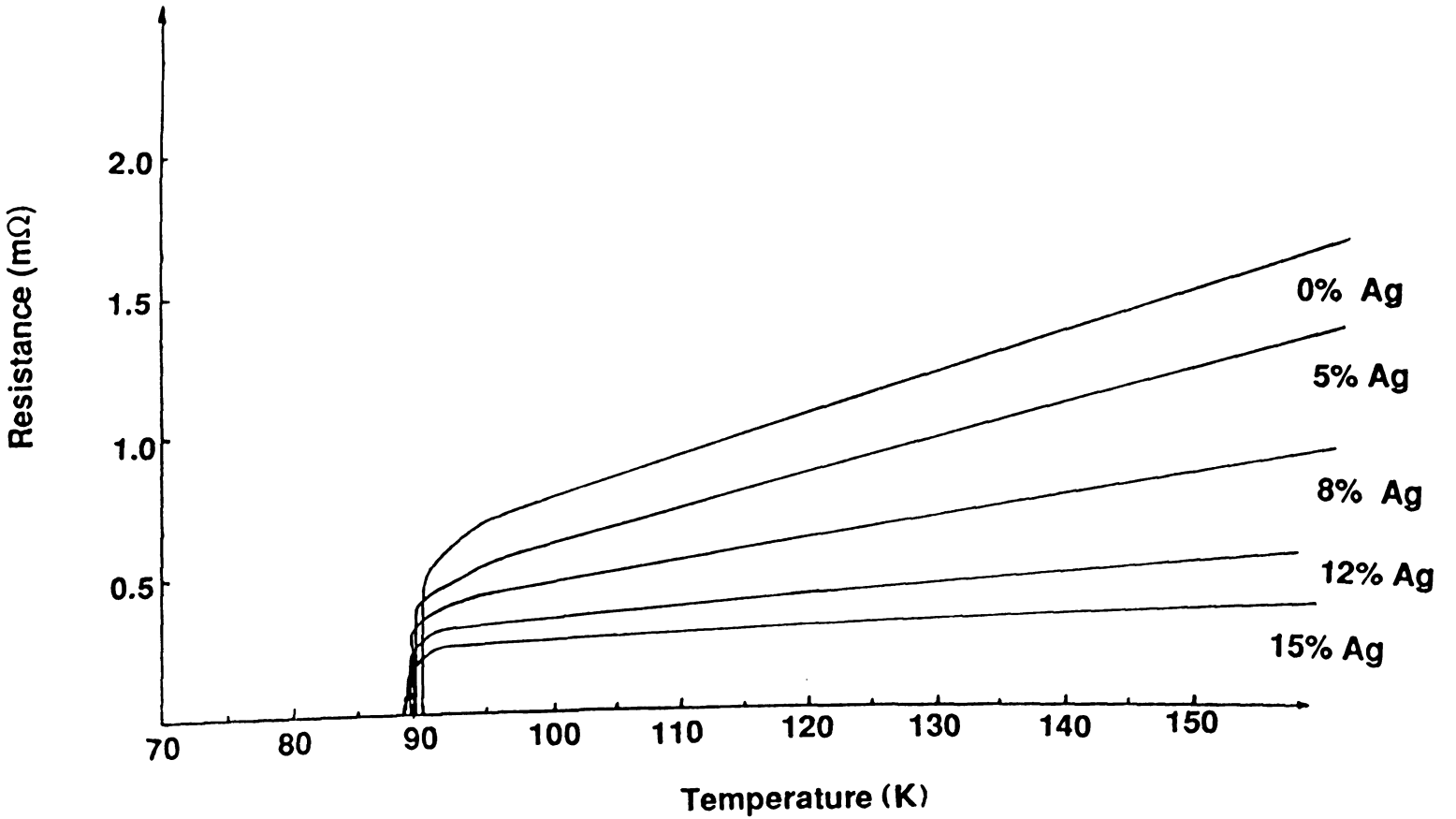

Fig. 31. The temperature dependance of resistance of 1-2-3 compound with different amounts of reinforcing Ag fibers.

interconnected, the presence of second phases, such as Y_2BaCuO_5 and other impurity phases ($BaCuO_2$, CuO , etc.), have little effect on the sharpness of the superconducting transition. It is to be noted that an improperly controlled oxygen stoichiometry, on the other hand, has a much stronger effect on the transition temperature width.

As seen in Fig. 31, an unreinforced HIPed specimen shows a relatively sharp transition behavior and the highest T_c value compared with the reinforced samples. This phenomenon suggests that better interconnectivity between high T_c grains can be obtained in the absence of Ag fibers in the specimen. Also the HIPed samples with 15 volume % Ag, display a larger transition temperature width. This broad transition may be indicative of the presence of weak link boundaries or minority phases along grain boundaries. Since Ag fibers are susceptible to oxidation, fiber oxidation may alter the desired oxygen stoichiometry of the superconducting phase near the Ag fiber. Therefore, Ag fibers might cause the formation of a low T_c phase or even a non-superconducting tetragonal phase near the fiber-matrix interface.

Figure 31 also demonstrates that the slope of the resistance vs. temperature curves, in the normal state, decreases systematically as the volume % Ag fibers increases. Also resistance at the non-superconducting state, decreases with increasing volume % Ag fibers. However, the transition temperature is approximately the same. Room temperature resistance of a sample with 15 volume % Ag, was found to be 0.3 mΩ. In contrast, the resistance of an unreinforced sample with the same geometry and at the same temperature, was 2.9 mΩ; a resistance almost 10 times higher than that of the 15 % reinforced specimen. Fig. 32 shows a plot of the normal state resistance at 150 K for samples with different volume % Ag fibers. This is a derived plot from Fig. 31. As can be seen in Fig. 32, resistance decreases linearly with the increase in volume % Ag.

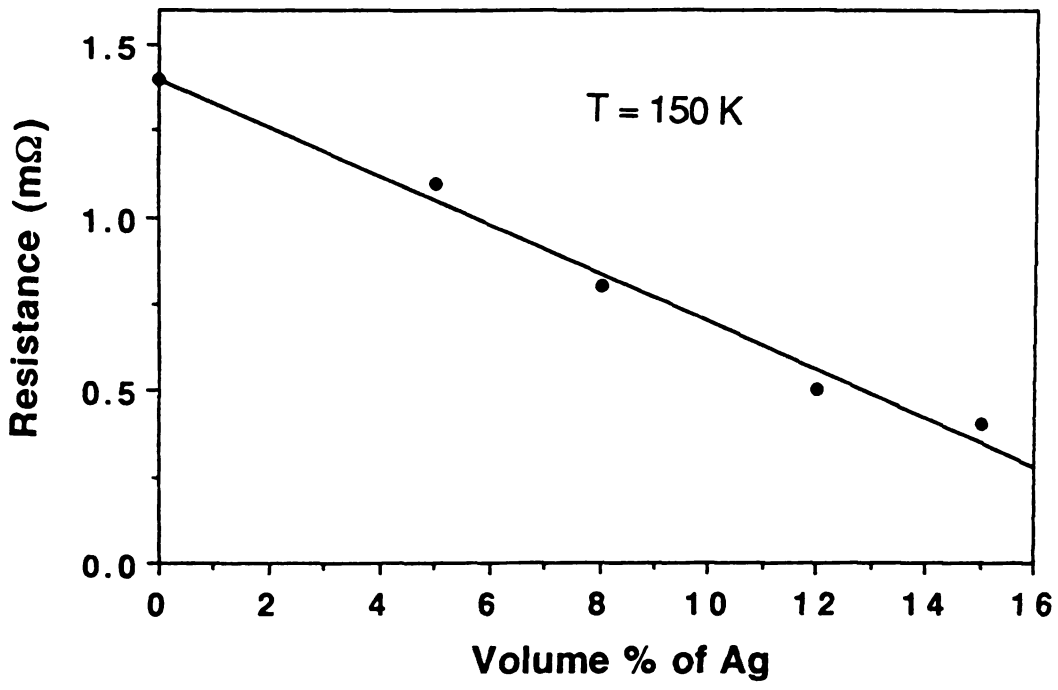

Fig. 32. The electrical resistance of specimens, with different volume % Ag fibers, at 150 K.

This can be accounted for by the Ag fiber, having a lower resistance than that of the ceramic 1-2-3 matrix.

Resistivity measurements for 1-2-3 samples, processed at two different conditions, one by conventional sintering and the other by HIPing (after post-annealing at 850°C for 20 hours) are shown in Fig. 33. This figure shows that a HIPed sample after post-annealing, has a lower T_c as well as its normal state resistivity is lower than that of a presintered 1-2-3 specimen. A HIPed sample without a post-anneal was found to consist of the non-superconducting tetragonal crystalline structure as determined from x-ray analysis (Fig. 30(b)). However, after post-annealing the oxygen stoichiometry is restored, possibly creating a greater degree of order of oxygen in the Cu-O chain.

4. 2. 2 Critical current density (J_c) measurements

The voltage-current (V-I) curves for samples with different volume % Ag, are shown in Fig. 34. Table 4 shows summarized data for critical current density (J_c) and the critical temperature. The results for J_c shown in Table 4 have a greater degree of uncertainty due to the resolution of the measuring instruments. The voltage drop across the specimen was measured in mV scale rather than in μV scale. Though the results shown in Table 4 are less accurate, the data for J_c, measured from HIPed specimens are reproducible enough to make qualitative comparisons.

J_c values shown in Table 4 demonstrate that the current density for HIPed specimens with 15 vol. % Ag is approximately 4 times higher than that for the conventionally sintered specimens with no Ag. The observed increase in J_c with increasing Ag volume %, is difficult to explain. It is possible that the Ag fiber acts as an agent which assists the formation of a denser 1-2-3 network. It

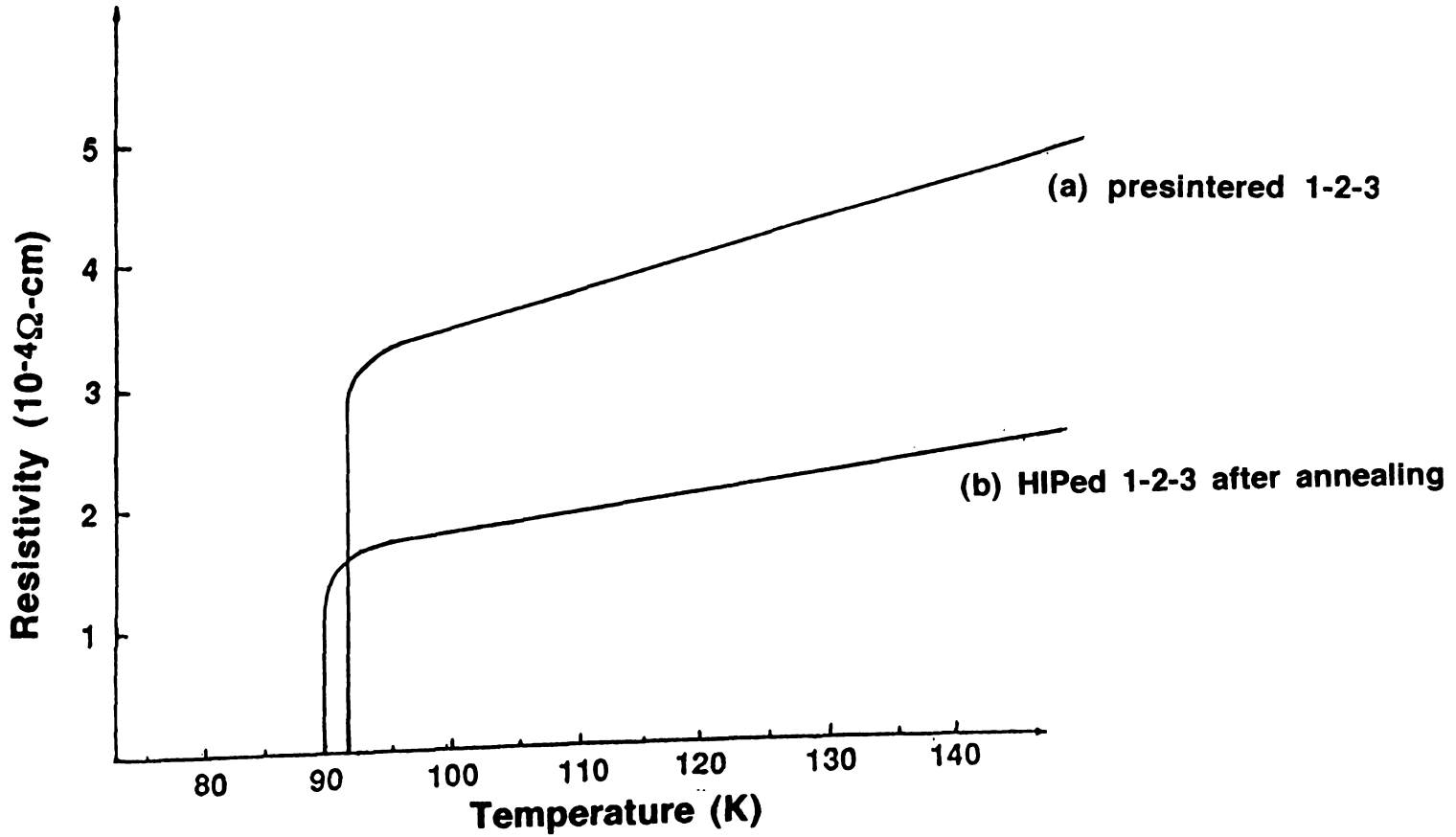

Fig. 33. Resistivity vs. temperature curves for 1-2-3 specimens processed by two different conditions; a presintered sample, and a sample HIPed and annealed.

Table 4

Results of transition temperature and critical current density measurements for HIPed and sintered $YBa_2Cu_3O_{7-x}$

	T_c (HIPed)	J_c (Sintered)	J_c (HIPed)
0%	90.0 ± 1.5	55 ± 5	110 ± 10
5%	89.0 ± 2.0	75 ± 5	126 ± 15
8%	88.5 ± 2.0	70 ± 8	145 ± 15
12%	88.5 ± 2.0	80 ± 10	200 ± 15
15%	88.0 ± 2.0	95 ± 15	205 ± 15

.Unit of T_c : K,
.Unit of J_c : Amp/cm^2

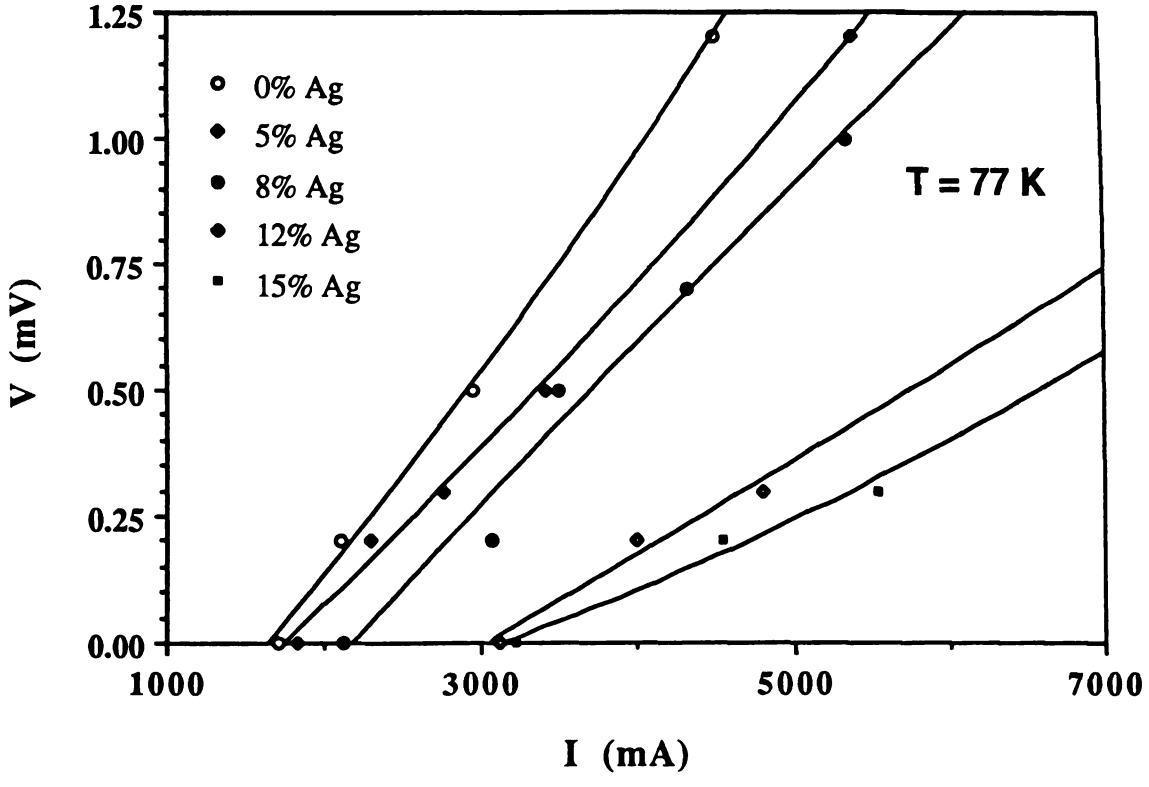

Fig. 34. The voltage-current (V-I) curves for specimens with different volume % Ag fibers.

is also possible that an oxygen interaction at the Ag-matrix interface might precipitate non-superconducting phase (as discussed earlier) while producing flux pinning.

One of the results obtained from the J_c measurements is the voltage-current (V-I) graphs for samples with different volume % Ag fibers. Beyond some critical current, a phase transformation from a superconducting to a non-superconducting state occurs. On the non-superconducting state, ohms law ($V = IR$) is effective in terms of the electrical voltage and electrical current. Therefore, the slope of V-I curve as a function of volume % Ag indicates trend of resistance of the non-superconducting state with the variation Ag content. For the unreinforced samples in the non-superconducting state, the slope of V-I curve is steep, that is, the resistance is high. As the Ag volume % increases, the slope of the V-I curve decreases since in normal state the resistance of the Ag reinforced composite decreases. Fig. 35 shows the slopes of the voltage-current (V-I) curves plotted as a function of volume % Ag. We note that within experimental errors, the slopes of the two curves shown in Figures 32 and 35 respectively are the same. The only difference is that the absolute value of the resistance as measured directly, is larger than that derived from Fig. 35. It can be speculated that the directly measured resistance sees a greater contribution from contact resistance. Also the resistance values in Fig. 35 correspond to the electrical resistance at 77 K as compared with that in Fig. 32 which is at 150 K.

The effect of a 211 phase on J_c was studied by McCallum et al. [100]. They pointed out the presence of the 211 phase may actually improve properties by producing flux pinning sites if they are distributed properly. However, in this experiment, the amount of 211 phase was very small and the determination of the presence of the 211 phase was quite difficult.

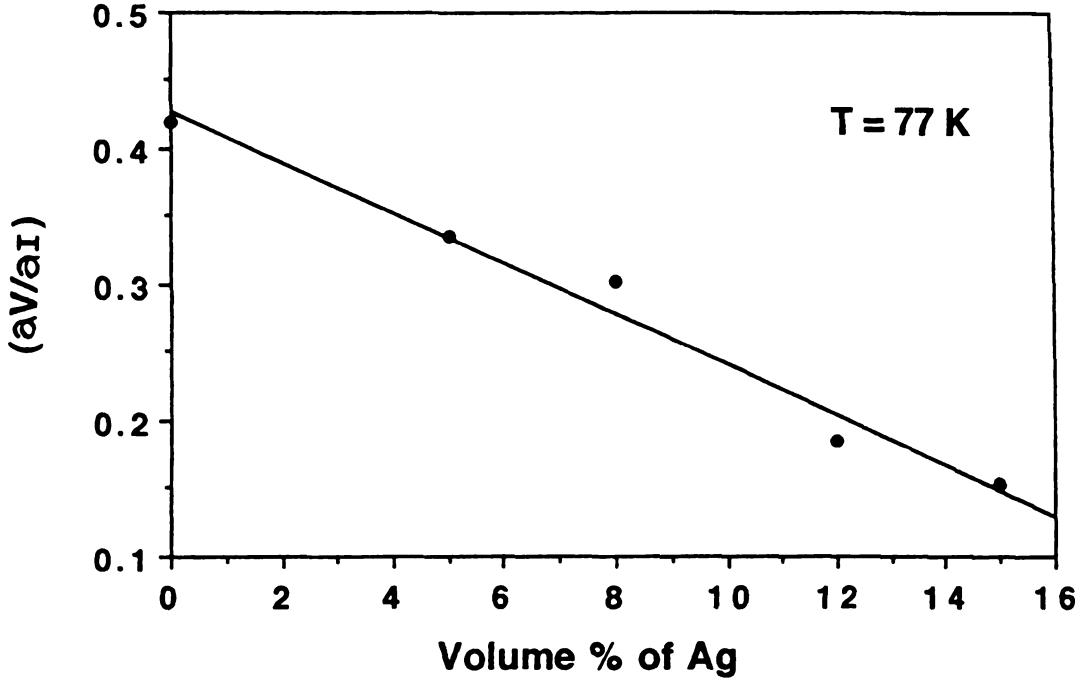

Fig. 35. The slopes of the voltage-current (V-I) curves in Fig. 34, are plotted as a function of volume % Ag fibers.

4. 2. 3 D.C magnetic moment measurements

The temperature dependance of the D.C magnetization for HIPed specimens with different volume % Ag is shown in Fig. 36. As can be seen in this figure, the magnetic moment is systematically changed with increasing temperature. There is a strong tendency toward a diamagnetic behavior which becomes systematically less dominant when the transition width broadens with increasing the volume % Ag fibers. HIPed samples with 15 volume % Ag displayed a wider transition temperature region and a lesser diamagnetic behavior compared to other samples. The decrease of diamagnetic behavior and the broadening of the transition width, with increasing volume % Ag, presumably arise from the decrease of the volume fraction of the superconducting phase in the HIPed specimen with increasing volume % Ag.

The magnitude of the Meissner effect is proportional to the volume fraction of the superconducting phase in the specimen. If the sample has a large amount of superconducting phase, the Meissner effect will be strong. Electrical resistivity on the other hand dependents on both the amount of the superconducting phase present, as well as the grain boundary properties. Even if a specimen has a large volume fraction of the superconducting phase, it does not show a sharp superconducting transition in the electrical resistivity, if its grain boundary is degraded. Conversely, if the specimen has a low volume % of the superconducting phase, it can show a sharp superconducting transition in the electrical resistivity if the superconducting phases are fully interconnected.

To determine the transition temperature from magnetic moment measurements, the transition area (10 - 90 % of the transition temperature), in the temperature range from 85 to 95 K, was enlarged. From this magnified area, the superconducting transition temperature was found to be approximately 88 ±

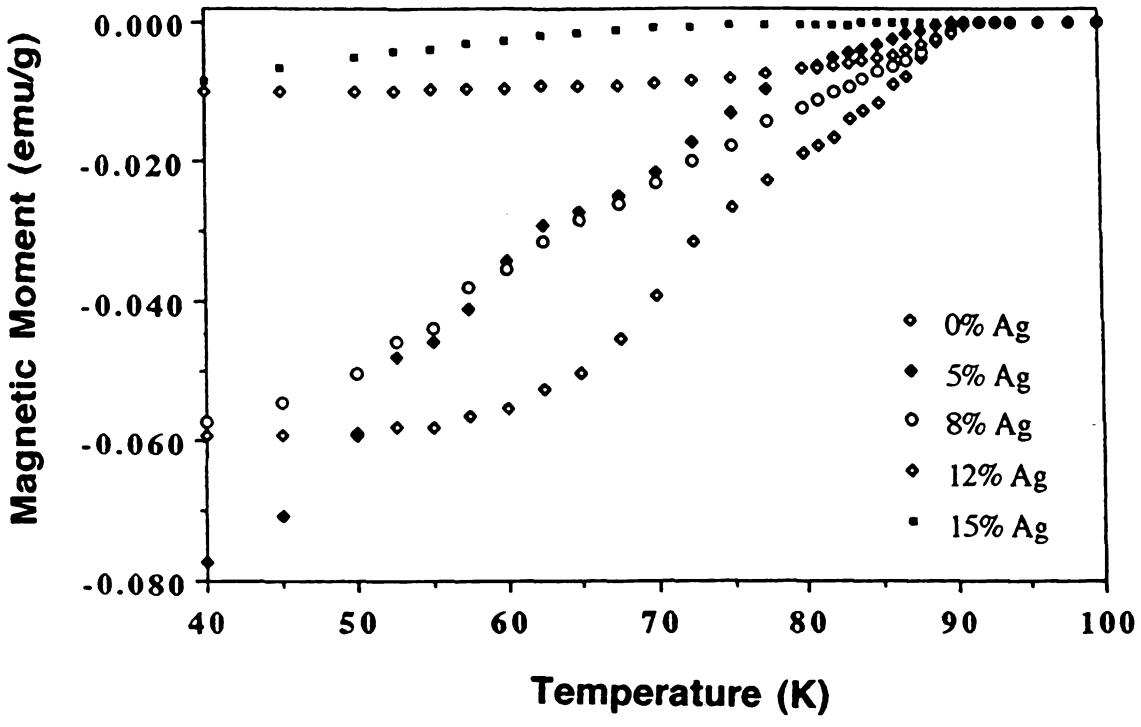

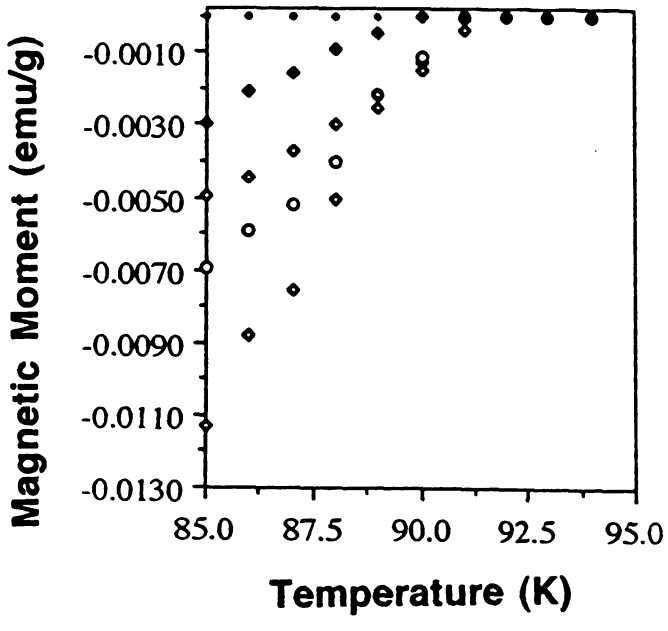

Fig. 36 The temperature dependance of the D.C magnetization for HIPed specimens.

3 K, which is consistent with the value obtained from the electrical resistance measurement carried out at various temperatures.

Based on the x-ray data, most Ag reinforced specimens have a lower volume fraction of the superconducting phase. Therefore, it can be concluded that the relatively sharp superconducting transition in electrical resistivity is due to the interconnected network of superconducting phases as mentioned earlier.

4. 3 Variation of Density and Porosity of Samples with Different Types of Processing

Porosity was measured as a function of the volume % Ag fibers and these results are plotted in Fig. 37. The porosity in the conventionally sintered specimens increased almost linearly with volume % Ag. However, HIPed samples were considerably more dense and did not show any increase of porosity with Ag volume %. After HIPing, the samples had densities between 92 and 96 % of the theoretical density.. Table 5 summarizes density and porosity data.

4. 4 Mechanical Properties of Ag-Fiber Reinforced Composites

Figure 38 shows the flexural strength of both HIPed and conventionally sintered specimens. Due to the optimization of the microstructure, the HIPed samples show significantly improved flexural strength over that of the conventionally sintered samples. The large amount of porosity (20 - 30 %) in the sintered specimens accounted for the low strength. Measured flexural strength of unreinforced 1-2-3 after HIPing and sintering, were found to be 56 MPa and 34 MPa respectively. However, as shown in Fig. 38, the flexural strength

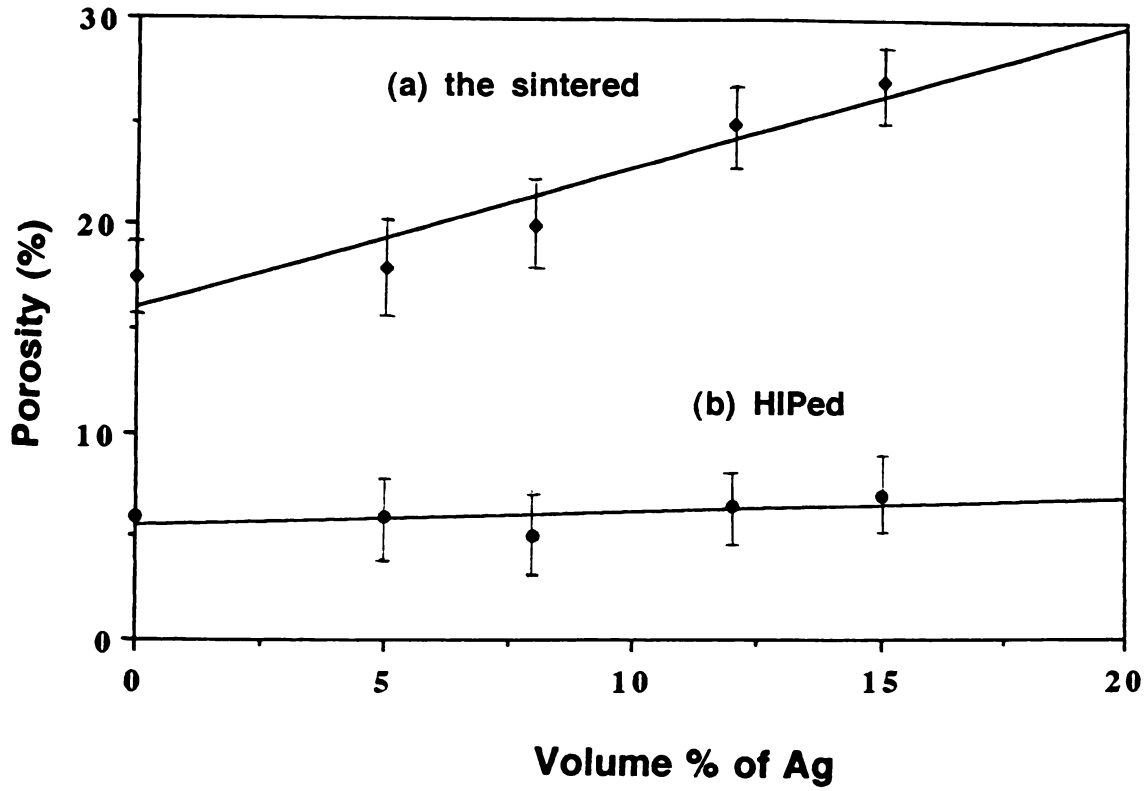

Fig. 37. Variation of porosity with volume % Ag fibers
(a) conventionally sintered samples; (b) HIPed samples.

Table 5

Measured and theoretical densities and porosities of $YBa_2Cu_3O_{7-x}$ reinforced with different volume % Ag-fibers

	Theoretical density (g/cm^3)	Measured density (g/cm^3) (a) sintered	(b) HIPed	Porosity (%) (a) sintered	(b)HIPed
0%	6.3750	5.2593 ± 0.1393	5.9925 ± 0.1015	17.5 ± 1.5	6.0 ± 1.6
5%	6.5808	5.3963 ± 0.1481	6.1860 ± 0.1130	18.0 ± 2.3	6.0 ± 1.7
8%	6.7043	5.3634 ± 0.1611	6.3691 ± 0.1208	20.0 ± 2.4	5.0 ± 1.8
12%	6.8689	5.1516 ± 0.1651	6.4224 ± 0.1215	25.0 ± 2.4	6.5 ± 1.8
15%	6.9924	5.1045 ± 0.1660	6.5029 ± 0.1253	27.0 ± 2.4	7.0 ± 1.8

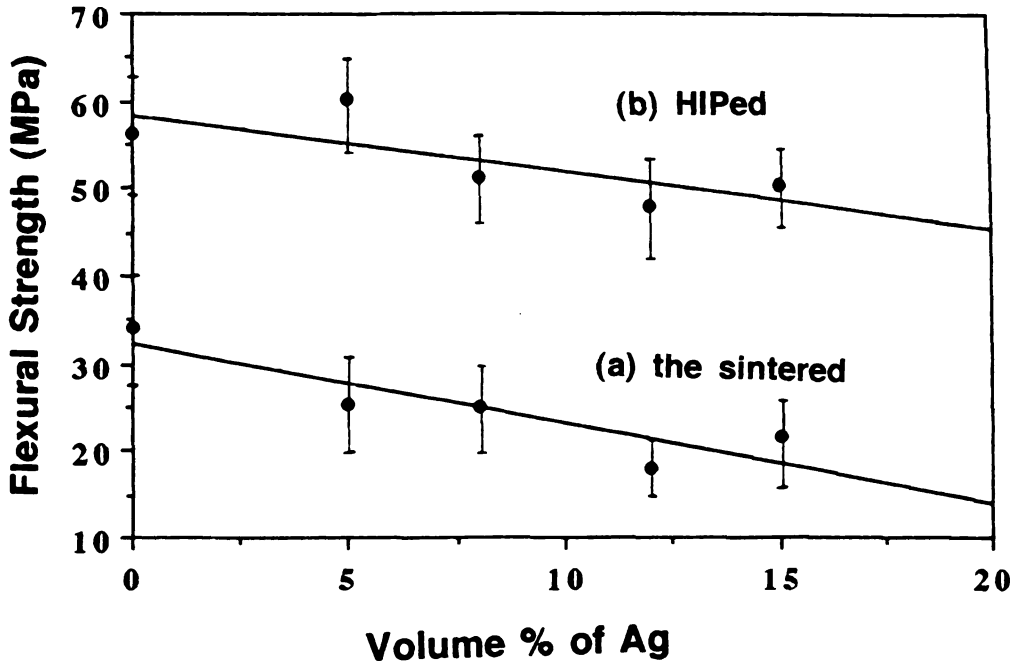

Fig. 38. A plot of flexural strength vs. volume % Ag
(a) conventionally sintered samples; (b) HIPed samples.

decreased systematically with increasing volume % Ag.

There are several possible explanations for flexural strength decrease with increasing volume % Ag:

(1) The general theory of the fiber reinforcement suggests that strengthening will occur if the elastic modulus of the fibers is greater than that of the matrix. The elastic modulii of Ag fiber and 1-2-3 matrix were found to be around 71 GPa [104] and 140 GPa [105] respectively.

(2) Inhomogeneous mixing of the fibers presumably causes nonuniform distribution of fibers in the fracture plane. This will also reduce the strengthening efficiency.

(3) If the interfacial bonding between the matrix and the fibers is weak then strength will decrease with increasing volume % Ag fiber.

(4) The diameter (50 μm) of Ag fibers might be relatively large. Fiber diameter influences strongly on the strength of the composite; usually the composite strength increases as fiber diameter decreases [106]. Also the large diameter fibers sometimes act as stress concentration sites which weaken the matrix.

(5) If the fiber length is shorter than the critical fiber length (l_c), then the matrix deforms around the fiber such that there is virtually no stress transfer and thereby the proportion of fibers capable of being loaded to the fracture stress will be reduced.

Another important property of fiber reinforced composites is their toughness. A useful way of quantifying toughness of a material is by measuring the fracture surface energy (γ) as has been discussed earlier. This is a measure of the resistance of the material to crack propagation and is defined empirically as the minimum amount of energy required to create a unit area of fracture surface. Increasing the fracture surface energy, by inhibiting crack propagation,

increases the resistance to fracture under static or shock loading.

K_{Ic} as a function of Ag volume fraction is shown in Fig. 39. As can be seen, K_{Ic} increases significantly with increasing volume % Ag. With 15 volume % Ag fibers, the measured K_{Ic} value increased up to 4.5 MPa $m^{1/2}$ which is almost 4 times higher than that for the unreinforced HIPed specimens (1.2 MPa $m^{1/2}$).

The nature of load-deflection curves as a function of Ag fiber volume fraction are also shown in Fig. 40. Typical fracture behavior of a 15 % Ag reinforced HIPed specimen along the load-deflection curve, is shown by inserting typical microstructures associated with the various stages of deformation. The increasing area under load-deflection curves in Fig. 40, indicates a remarkable improvement in the average value of fracture energy (γ). From these curves (Fig. 40), it is clear that the unreinforced 1-2-3 sample failed catastrophically, and simultaneously the fracture load decreased immediately to zero. This fracture behavior is typical of a brittle ceramic material. In contrast, as seen in the optical micrographs of the sample (Fig. 40), the reinforced specimen fractured in a very different way. The crack deviated from original fracture plane because of the bridging fibers and displayed additional displacement before the ultimate failure.

Different load-deflection curves can be explained by the type of energy absorption mechanisms. Some of these mechanisms may be fiber debonding, crack-deflecion, fiber pull-out and fiber plastic deformation. However, in this experiment, the energy of fracture is found to be due to a combination of the work needed to debond the fibers, and the work done against friction in pulling the fibers out of the matrix.

A summary of the mechanical property data obtained for samples reinforced with different volume fraction Ag fiber is shown in Table 6. Although

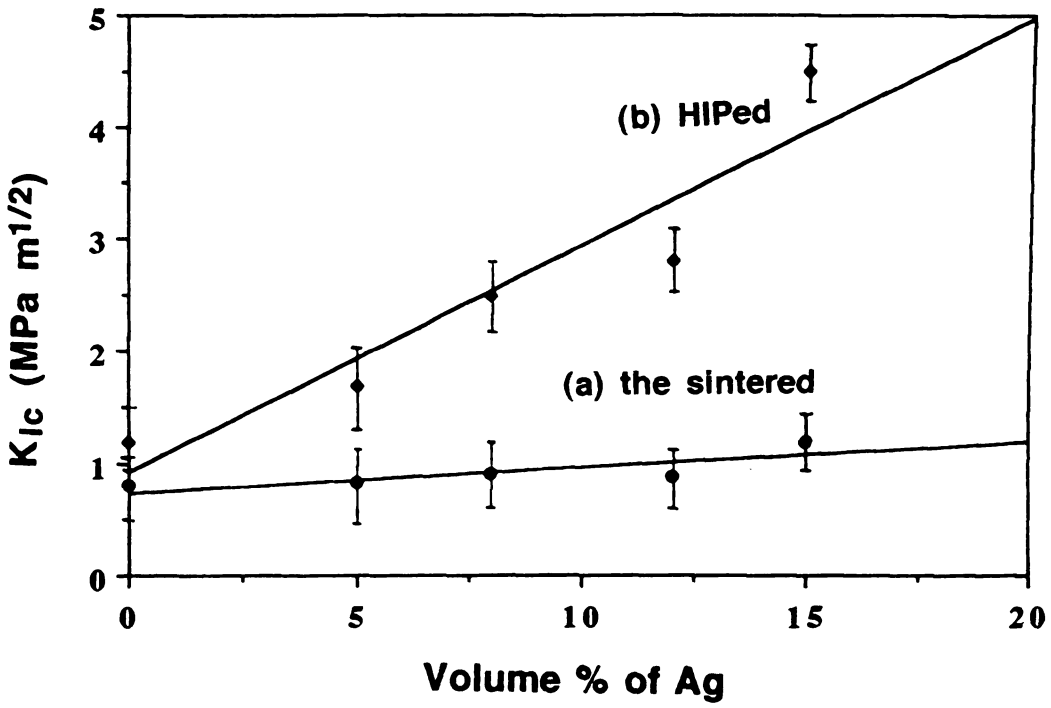

Fig. 39. K_{Ic} versus volume % Ag
(a) conventionally sintered samples; (b) HIPed samples.

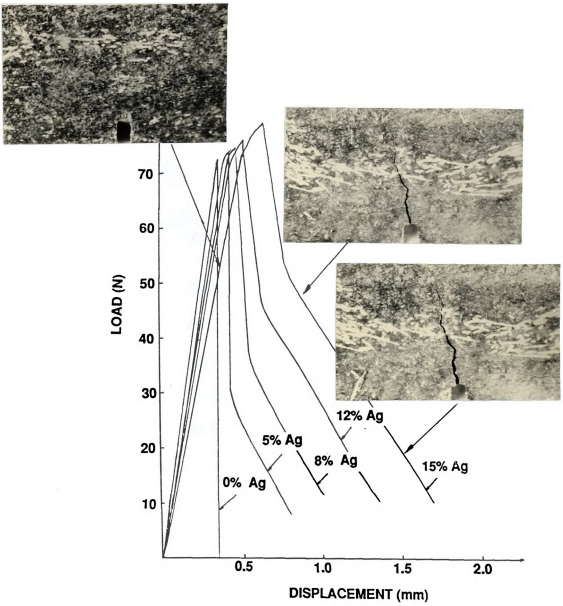

Fig. 40. Typical load-deflection curves of $YBa_2Cu_3O_{7-x}$ samples reinforced with various volume % Ag fibers. Also shown are corresponding typical fractographs.

Table 6

Summary of measured mechanical properties of 1-2-3 and Ag fiber reinforced and HIP consolidated 1-2-3 compound

	σ_F(MPa)		K_{Ic}(MPa $m^{1/2}$)	
	(a) sintered	(b) HIPed	(a) sintered	(b) HIPed
0 %	34.3 ± 6.0	56.2 ± 7.3	0.80 ± 0.3	1.2 ± 0.3
5 %	25.4 ± 5.5	60.3 ± 7.0	0.83 ± 0.4	1.7 ± 0.4
8 %	24.9 ± 5.2	51.3 ± 6.1	0.91 ± 0.3	2.5 ± 0.3
12 %	18.0 ± 6.3	47.9 ± 7.2	0.87 ± 0.3	2.8 ± 0.4
15 %	21.7 ± 6.2	50.4 ± 4.2	1.23 ± 0.3	4.5 ± 0.3

there is some scatter in the data, the results exhibit a significant improvement in K_{Ic} and fracture energy. Flexural strength values, however, are seen to decrease systematically as a function of volume % Ag.

4. 5 Microstructure and Interfaces

4. 5. 1 Optical microscope analysis

Figure 41 shows the microstructure of the as-received Ag fibers. For comparison, microstructures of the unreinforced and Ag fiber reinforced specimens, produced by two different processing techniques, are shown in Fig. 42 and Fig. 43 respectively.

The conventionally processed specimen shows extensive porosity and large grain size, while the HIP processed specimen have relatively less porosity and a very fine grain size (Figs. 42, 43(a) and 43(b)). Optical microscopy of a HIPed specimen (observed under polarized light) revealed a bimodal grain size; the smaller grains are 1 - 5 μm in diameter, and the larger grains are approximately 10 - 15 μm in diameter. The HIPed sample contained a small amount of uniformly distributed porosity. Examination of the microstructure of the HIPed sample indicates an improved inter-grain integrity resulting from the elimination of residual pores. As seen from Fig. 43, the Ag fibers bond well with the 1-2-3 phase by forming a continuous network. This continuous network is believed to be responsible for improved J_c as discussed earlier.

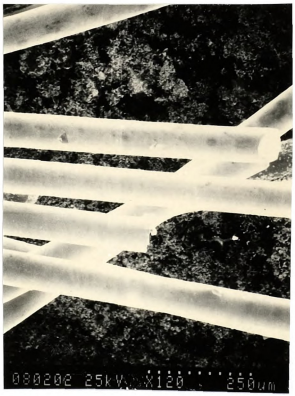

Fig. 41. Microstructure of as-received pure Ag fibers (x120).

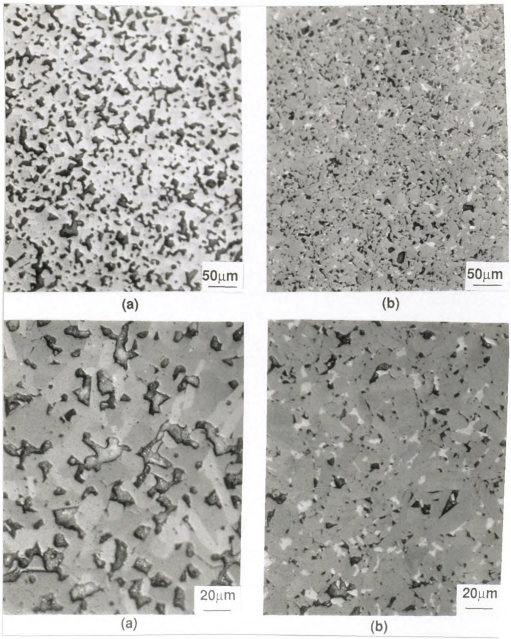

Fig. 42. Optical microstructures taken from the polished surface of 1-2-3 specimens at different magnifications (x 200 and x 500) (a) sintered, (b) HIPed and annealed.

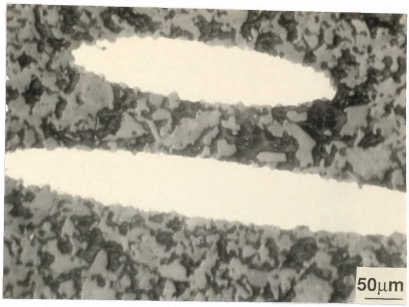

(a)

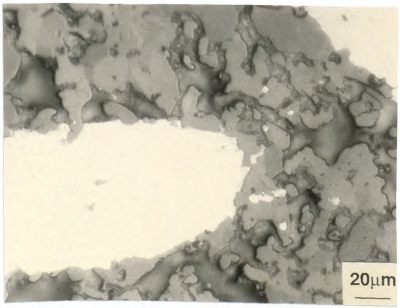

(b)

Fig. 43(a). Optical microstructures of the sintered specimen reinforced by 15 volume % Ag fiber, taken at different magnifications (a) x 200, (b) x 500.

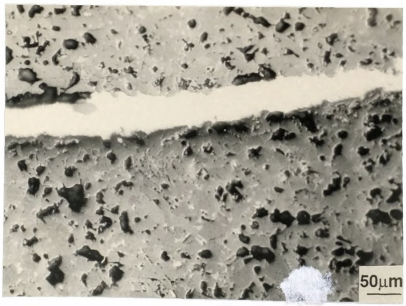

(a)

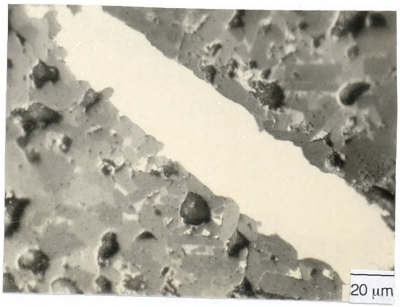

(b)

Fig. 43(b). Optical microstructure of HIPed specimen reinforced by 15 volume % Ag fiber, taken at different magnifications (a) x 200, (b) x 500.

4. 5. 2. Scanning Electron Microscopy (SEM) analysis

The SEM micrographs in Fig. 44 were taken on the fractured section of a conventionally sintered, and HIPed samples as shown in Fig. 44(a) and 44(b) respectively. As observed by using the optical microscope, the sintered specimen contains copious amounts of pores and the grain size is large. The HIPed specimen on the other hand shows fewer pores and the grain size is smaller. To confirm the presence of the homogeneous distribution of fibers in the matrix, fracture surfaces with increasing volume % Ag fiber were systematically studied using a SEM (Fig. 45). As can be seen in Fig. 45, the area fraction of Ag fiber increases with increasing percentage of Ag fibers added. These figures also indicate a relatively uniform distribution of fibers in the matrix.

Fracture surface observations give useful information concerning energy absorption or toughening mechanisms. Some of these mechanisms may be fiber debonding, crack-deflecion, fiber pull-out and fiber plastic deformation. As can be seen in Fig. 46(a), different aspects of fiber pull-out from the matrix can be clearly seen. Also debonding phenomena between the fiber and matrix are easily seen from Fig. 46(b).

One significant phenomena, observed in most micrographs, is that the topography of the Ag fibers are altered during HIP processing. As can be seen from Fig. 47, the surface of Ag fiber was visibly faceted by attached 1-2-3 grains. The faceted Ag fiber can not be fully explained by a typical ductile fracture behavior which usually occurs in Ag after neck formation. To determine surface microhardness, vickers indentation tests were conducted on the surface of high purity annealed Ag plates and HIPed 1-2-3 samples. Indentations were made in air at a load of 100 Kg by using a 1/16 inch diameter ball indenter. This combination gives the Rockell B scale. Calculation of the micro-hardness was

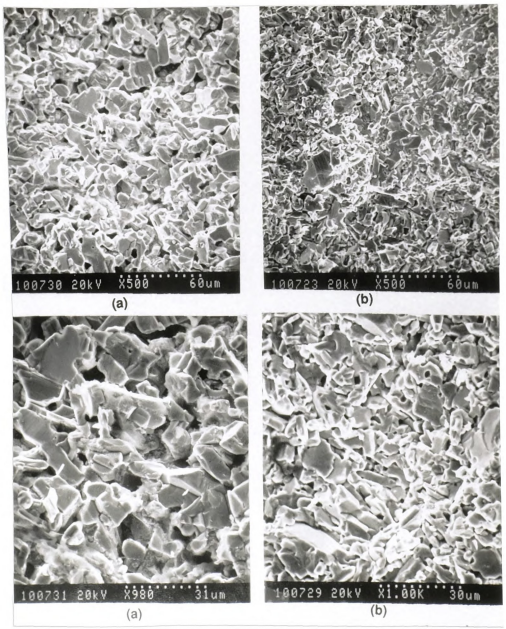

Fig. 44. SEM micrographs, taken from the fractured surface of HIPed 1-2-3 specimens, at different magnifications (x 500 and x 1,000) (a) sintered, (b) HIPed.

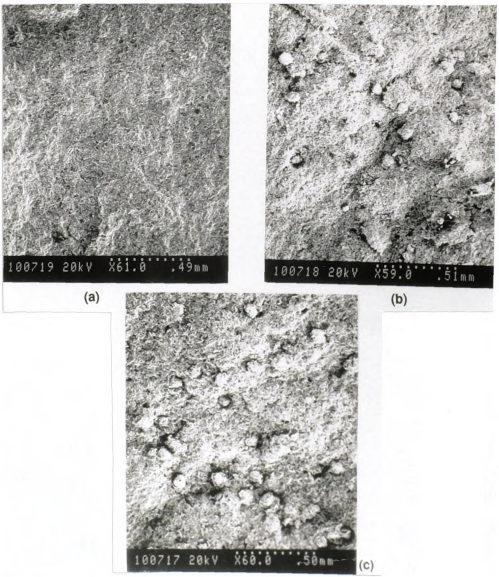

Fig. 45(a). SEM micrographs taken from the fractured surface of HIPed 1-2-3 specimens reinforced by different Ag volume %
(a) 1-2-3 matrix, (b) 5 % Ag, (c) 8 % Ag.

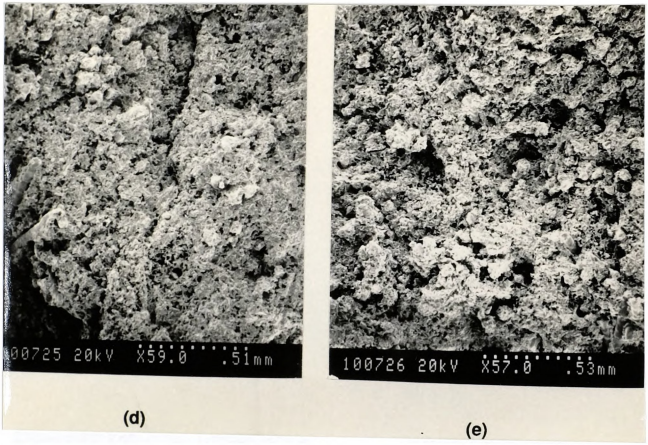

Fig. 45(b). SEM micrographs taken from the fractured surface of HIPed 1-2-3 specimens reinforced by different Ag volume %
(d) 12 % Ag, (e) 15 % Ag.

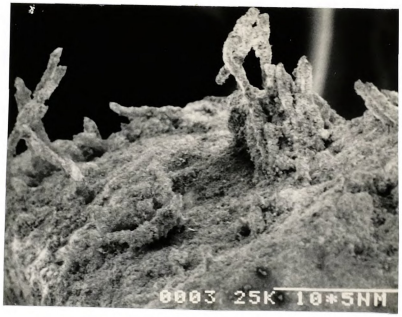

(a)

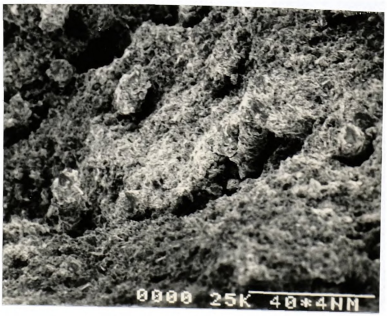

(b)

Fig. 46. SEM micrographs of fracture surfaces of HIPed and Ag reinforced specimen showing: (a) fiber pull-out, and (b) fiber debonding.

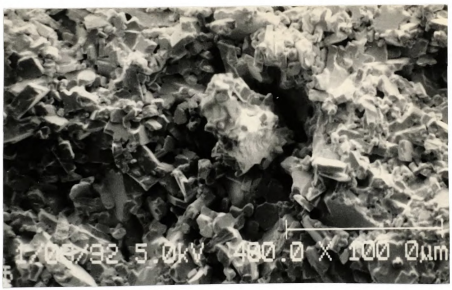

(a)

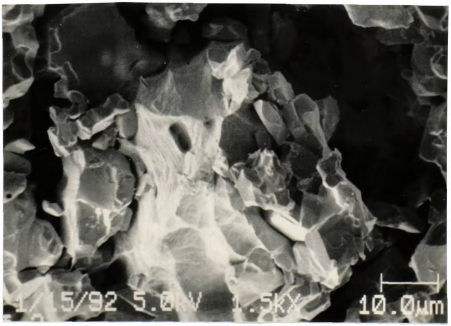

(b)

Fig. 47. SEM micrographs showing damaged Ag fiber in HIPed 1-2-3 matrix (a) x 400, (b) x 1,500.

based on an average of 5 indentation measurements. Measured microhardness value in HR_B scale was 32 for Ag and 68 for 1-2-3, respectively. These results indicate that the hardness of 1-2-3 samples is more than 2 times greater than that of annealed Ag. Thus, It is possible that 1-2-3 phase particles are mechanically embedded on the softer Ag fibers during the pressurization stage of the isostatic pressing. These embedded particles then react with Ag fibers at the sintering temperature to produce a strong adherent layer. Fig. 46 shows indeed such in the case. Therefore, these coated fibers might not necessarily have the same ductility or strength as the virgin Ag fibers.

Another interesting result from both SEM and optical micrographs is the fine grained materials obtained from the HIPing process. Even after prolonged post-annealing at 850°C for 20 hours, the grain size remained almost the same as in the unannealed sample (Fig. 48). This result correlates well with the results by Sadananda et al. [71]. Since the final grain size was attained during the HIPing and not during the annealing process, it can be suggested that grain refinement occured at the interparticle contact areas due to high localized strain produced by the applied pressure. Since HIP processing is conducted at a lower temperature (890°C) than for conventional sintering (925°C), and the HIP processing time (2.5 hours) is compared with the conventional sintering time (24 hours), these factors combine to produce a smaller grain size.

A fine grained materials has higher strength according to the Hall-Petch relationships [107]:

$$\sigma_f = \sigma_o + kd^{-1/2} \qquad (27)$$

where σ_f is the fracture strength, d is the average grain diameter and σ_o and k are obtained from the intercept and slope respectively of the flow stress versus

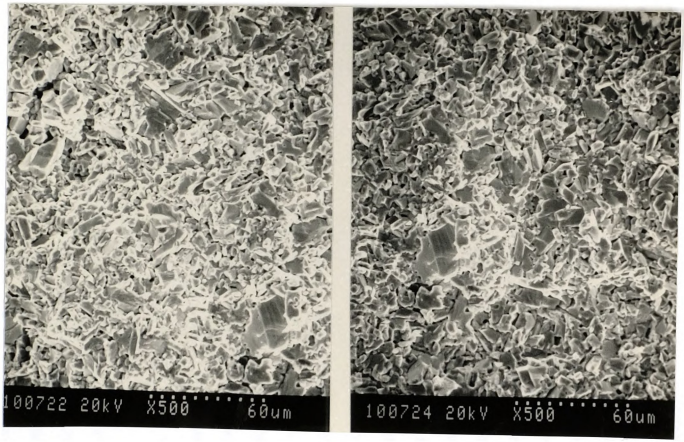

(a) **(b)**

Fig. 48. SEM micrographs taken from the fractured surfaces (x 500)
(a) HIPed specimen without any post-annealing
(b) HIPed with post-annealing, at 850°C for 20 hours.

$d^{1/2}$ plot. Therefore, the fine grain structure, as discussed above, will have a beneficial effort on the mechanical properties (i.e., toughness and tensile strength) of the HIPed superconductor composites.

Returning to superconducting properties, it is well known that the grain size and grain boundary chemistry play important roles in affecting the J_c. A sample with a large grain size, favorably oriented and non-equiaxed grains, and with low porosity, can have a higher critical current density. A fine grain size results in a decrease of current transport capabilities because of the increase in the number of grain boundaries along a conducting path. HIPing is one of effective ways of reducing the porosity and we know that porosity causes the lack of continuity of the superconductive phase across the grain boundaries in sample. If there is no texture formation between neighboring grain boundaries, the proportion of high-angle grain boundaries is increased in a fine grained material. In HIPed composite superconductors, the grains are small and randomly oriented, as has been discussed earlier. Thus, J_c values are still relatively low for the HIPed samples. The secondary product, such as, Y_2BaCuO_5, due to the phase decomposition of 1-2-3, is known to improve J_c through flux pinning. However, it was difficult to detect this phase (2-1-1) by using SEM or optical microscopy.

Micro-cracking in the specimens is one of the detrimental effects which occurs in reinforced composites. It is important to choose materials which have a similar difference between their thermal expansion coefficients in order to avoid micro-crack formation. The coefficient of thermal expansion of the matrix and the fibers are 16.9 x 10^{-6}/K [108] and 19 x 10^{-6}/K [109], respectively. Thus the fibers contract slightly more than the matrix during cooling. It seems that the fibers do not introduce microcracks into the 1-2-3 based matrix due to the thermal expansion mismatch. Because porosity exists between the fiber-matrix

interface and the difference in thermal-expansion coefficients is quite low, stresses generated by the thermal-expansion mismatch could be relieved and the residual stresses may be small. The best composites have a differential expansion coefficient of about 1 to 2 x 10^{-6}/K [106], with $\alpha_f > \alpha_m$ (where α_f and α_m are thermal expansion coefficients of fiber and matrix respectively) for the fibers to have residual tensile stress and the matrix to have residual compression stress during heating. For our present case this condition is satisfied.

4. 6 Microchemistry of Bulk and Interface Regions

4. 6. 1 Energy dispersive x-ray analysis

Energy dispersive X-ray analysis was conducted for regions of 1-2-3 grains and Ag fiber (Fig. 49). Fig. 50(a) shows the elemental energy dispersive x-ray data (EDAX) for the common elements in the 1-2-3 superconductors. The bottom portion of this figure shows a semi-quantitative (without correction factors) analysis of the EDAX data. Fig. 50(b) and 50(c) show similar results for Ag fiber reinforced regions. Fig. 50(b) is that from a large area of the fracture surface and the 50(c) is that from a Ag fiber region.

4. 6. 2 Auger Electron Spectroscopy (AES) analysis

After Auger surface scanning, it was found that the sample surfaces were contaminated by carbon. Sample surface were polished with diamond paste and alumina powder dispersed in methanol (Fig. 51). Even after a 5,000 nm layer was ion-sputtered away, the Auger data (Fig. 52) indicated that the carbon content remained almost the same as before. Due to this carbon contamination,

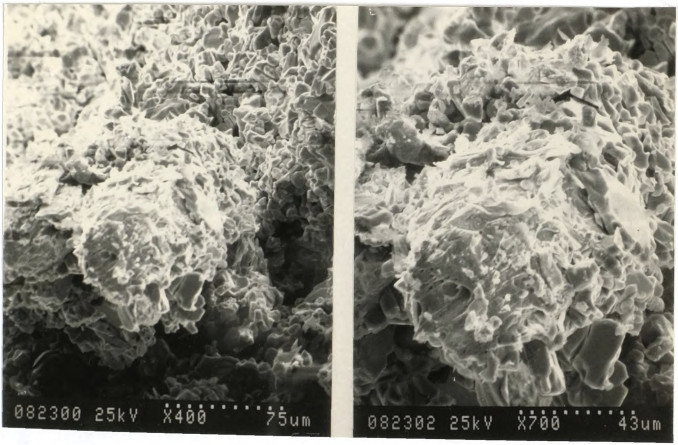

Fig. 49. Fractured surfaces of HIPed specimen examined for EDAX elemental analysis as presented in Figs. 50(a), 50(b) and 50(c) (x 400 and x 700).

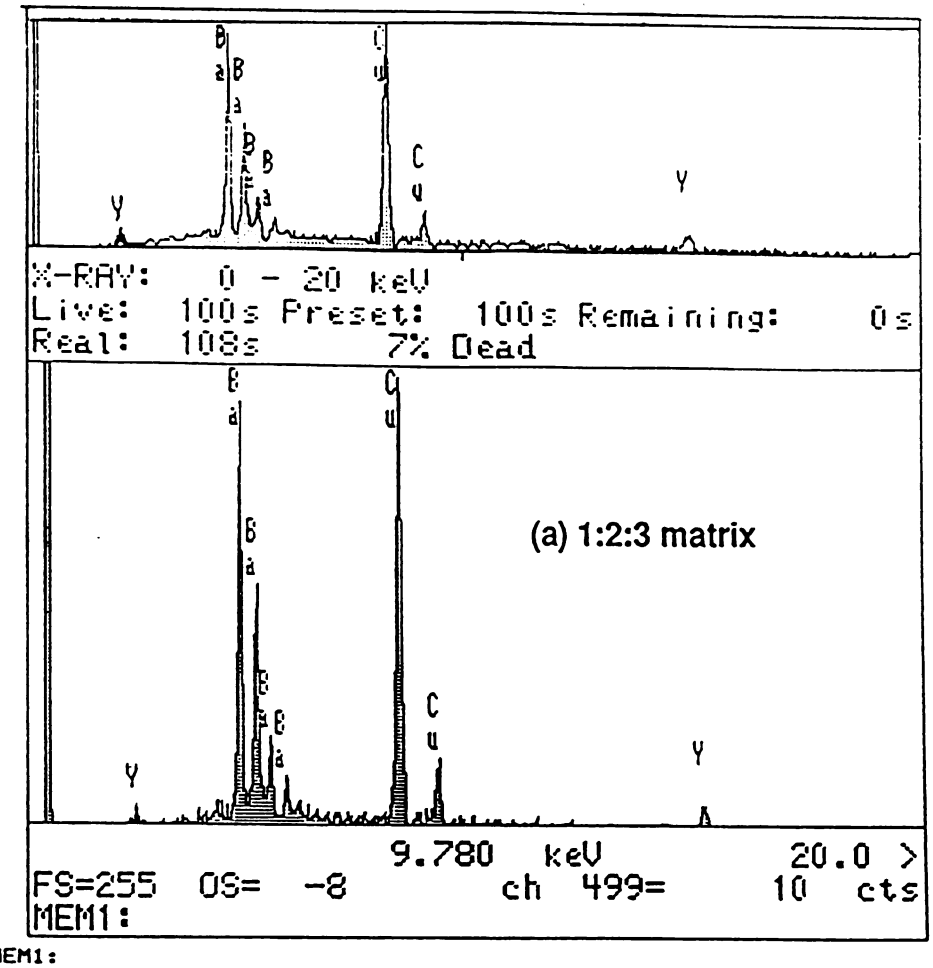

MEM1:

WINDOW LABEL	START keV	END keV	WIDTH CHANS	GROSS INTEGRAL	NET INTEGRAL	EFF. FACTOR	%AGE TOTAL
Y	1.82	2.06	13	1825	948	1.00	1.83
BA	4.36	4.58	12	21327	14655	1.00	28.32
BA	4.72	4.98	14	14682	8487	1.00	16.40
BA	5.08	5.26	10	5557	2257	1.00	4.36
BA	5.44	5.62	10	3183	973	1.00	1.88
CU	7.90	8.20	16	25689	21001	1.00	40.59
CU	8.78	9.06	15	5132	2777	1.00	5.37
Y	14.84	15.08	13	2264	646	1.00	1.25

Fig. 50(a). Elemental analysis by EDAX of a 1-2-3 superconductor.

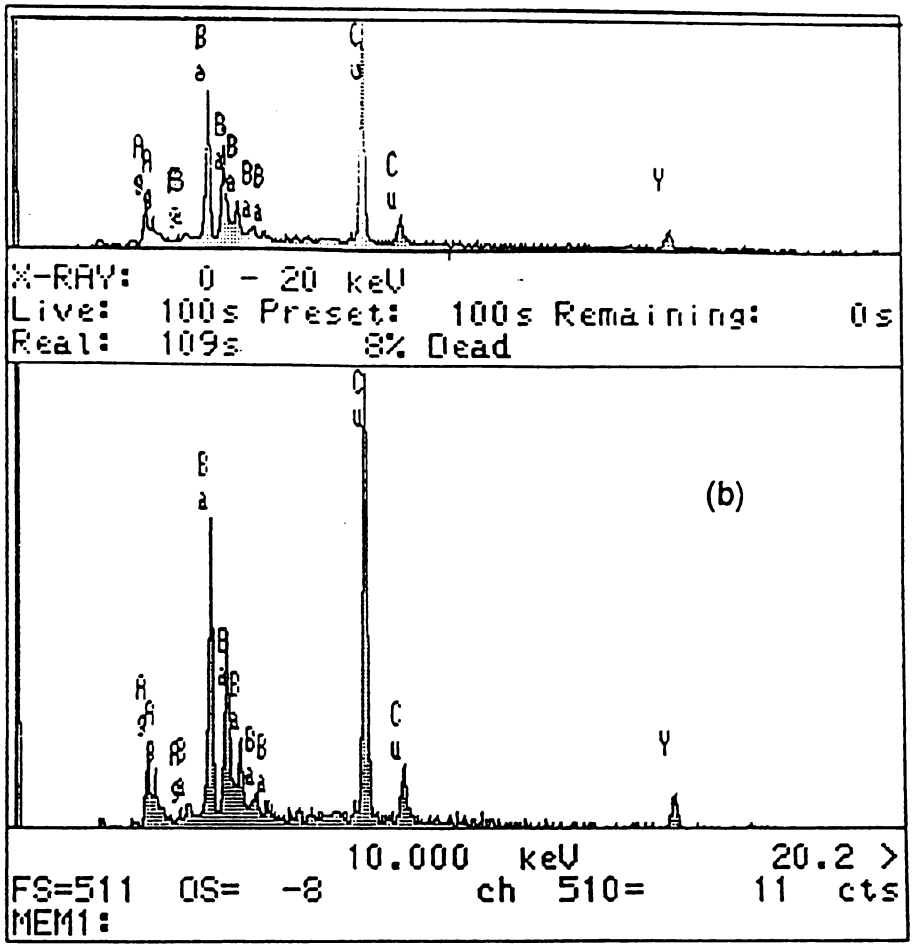

MEM1:

WINDOW LABEL	START keV	END keV	WIDTH CHANS	GROSS INTEGRAL	NET INTEGRAL	EFF. FACTOR	%AGE TOTAL	%AGE RATIO
Ag	2.88	3.30	22	1202	608	1.00	7.23	292.31
Ag	3.72	3.82	6	149	14	1.00	.17	6.73
Ba	3.84	4.08	13	400	56	1.00	.66	26.68
Ba	4.28	5.32	53	5633	3910	1.00	46.52	1880.05
Ba	5.50	5.64	8	335	47	1.00	.56	22.60
Ba	5.72	5.86	8	261	13	1.00	.15	6.25
Cu	7.90	8.20	16	3742	3158	1.00	37.57	1518.27
Cu	8.78	9.02	13	684	392	1.00	4.66	188.22
Y	14.82	15.08	14	439	208	1.00	2.47	100.00

Fig. 50(b). Elemental analysis by EDAX on a fractured surface (with overall area scanning).

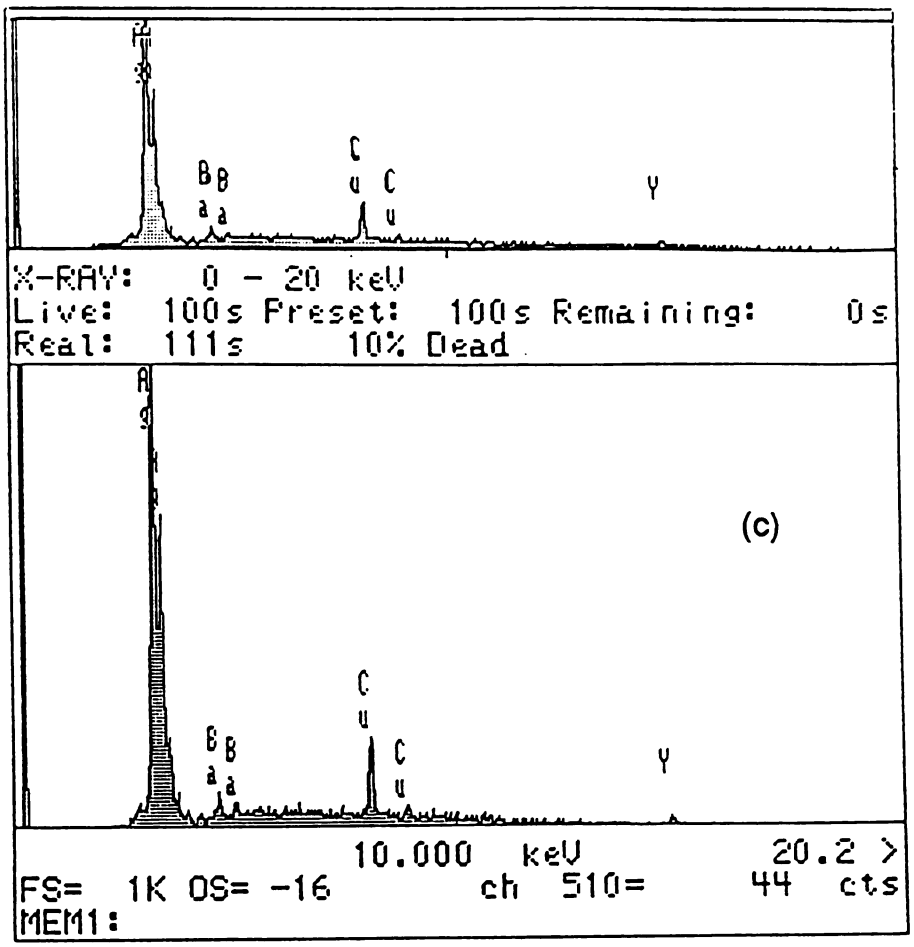

MEM1:

WINDOW LABEL	START keV	END keV	WIDTH CHANS	GROSS INTEGRAL	NET INTEGRAL	EFF. FACTOR	%AGE TOTAL
Ag	2.80	3.44	33	15097	12639	1.00	91.69
Ba	4.38	4.56	10	719	149	1.00	1.08
Ba	4.78	4.98	11	690	151	1.00	1.10
Cu	7.96	8.18	12	1708	694	1.00	5.03
Cu	8.86	9.00	8	464	56	1.00	.41
Y	14.82	15.06	13	362	96	1.00	.69

Fig.50(c). Elemental analysis by EDAX of a region of Ag fiber.

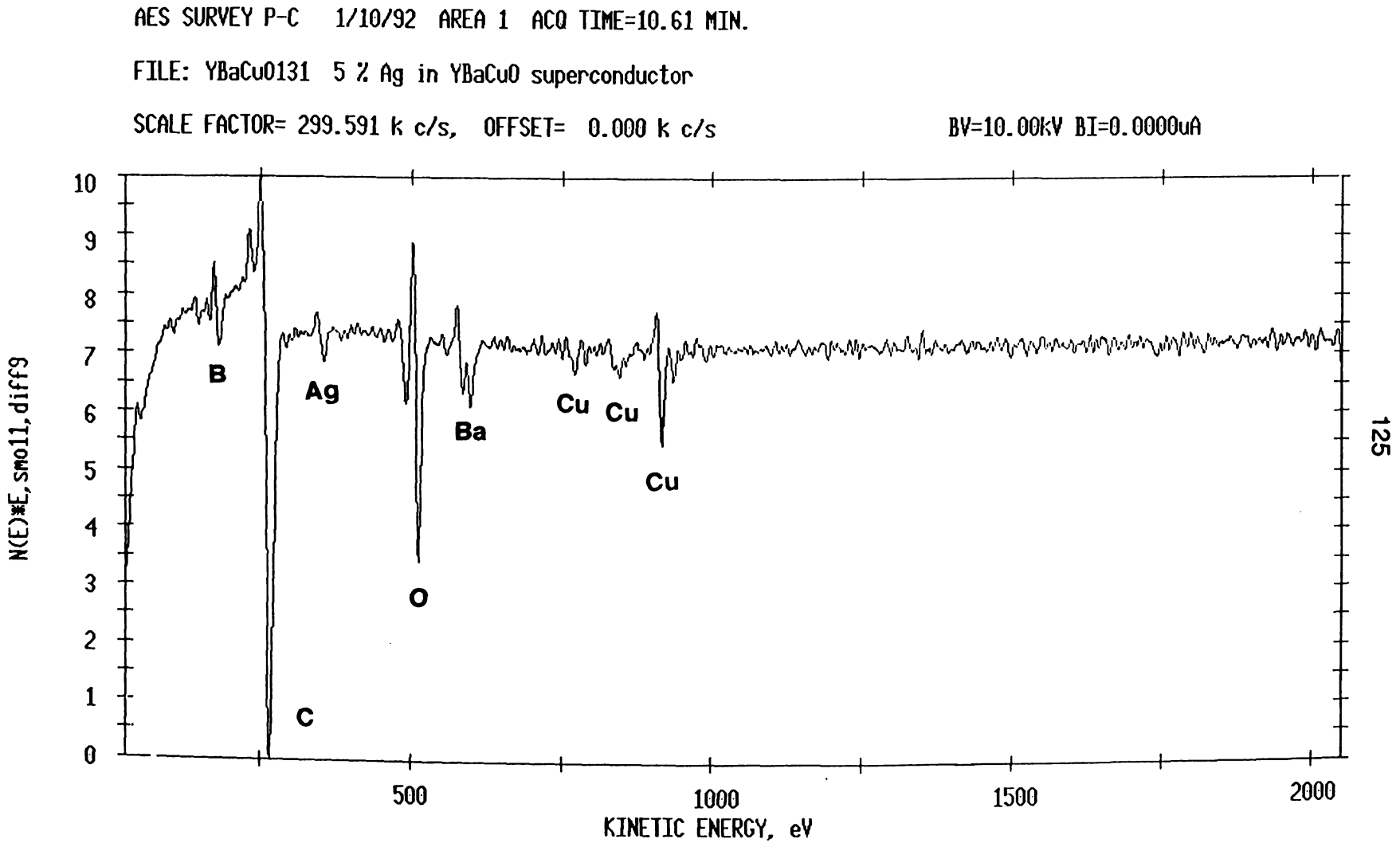

Fig. 51. AES spectra taken from the polished surface of a HIPed specimen reinforced with 5 volume % Ag.

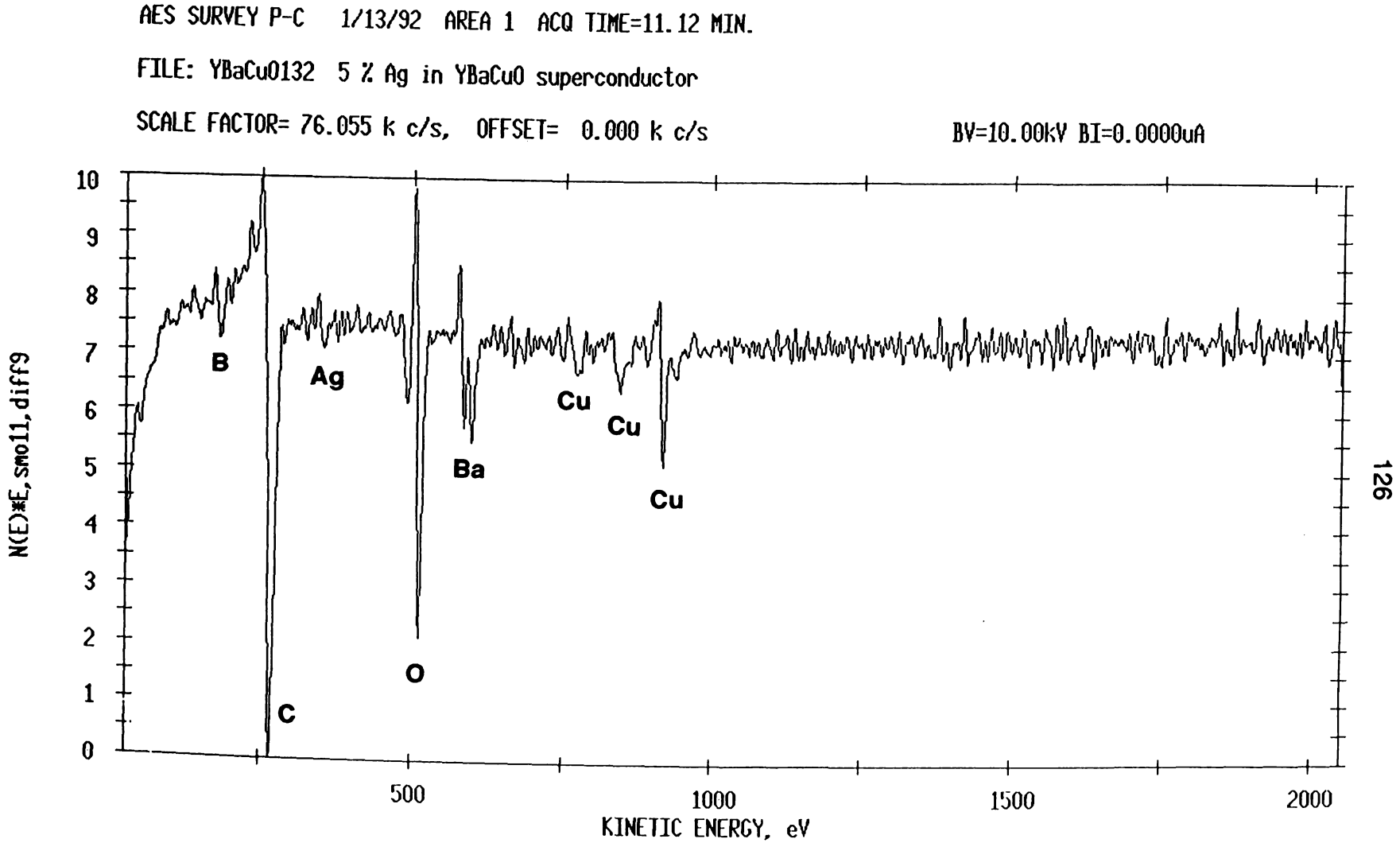

Fig. 52. AES spectra taken from the polished surface of a HIPed specimen reinforced with 5 volume % Ag after ion sputtering.

all elemental intensities were reduced.

All samples fractured at room temperature showed that the Ag fiber was debonded from matrix during fracturing, and fibers were covered with very fine grains of 1-2-3 phase. Specimens fractured at cryogenic temperatures, were used to study the fiber-matrix interface.

Figures. 53 and 54 show the typical Auger electron spectra in terms of the derivative (N(E) * E) and the kinetic energy modes before and after ion sputtering of the fractured surface (Fig. 26). All of the peaks in the spectra can be accounted for by the components of the compound. After ion sputtering, carbon peaks remained even though the intensity of the carbon peak was somewhat reduced. The presence of a small quantity of carbon is most likely due to the contamination of the high vacuum system (please note that this system is also used to study polymeric materials) [110]. Small amounts of boron were also detected. This suggests that there was a possible surface reaction between the boron nitride used during HIPing and the specimen.

From the line scan data (Fig. 55) taken on the same fracture surface, the oxygen concentration, which is based on the molar ratio of the 1-2-3 system, was somewhat lower than expected. This might indicate a loss of surface oxygen in the high vacuum environment [111]. At the same time this data indicates that oxygen did not diffuse very far into the Ag fibers. The line scanning was carried out from the interface between matrix and Ag fiber well into the Ag fiber. Thus, the result suggests that at the HIPing temperature, the oxygen diffusion rate into Ag is quite low. However, diffusion of Ag into 1-2-3 matrix phase could not be detected conclusively. The line scan seems to show that the interface between the matrix and the Ag fiber is not sharp. One possible explanation is that elements of the matrix phase has diffused into the Ag fiber during processing.

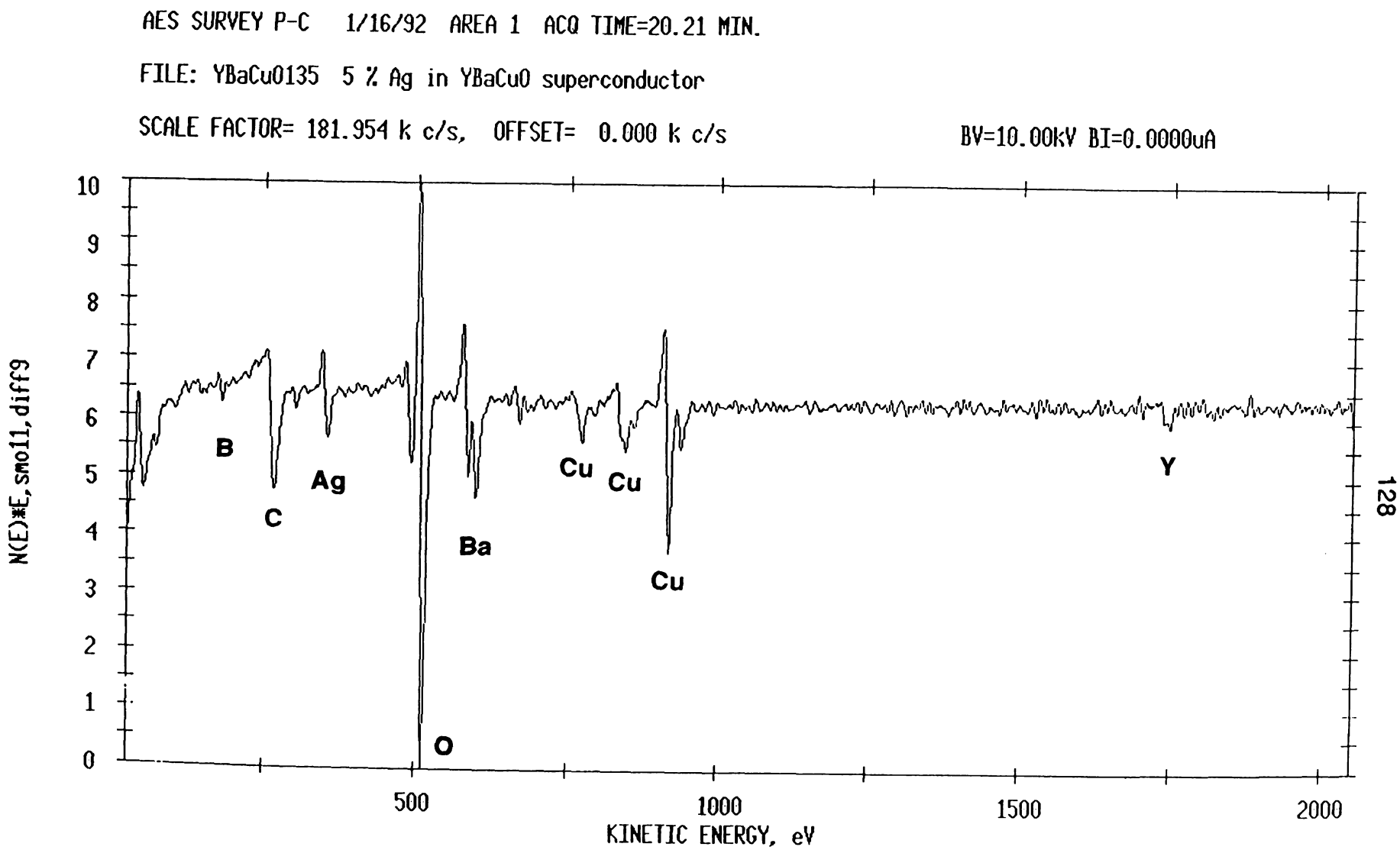

Fig. 53. AES spectra taken from the fractured surface of a HIPed specimen reinforced with 5 volume % Ag.

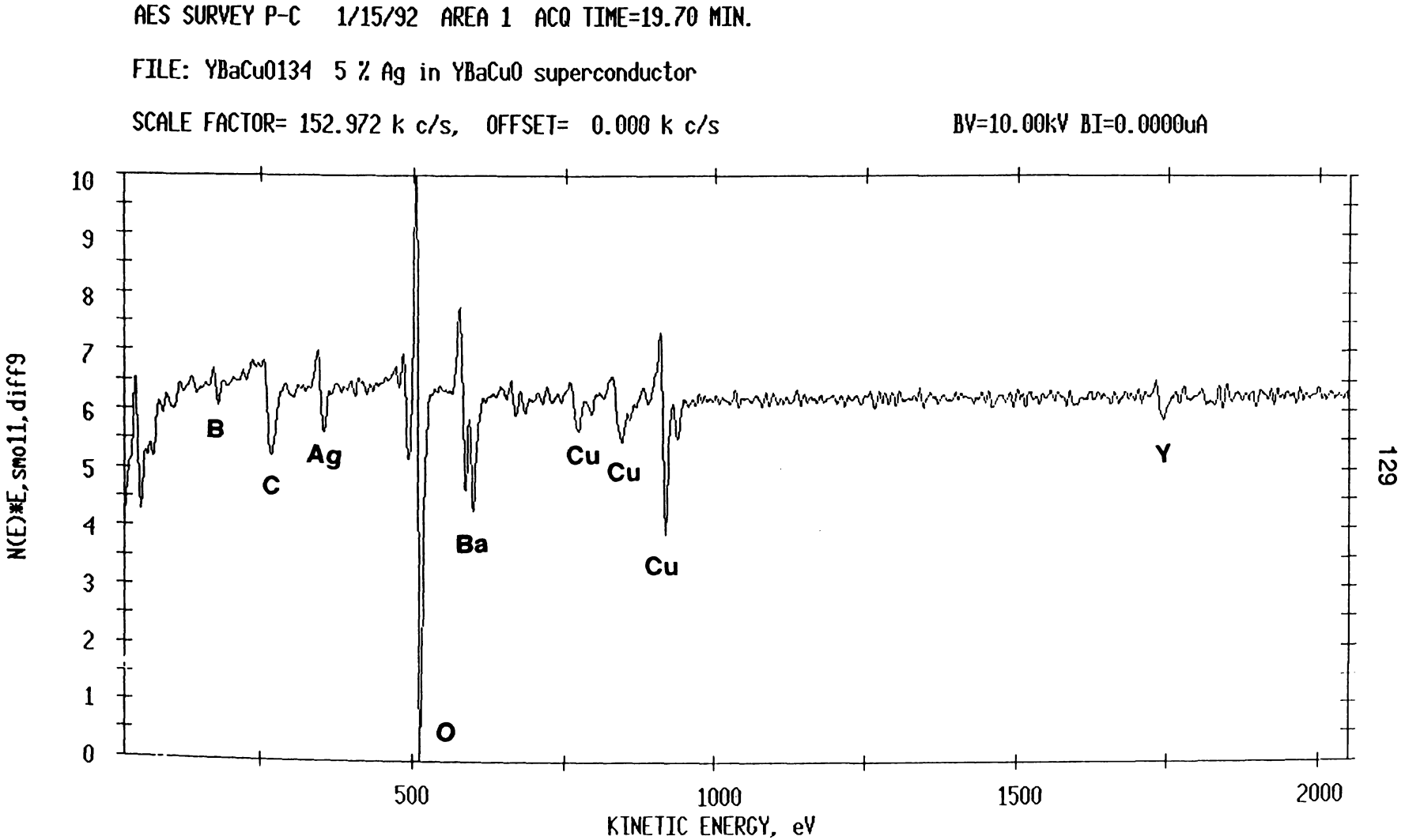

Fig. 54. AES spectra taken from the fractured surface of a HIPed specimen reinforced with 5 volume % Ag after ion sputtering.

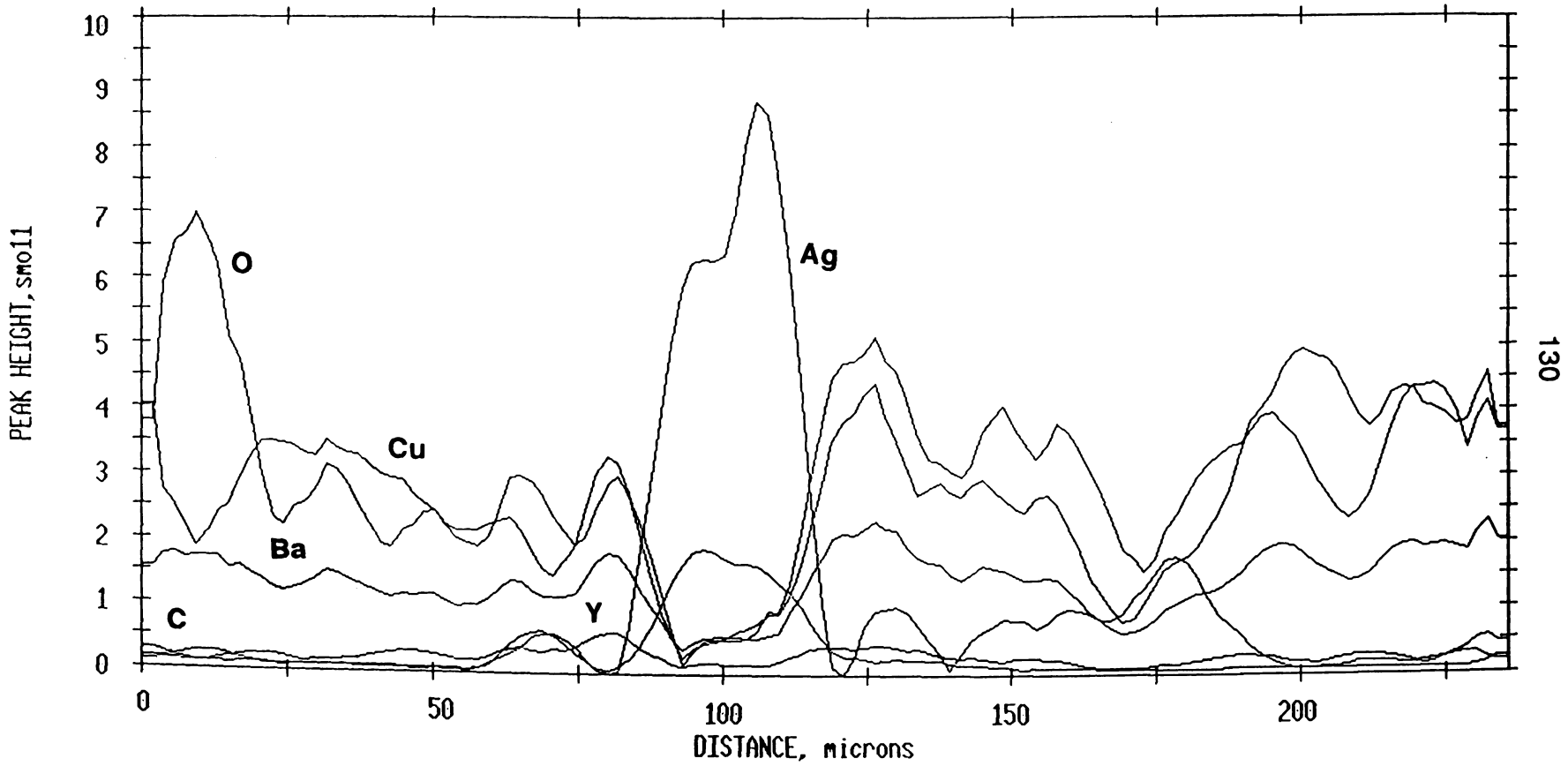

Fig. 55. AES spectra in the line scanning mode, taken from the fractured surface of a HIPed specimen reinforced with 5 volume % Ag.

It is known that yttrium has a relatively low sensitivity for Auger transition [97]. Therefore, the excitation of the Auger transition was difficult with a 5 keV beam voltage (Fig. 56). However, when a 15 keV electron beam was applied to increase the Auger sensitivity for yttrium, significant radiation damage occured on the fracture surface. Fig. 57 shows one of the fractured surfaces damaged by electron radiation upon application of 15 keV for 3 hours. Please note the glassy appearance of the surface which strongly suggests melting and vitrification.

Figure 58 shows dot-mapped AES images for different elements (Y, Ba, Cu, O and Ag) with different contrasts. Yttrium element (Fig. 58(a)) was lightly and uniformly scattered on the surface (Fig. 26) while barium (Fig. 58(b))and oxygen elements (Fig. 58(d)) were heavily distributed on the surface. In a dot-maped image, representing barium and oxygen elements, dark background indicates the presence of deep porosity or other elements such as silver. However, in some sections of the fractured surface (in as Fig 26), the copper rich phases were observed as clusters, based on the copper dot-mapped image (Fig. 58(c)). Silver fibers were detected clearly as large bright spots and silver fibers can be seen in several other areas. Only one silver fiber was selected by SEM in Fig. 26, on which dot-mapping was performed. However, as pointed out in discussing the line scan data, interfaces between Ag fibers and matrix are not well defined because some of the 1-2-3 grains (shown as dark image in silver fiber itself) are deposited on or attached to the silver fibers. In this experiment, Auger electrons of each elements were detected around 500 nm from the surface.

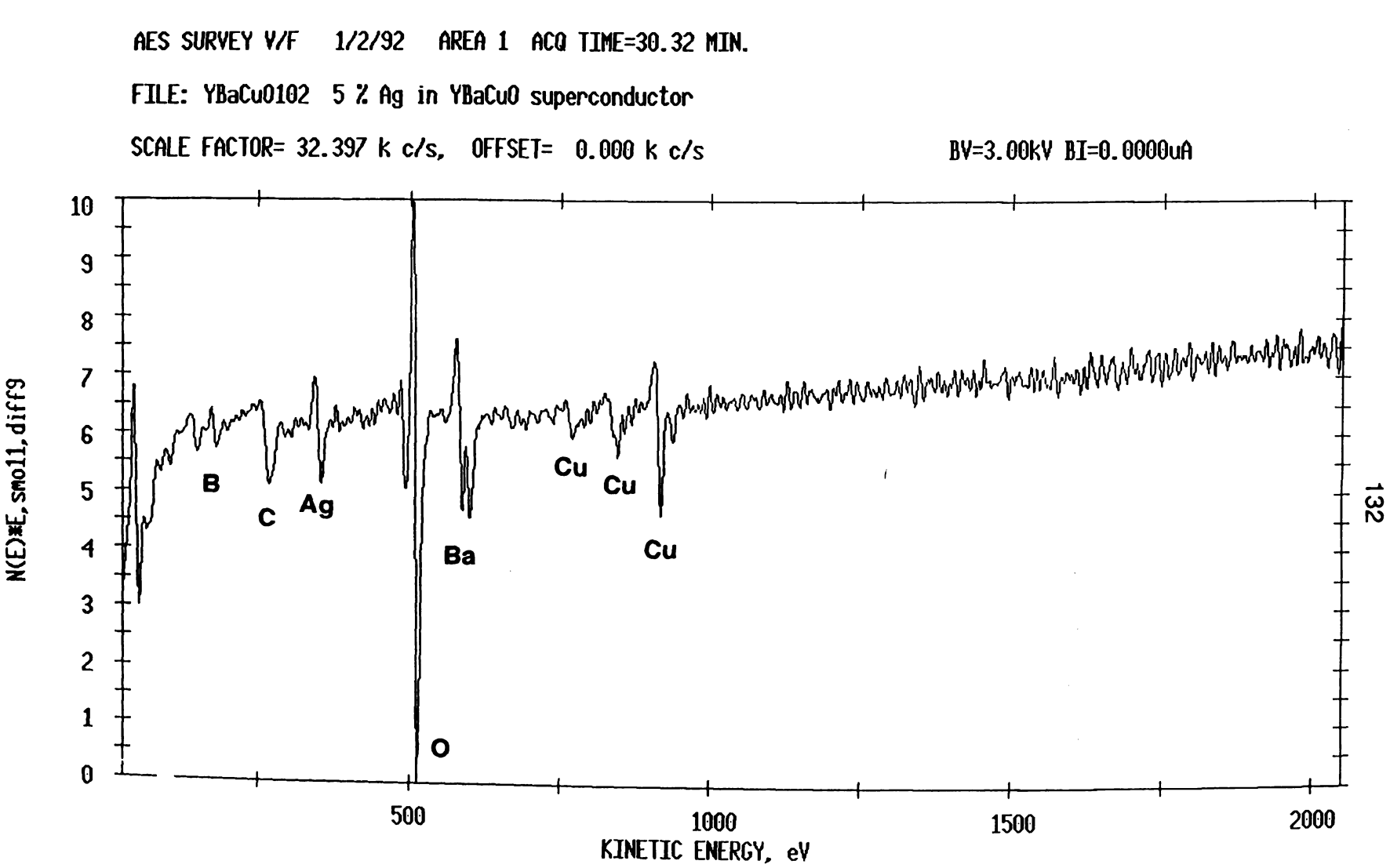

Fig. 56. AES spectra with 5 keV excitation energy, taken from the fractured surface of a HIPed specimen reinforced with 5 volume % Ag.

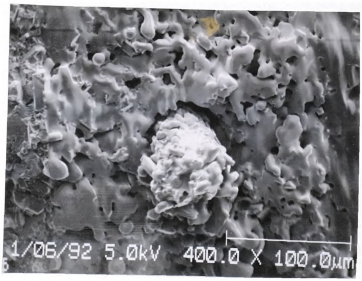

Fig. 57. Fracture surface of a HIPed specimen reinforced with 5 volume % Ag which exhibits electron beam radiation damage at 15 keV excitation energy. Rounded projections indicate melting.

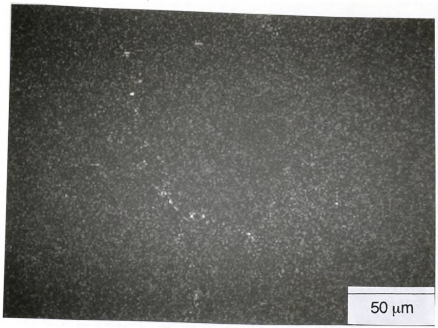

(a)

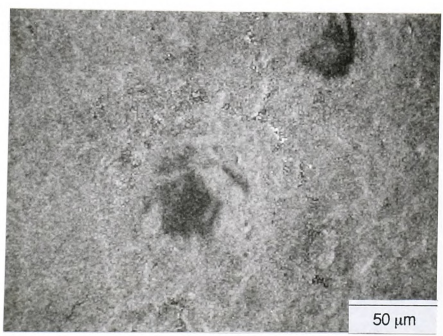

(b)

Fig. 58(a). AES image produced by compositional dot-mapping, taken from the fractured surface of a HIPed specimen reinforced with 5 volume % Ag; (a) mapping of yttrium, (b) mapping of barium.

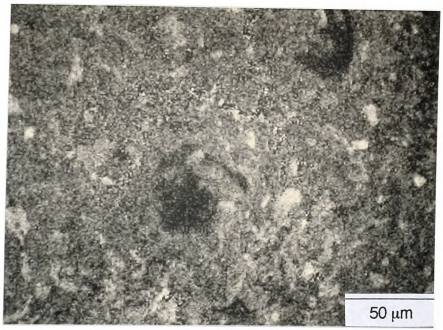

(c)

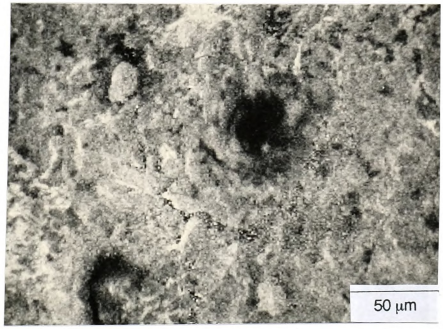

(d)

Fig. 58(b). AES image produced by compositional dot-mapping, taken from the fractured surface of a HIPed specimen reinforced with 5 volume % Ag; (c) mapping of copper, (d) mapping of oxygen.

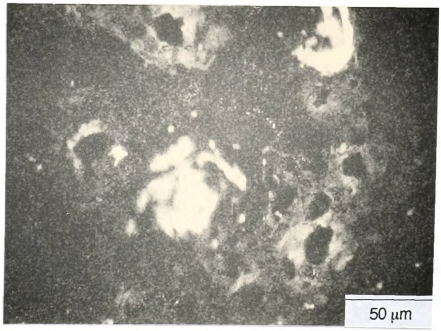

(e)

Fig. 58(c). AES image produced by compositional dot-mapping, taken from the fractured surface of a HIPed specimen reinforced with 5 volume % Ag; (e) mapping of silver.

5. CONCLUSIONS

The objective of this research is to evaluate the feasibility of obtaining dense superconducting composites, which have a critical temperature > 77 K, a reasonable critical current density, and which have a greater fracture toughness. After investigating several types of reinforcement materials, Ag fibers were chosen because Ag fibers produced the minimum degradation of superconducting properties. To meet research objectives, specimens were fabricated by using two different processing techniques; one by conventional sintering and the other by HIPing. In this research, physical, electrical and mechanical properties of Ag fiber reinforced $YBa_2Cu_3O_{7-x}$ superconductor composites have been systematically investigated as a function of volume % fibers and processing techniques. Following are the main conclusions of this research:

1. In the non-superconducting state, the temperature dependance of the electrical resistance decreased systematically as the Ag volume % increased. Increasing volume % of Ag, however, did not have any significant negative effects on T_c and J_c. In fact, J_c increased by a factor of almost 2 for the reinforced and HIPed samples compared with unreinforced samples.

2. HIPed specimens, with different volume percents of Ag, have a superconducting onset temperature range of 90 to 92 K. In all of the cases zero resistance state occurred at approximately 88 to 90 K. The critical temperature data agree well with transition temperature determined from magnetic susceptibility studies.

3. HIPed sample shows a higher densification with approximately 5 % porosity as compared with the conventioally processed samples. Since porosity adversely affects both the electrical and mechanical properties, HIP densification method for processing is recommended.

4. A significant improvement of fracture toughness of $YBa_2Cu_3O_{7-x}$ superconductor can be obtained by Ag fiber reinforcement and HIP processing. For example, the value of K_{Ic}, (4.5 MPa $m^{1/2}$), in a specimen with 15 % Ag-fiber, increased by a factor of 4 over that for an unreinforced specimens, (1.2 MPa $m^{1/2}$).

5. With the addition of Ag fibers, the fracture energy, γ_F, was found to increase linearly but the fracture strength,σ_F, decreased systematically.

6. Some decomposition of the 1-2-3 phase occurred in the HIPed samples at a temperature of 890°C under 170 MPa.

7. A fine-grained consolidated superconductor composite was obtained after HIPing. It is believed that this fine grain size is a limitation to a dramatic improvement in J_c. J_c could be improved by texturing and/or grain growth. Our initial efforts to produce grain growth in these samples were not successful. It was found that increased HIPing temperature, which might promote grain growth, had an adverse effect on superconducting properties due to phase decompositions.

8. Although J_c is not very large in samples processed in this research, the gain in mechanical stability, retention of a relatively high critical temperature and a modest improvement in J_c will make this processing techniques useful for developing some engineering devices (e.g. low current carrying electrical busses, switches etc.).

APPENDIX

1. Research history

Prior to using Ag fibers, 3 different types of reinforcing materials were investigated. First, carbon fibers with a 5 μm diameter were consolidated into a 1-2-3 matrix. However, the carbon fibers reacted with oxygen, decomposed and did not reinforce the 1-2-3 matrix.

Second, copper fibers with a 15 μm diameter was introduced into the matrix and processed. The copper fibers similarly oxidized during sintering. Fig. 59 shows the as received Cu fiber and Figs. 60(a) and 60(b), different aspects of the oxidized copper fiber after heating to 930°C for 3 hours in air.

Third, the copper fiber was cladded with about 0.2 mm of silver by using an electroless plating technique [112]. The silver plating material was chosen because the element silver was known to have little or no effect on the superconducting properties of $YBa_2Cu_3O_{7-x}$. This technique produced a considerably thick plating in a short time. This process actually is a controlled reduction process of a metal ion species by a chemical reducing agent. A general equation for this type of reaction for deposition on a metallic substrate (M_S) is

$$M^{+2} + \text{reducer} \longrightarrow M^{o} \text{ (on } M_S) + \text{reaction products} \quad (29)$$

In this experiment, the reducer was 50 g/l of potassium iodide, which reacted with 500 g/l of silver nitrate. Basic procedures for this technique were as follows. First to remove the oxidized layer, the copper surface was dipped into a dilute nitric acid for few seconds at room temperature and then immediately

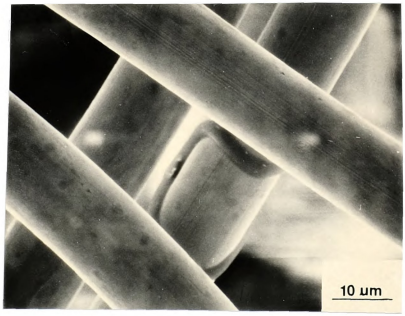

Fig. 59. Scanning electron micrograph of as received Cu fibers (x 250).

(a)

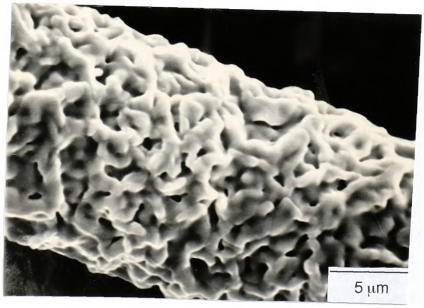

(b)

Fig. 60(a). SEM micrographs showing the oxidation of Cu fibers at the sintering temperature of 930°C for a sintering in air for 3 hours; (a) x 250, (b) x 1,500.

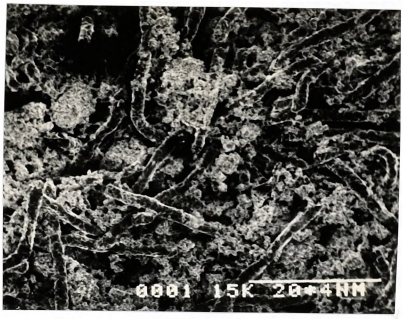

(a)

(b)

Fig. 60(b). SEM micrographs showing oxidized Cu fibers in the matrix of 1-2-3 compound after sintering at 930°C for 3 hours in air; (a) x 150, (b) x 600.

rinsed with distilled water. The plating solution was made by mixing two chemicals; potassium iodide and silver nitrate, at 100°C. Clean copper fibers (as described above) were immersed in the hot solution. Plating thickness increased with time and with increasing solution temperature. Although, exhibiting good adhesion, the silver deposited was somewhat porous and may not be protected from oxidation and mechanical damage. Fig. 61(a) and Fig. 61(b) show several SEM micrographs of copper fibers after the silver deposition. After cladding with silver, copper fibers were embedded into 1-2-3 matrix for synthesis. The detrimental effect during this process was the Cu-Ag eutectic phase formation at approximately 800°C. The liquid eutectic alloy drained out, leaving behind a sponge and much weakened Cu fiber skeleton. These remaining fibers did not bond well with the matrix and they did not contribute to the mechanical properties of the composite in a positive way. Fig. 62 shows typical SEM micrographs taken at different magnifications after sintering. Fig. 63 is the phase diagram of Ag-Cu system [113]. Since Ag metal did not react, per se, with the 1-2-3 matrix, it was then decided to conduct our experiments with pure Ag fibers.

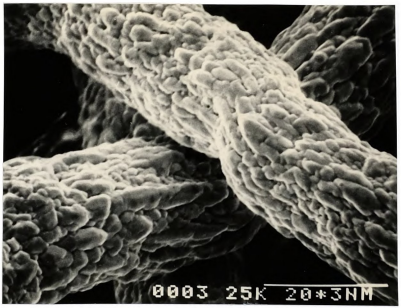

Fig. 61(a). SEM micrographs showing surface morphology of Ag coating on Cu fibers (x 1,200).

Fig. 61(b). SEM micrographs of the cross sectional area of Ag coated Cu fibers (x 500).

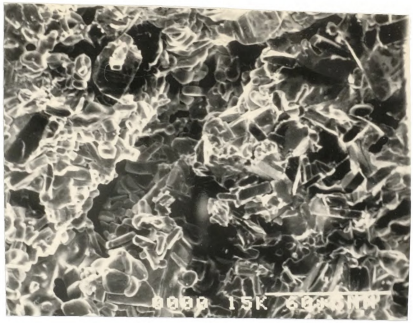

(a)

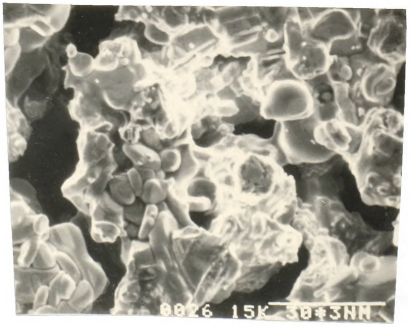

(b)

Fig. 62. Fractured surface of 1-2-3 compound reinforced with Ag coated Cu fibers. Samples were prepared by sintering at 930°C for 24 hours. (a) x 250, (b) x 1,000.

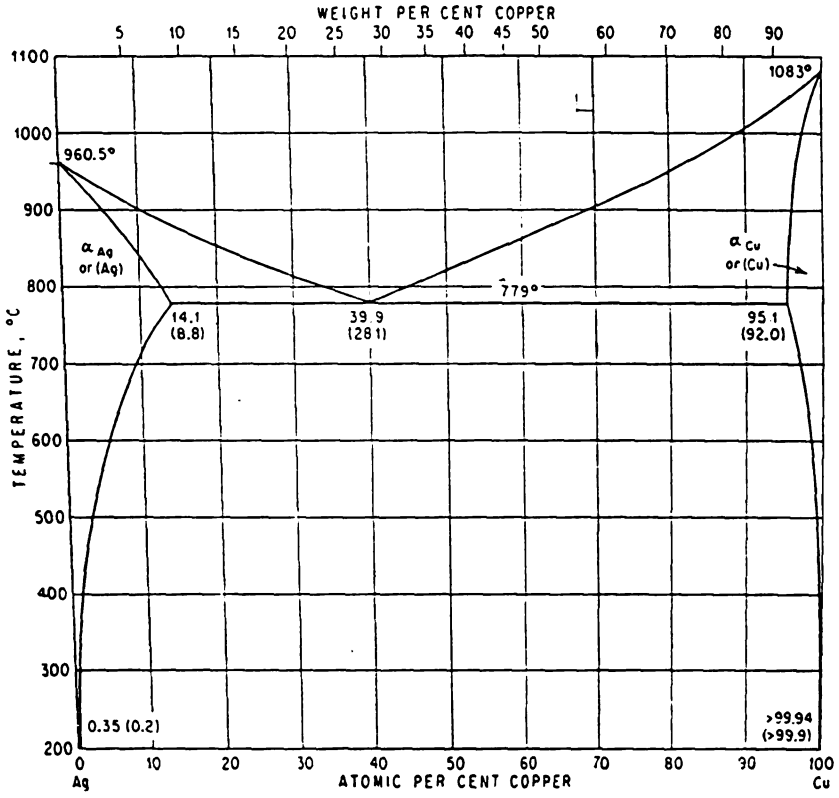

Fig. 11. Ag-Cu

Fig. 63. Equilibrium phase diagram of Ag-Cu system (Ref. 113).
Note that the eutectic temperature is below the sintering temperature.

REFERENCES

1. C. W. Chu, P. H. Hor, R. L. Meng, L. Cao and Z. J. Huang, Science, 235, 567 (1987)

2. Y. H. Kao, Y. D. Yao, L. Y. Jang, F. Xu, A. Krol, L. W. Song, C. J. Sher, A. Darovsky and J. C. Phillips, J. Appl. Phys., 67, 353 (1990)

3. F. Deslandes, B. Raveau, P. Dubots and D. Legat, Solid State Commun., 71, 407 (1989)

4. G. Xiao, F. H. Streitz, M. Z. Cieplak, A. Bakhshrai, A. Gavrin and C. L. Chien, Phys. Rev., B 38, 776 (1989)

5. V. Plechacek, V. Landa, Z. Blazek, J. Sneidr, Z. Trejalova and M. Cermak, Physica C, 153, 878 (1989)

6. J. G. Bednorz and K. A. Müller, Z. Phys., B 64, 189 (1986)

7. R. J. Cava, B. Batlogg, R. B. Van Dover, D. W. Murphy, S. Sunshine, T. Siegriest, J. P. Rameika, E. A. Reitman, S. Zahurak and G. P. Espionosa, Phys. Rev. Lett., 58, 1676 (1987)

8. C. W. Chu, P. H. Hor, R. L. Meng, L. Cao and Z. J. Huang, Z. J. Phys. Rev. Lett., 58, 405 (1987)

9. J. Cava, R. B. Van Dover, B. Batlogg and E. A. Rietman, Phys. Rev. Lett., 58, 408 (1987)

10. P. H. Hor, R. L. Meng, Y. Q. Wang, L. Cao, Z. J. Huang, J. Bechtold, K. Foster and C. W. Chu, Phys. Rev. Lett., 58, 1891 (1987)

11. G. Xiao, F. H. Streitzm, A. Gravrin, Y. W. Du and C. L. Chien, Phys. Rev., B 35, 8782 (1987)

12. T. Siegrist, L. F. Schneemeyer, J. V. Waszczak, N. P. Singh, R. A. Opila, B. Batlogg, L. W. Rupp and D. W. Murphy, Phys. Rev., B 36, 8365 (1987)

13. Z. Z. Sheng and A. M. Hermann, Nature, 332, 55 (1988)

14. Z. Z. Sheng, A. M. Hermann, A. El Ali, C. Almason, J. Estrada, T. Datta and R. J. Matson, Phys. Rev. Lett., 60, 937 (1988)

15. Z. Z. Sheng and A. M. Hermann, Nature, 332, 138 (1988)

16. C. Michel, M. Hervieu, M. M. Bored, A. Grandin, F. Deslandes, J. Provost and B. Raveau, Z. Phys., B 68, 421 (1987)

17. C. W. Chu, J. Bechtold, L. Gao, P. H. Hor, Z. J. Huang, R. L. Meng, Y. Y. Sun, Y. Q. Wang and Y. Y. Xue, Phys. Rev. Lett., 60, 941 (1988)

18. J. M. Tarascon, L. H. Greene, P. Barboux and G. W. Hull, Phys. Rev., B 36, 8393 (1987)

19. G. Xiao, F. H. Streitz, A. Gavrin and C. L. Chien, Phys. Rev., B 35, 8782 (1987)

20. M. F. Yan, W. W. Rhodes and P. K. Gallagher, J. Appl. Phys., 63, 821 (1988)

21. S. R. Ovshinsky, R. T. Young, D. D. Allred, G. DeMaggio and G. A. Van der Leeden, Phys. Rev. Lett., 24, 2579 (1987)

22. M. F. Yan, G. Sageev Grader and W. W. Rhodes, J. Mat. Sci., 24, 703 (1989)

23. Narottam P. Bansal, and Ann L. Sandkuhl, Appl. Phys. Lett., 52, 838 (1988)

24. S. H. Jin, J. Met., Mar., 7 (1991)

25. M. K. Wu, J. R. Ashburn, C. J. Torng, P. H. Hor, R. L. Meng, J. Bechtold, K. Foster and C. W. Chu, Phys. Rev. Lett., 58, 908 (1987)

26. R. Beyers, G. Lim, E. M. Engler, R. J. Savoy, T. M. Shaw, T. R. Dinger, W. J. Gallagher and R. L. Sandstrorm, Appl. Phys. Lett., 50, 1919 (1987)

27. F. Galasso, J. Met., June, 8 (1987)

28. F. Beech, S. Miraglia, A. Santoro and R. S. Roth, Phys. Rev., B 35, 8778 (1987)

29. A. K. Singh, L. E. Richards, H. A. Hoff, V. Letourneau and C. S. Pande, J. Appl. Phys., 63, 5805 (1988)

30. W. I. F. David, W. T. A. Harrison and J. D. Grace, Nature, 327, 310 (1987)

31. H. Ledbetter, J. Met., Jan., 24 (1988)

32. J. D. Jorgensen, B. W. Veal, W. K. Kwok, G. W. Crabtree, A. Umezawa, L. J. Nowicki and A. P. Paulikas, Phys. Rev., B 36, 5731 (1987)

33. T. R, Dinger, R. F. Cook and D. R. Clarke, Appl. Phys. Lett., 51, 454 (1987)

34. R. F. Cook, T. M. Shaw and P. R. Duncombe, Adv. Ceram. Mat., 2, 606 (1987)

35. J. E. Blendal, C. K. Chiang, D. C. Cranmer, S. W. Freiman, E. R. Fuller, Jr., and D. E. Newbury, Adv. Ceram. Mat., 2, 512 (1987)

36. H. Fujimoto, M. Murakami, T. Oyama, Y. Shiohara, N. Koshizuka and S. Tanaka, Jap. J. Appl. Phys., 29, L1793 (1990)

37. T. Nishio, Y. Itoh, F. Ogasawara, M. Suganuma, Y. Yamada and U. Mitzutani, J. Mat. Sci., 24, 3228 (1989)

38. D. Lee and K. Salama, Appl. Phys. Lett., 29, L2017 (1990)

39. C. Vipulanandan, S. Salib and K. Ravi-Chandar, Mat. Res. Bull., 24, 1059 (1989)

40. S.Salib, C. Vipulanandan and T. Stone, Proc. of the MRS Fall Mtg., Boston, MA, 1989

41. K. C. Goretta, M. Kullberg, D. Bar, S. E. Dorris, U. Balachandaran, R. B. Poeppel and J. C. Routbort, Proc. of the Met. Soc. Spring Mtg., Anaheim, CA, 1990

42. S. Jin, R. C. Sherwood, T. M. Tiefel, R. B. vanDover and D. W. Johnson, Jr., Appl. Phys. Lett., 51, 203 (1987)

43. B. R. Weinberger, L. Lynds, D. M. Potrepka, D. B. Snow, C. T. Burila, H. E. Eaton, Jr. and R. Cipolli, Physica C, 161, 91 (1989)

44. D. Pavuna, H. Berger, J. L. Tholence, M. Affronte, R. Sanjines, A. Dubas, Ph. Bugnon and F. Vasey, Physica C, 153, 1339 (1988)

45. J. P Singh, H. J. Leu, R. B. Poeppel, E. van Voorhees, G. T. Goudey, K. Winsley and D. Shi, J. Appl. Phys., 66, 3154 (1989)

46. G. Kozlowski, S. Rele, D. F. Lee and K. Salama: to be published in J. Mat. Sci.

47. M. K. Malik, V. D. Nair, A. R. Biswas, R. V. Raghaven, P. Chaddah, P. K. Mishira, G. Ravi Kumar and B. A. Dasannacharya, Appl. Phys. Lett., 52, 1525 (1988)

48. N. Imanaka, F. Saito, H. Imai and G. Adachi, Jpn. J. Appl. Phys., 28, L580 (1989)

49. T. H. Tiefel, S. Jin, R. C. Sherwood, M. E. Davis, G. W. Kammmlott, P. K. Gallagher, D. W. Johnson, Jr., R. A. Fastnacht and W. W. Rhodes, Mater. Lett., 7, 363 (1989)

50. T. Oka, F. Ogasawara, Y. Itoh, M. Suganuma and U. Mizutani, Jap. J. App. Phys., 29, 1924 (1990)

51. J. W. Ekin, A. I. Braginski, A. J. Panson, M. A. Janocko, D. W. Capone, H. N. J. Zaluzec, B. Flandermeyer, O. F. deLima, M. Hong, J. Kwo, and S. H. Liou, J. Appl. Phys., 62, 4821 (1987)

52. G. J. Yrrek, J. B. Vander Sande, D. A. Rudman and Y. M. Chiang, J. Met., Jan., 16 (1988)

53. R. B. Laibowitz, R. H. Koch, P. Chaudari and R. J. Gambino, Phys. Rev., B 35, 8821 (1987)

54. L. F. Schneemeyer, E. M. Gyorgy and J. V. Waszczak, Phys. Rev., B 36, 8804 (1987)

55. T. R. Dinger, T. K. Worthington, W. J. Gallagher and R. L. Sandstrom, Phys. Rev. Lett., 58, 2687 (1987)

56. T. K. Worthington, W. J. Gallagher and T. R. Dinger, Phys. Rev. Lett., 59, 1160 (1987)

57. J. W. Ekin, Adv. Ceram. Mat., 2, 586 (1987)

58. D. Dimos, P. Chaudhari and J. Mannhart, Phys. Rev., B 41, 4038 (1990)

59. S. E. Babcock, X. Y. Cai, D. L. Kaiser and D. C. Larbalestier, Nature, 347, 167 (1990)

60. S. E. Babcock and D. C. Larbalestier, J. Mat. Res., 5, 919 (1990)

61. D. M. Kroeger, J. Brynestad and R. A. Padgett, Appl. Phys., 64, 1266 (1988)

62. D. M. Kroeger, A. Choudhury, J. Brynestad and R. K. Williams, R. A. Padgett and W. A. Coghlam, J. Appl. Phys., 64, 331 (1988)

63. S. Jin, T. H. Tiefel, R. C. Sherwood, M. E. Davis, R. B. van Dover, G. W. Kammmlott, R. A. Fastnacht and H. D. Keith, Appl. Phys. Lett., 52, 2074 (1988)

64. M. Murasaki, M. Morita and N. Koyoma, Jpn. J. Appl. Phys., 28, L1125 (1989)

65. K. Salama, V. Selvamanickam, L. Gao and K. Sun, Appl. Phys. Lett., 54 2352 (1989)

66. J. Heinrich, N. Henn and M. Bohmer, Mat. Sci. and Eng., 71, 131 (1985)

67. W. A. Kaysser, M. Aslan, E. Arzt, M. Mitkov and G. Petzow, Powder Met., 1, 63 (1988)

68. D. W. Richerson and I. M. Wimmer, J. Am. Ceram. Soc., 66 [9], C-173 (1983)

69. M. Bohmer, Sci. Ceram., II, 439 (1981)

70. J. K. Tien, J. C. Borofka, B. C. Hendrix, T. Caulfield and S. H. Reichman, Met. Trans., 19A, 1841 (1988)

71. K. Sadananda, A. K. Singh, M. A. Iman, M. Osofsky, V. LeTourneau and L. E. Richards, Adv. Ceram. Mat., 3, 524 (1988)

72. J. Niska, B. Loberg and K. Easterling, J. Am. Ceram. Soc., 72, 1508 (1989)

73. B. C. Hendrix, T. Abe, J. C. Borofka, J. K. Tien and T. Caufield, Appl. Phys. Lett., 55, 313 (1989)

74. H. Okada and K. Homma, Proc. 6th, CIMTEC, 1023 (1986)

75. H. F. Fischmeister and E. Arzt, Powder Met., 26, 82 (1983)

76. B. Harris, Composites, 3 & 4, 152 (1972)

77. J. A. Aveston, Conference Proceedings NPL, 63 (1971)

78. A. P. Cottrell, Proc. R. Soc., A, 282 (1974)

79. I. M. Donald and P. W. McMillan, J. Mat. Sci., 11, 949 (1976)

80. J. Aveston, G. A. Cooper and A. Kelly, "The Properties of Fibre Composite". IPS Sci. Tech., 15 (1971)

81. D. B. Marshall and A. G. Evans, J. Am. Ceram. Soc., 68, 225 (1985)

82. D. B. Marshall, B. N.Cox and A. G. Evans, Acta. metall., 33, 2013 (1985)

83. S. G. Sashedri and Kai-Yin Chia, J. Am. Ceram. Soc., 70 [10], C242 (1987)

84. J. V. Mullin and A. C. Knoell, Mat. Res. and St., Dec., 16 (1970)

85. C. Zweben, Eng. Sci. Cerm. Prc., (7-8), 499 (1985)

86. J. J. Mecholsky, Ceram. Bulletin, 65, 315 (1986)

87. D. B. Marshall and A. G. Evans, J. Am. Ceram. Soc., 68 [5], 225 (1985)

88. D. Lewis, C. Bulik and D. Shadwell, Ceram. Eng. Sci. Proc., 6, 507 (1985)

89. G. C. Sih, P. C. Paris and G. R. Irwin, Int. J. Fract. Mech.,1, 189 (1965)

90. R. M. Anderson, Adv. Mat. Proc., March, 31 (1989)

91. Quantum Design. Co., "Operation Manual"

92. Y. Syono, M. Kikuchi, K. Ohishi, K. Hiraga, H. Arai, Y. Matsui, N. Kobayashi, T. Sasaoka and Y. Muto, Jpn. J. Appl. Phys., 26, L498 (1987)

93. L. H. Van Vlack, "Materials Science for Engineers" Addison-Wesley Pub. Co., 509 (1971)

94. W. F. Brown, and J. E. Srawley, ASTM, STP 410, 12 (1966)

95. E. S. H. Burshop, "The Auger Effect and Other Radiationless Transitions", Cambridge University Press, Cambridge, (1952).

96. L. A. Harris, J. Appl. Phys., 39, 1419 (1967)

97. Handbook of Auger Electron Spectroscopy, JEOL Ltd., Tokyo, 1982

98. B. D. Cullity, "Elements of X-ray Diffraction", 2nd ed., Addison Wesley Pub. Co., 140 (1978)

99. W. Wong-Ng, H. McMurdie, B. Paretzkin, C. Hubbard and A. Dragoo, Powder Diffraction J 2, 192 (1987)

100. R. W. McCallum, J. D. Verhoeven, M. A. Noack, E. D. Gibson, F. C. Laabs, D. K. Finnemore and A. R. Moodenbaugh, Adv. Ceram. Mat., 2, 388 (1987)

101. Y. Yamada, M. Yata, Y. Kaieda, H. Irie and T. Matumoto, Jap. J. Appl. Phys., 28, L797 (1989)

102. D. K. Dijken and J. Th. M. DeHosson, Appl. Phys. Lett., 58, 1911 (1991)

103. D. Murphy, S. Sunshine, R. B. Van Dover, R. J. Cava, B. Batlogg, S. M. Zahurak and L. F. Schneemeyer, Phys. Rev. Lett., 58, 1888 (1987)

104. Metal Handbook, Vol. 2 10th edition, ASM International Handbook Committee, 102, 1990

105. R. L. Carriere, O. M. Fuller and M. Ternan, J. Mat. Sci., 6, 265 (1971)

106. I. W. Donald and P. W. McMillan, J. Mat. Sci., II, 949 (1976)

107. W. D. Kingery, H. K. Bowen and D. R. Uhlmann, "Introduction to Ceramics", 2nd., edition, John Wiley & Sons, Inc., 794, 1976

108. T. Hashimoto, K. Fueki, A. Kishi, T. Azumi and H. Koinuma, Jap. J. App. Phys., 27, L214 (1988)

109. W. D. Callister, Jr.,"Material Science and Engineering", 2nd., edition, John Wiley & Sons, Inc., 207, 1991

110. S. E. Babcock, T. F. Kelly, P. J. Lee, J. M. Seuntjens, L. A. Lavanier, and D. C. Larbalestier, Physica C, 152, 55 (1988)

111. D. M. Kroeger, J. Brynestard and R. A. Padgett, Appl. Phys. Lett., 52, 1419 (1988)

112. T. L. Rama Char and R. Sadagopachari, Current Science (India) 19, 284 (1950)

113. P. Hansen, "Constitution of binary alloys", 2nd ed., McGraw-Hill book Co. Inc., 1958